

© 2007

TAO HAN

ALL RIGHTS RESERVED

ELECTROSPINNING AND NANOFIBERS

A Dissertation

Presented to

The Graduate Faculty of the University of Akron

In Partial Fulfillment

of the Requirements for the Degree

Doctor of Philosophy

Tao Han

December, 2007

ELECTROSPINNING AND NANOFIBERS

Tao Han

Dissertation

Approved:

Accepted:

---

Advisor  
Darrell H. Reneker

---

Department Chair  
Mark D. Foster

---

Committee Member  
Gary R. Hamed

---

Dean of the College  
Stephen Z. D. Cheng

---

Committee Member  
Alexei P. Sokolov

---

Dean of the Graduate School  
George R. Newkome

---

Committee Member  
Ali Dhinojwala

---

Date

---

Committee Member  
George G. Chase

## ABSTRACT

Electrospinning offers a unique way to produce submicron and nanofibers. It utilizes an electrical force to generate a fine, charged jet from the surface of a viscous liquid. This jet moves straight towards a grounded collector for a certain distance, then bends into spiral coils; finally, the jet solidifies and collects as nonwoven cloth. Determination of the jet path near the onset of the electrical bending instability is important for the orderly collection of the electrospun fibers. The onset and development of the electrical bending instability were investigated. Under certain conditions, high applied voltage prohibited the onset of bending instability and a straight jet reached the collector. Micron and submicron fibers were produced by collecting a straight jet on a moving collector. The diameter, velocity and the longitudinal stress along the jet axis of an electrospinning jet were measured using custom-built equipment. A new apparatus was designed to measure the longitudinal stress along the electrospinning jet. The relaxation of longitudinal stress along the electrospinning jet was experimentally verified. The elongational relaxation time and elongational viscosity of the polymer solution were characterized. Buckling instabilities of electrospinning jets were observed and compared with the behavior of uncharged jets. Various two-dimensional and three-dimensional micron size patterns were produced by the buckled electrospun fibers. A novel pendulum-like motion of a straight

electrified jet was observed and the resulting hierarchical structures made from buckled fibers were presented. A theoretical model was proposed and simulated results showed reasonable agreement with the experimental observations. This work extends the understanding of the complicated electrospinning process.

## DEDICATION

This dissertation is dedicated to my family.

## ACKNOWLEDGEMENTS

I would like to sincerely express my gratitude to my research advisor, Dr. Darrell H. Reneker who gave me the direction and freedom to approach the problems. His guidance, encouragement and support are greatly appreciated.

I am deeply indebted to Dr. Alexander L. Yarin for his great contribution to this work. It is wonderful experience to work with him through all the projects.

Special thanks to the committee members, Dr. Gary R. Hamed, Dr. Ali Dhinojwala, Dr. Alexei Sokolov and Dr, George G. Chase, who took the time to read my dissertation and helped me to improve it with thoughtful comments and suggestions.

I want to acknowledge the group members in Dr. Reneker's lab for their great discussions and technical supports.

Finally, I would like to express my love and appreciation to my wife, my parents and my brother. Without the family, I cannot go anywhere.

## TABLE OF CONTENTS

	Page
LIST OF TABLES .....	x
LIST OF FIGURES .....	xi
CHAPTER	
I. INTRODUCTION .....	1
II. BACKGROUND OF ELECTROSPINNING .....	4
III. ELECTRICAL BENDING INSTABILITY IN ELECTROSPINNING JET .....	27
3.1 Introduction .....	27
3.2 Experimental .....	31
3.3 Results and discussion .....	32
3.3.1 Electrical bending instability as a function of distance .....	32
3.3.2 Electrical bending instability as a function of applied voltage .....	37
3.3.3 Onset of electrical bending instability in the straight segment.....	39
3.3.4 Electrospun fibers produced by a straight electrified jet. ....	39
3.4 Summary .....	44
IV. INVESTIGATION OF THE DIAMETER, VELOCITY AND LONGITUDINAL STRESS PROFILE OF ELECTROSPINNING JET.....	45
4.1 Introduction .....	45

4.2 Theoretical background.....	46
4.2.1 Measurement of jet diameter .....	47
4.2.2 Measurement of jet velocity.....	53
4.2.3 Measurement of longitudinal stress along jet .....	56
4.3 Experimental.....	63
4.4 Results and discussion .....	66
4.5 Summary .....	77
V. BUCKLING INSTABILITY OF ELECTROSPINNING JETS.....	79
5.1 Introduction .....	79
5.2 Experimental .....	80
5.3 Results and discussion .....	82
5.3.1 Buckling of straight electrified jets: PEO solution collected on a horizontal moving grounded plate .....	84
5.3.2 Buckling of bending electrospinning jets: PEO solution collected on a horizontal moving grounded plate .....	85
5.3.3 Buckling of bending electrospinning jets: PEO jets onto an inclined moving collector.....	87
5.3.4 Buckling of straight electrified jets: PLLA jets collected on a horizontal moving grounded plate .....	89
5.3.5 Buckling of straight electrified jets: Polystyrene jets onto a horizontal moving grounded plate .....	92
5.3.6 Buckling of bending electrospun jets: nylon-6 onto an inclined moving collector .....	95
5.3.7 Comparisons between the buckling instabilities of uncharged fluid jets and electrified fluid jets .....	98

5.4 Summary .....	106
VI. PENDULUM-LIKE MOTION OF STRAIGHT ELECTRIFIED JETS.....	108
6.1 Introduction .....	108
6.2 Experimental .....	109
6.3 Results and discussion .....	111
6.3.1 Experimental results .....	111
6.3.2 Theoretical model .....	123
6.4 Summary .....	135
VII. SUMMARY AND CONCLUSIONS .....	136
REFERENCES .....	139

## LIST OF TABLES

Table	Page
4.1 Characteristics of the polyethylene oxide solution calculated from Eq. (4.19) and Eq. (4.20).....	77
5.1 Comparison of the measured and calculated buckling frequencies of electrospinning jets. ....	105

## LIST OF FIGURES

Figure	Page
1.1 (Number of molecules on surface) divided by (total number of molecules) and surface area per unit mass plotted functions of diameter of the fiber.....	2
1.2 The annual number of publications on the research topic of “electrospinning”, obtained by SciFinder Scholar 2006 on 11/1/2007. For 2007, the number provided is the number of publications before 11/1/2007.....	3
3.1 Electrospinning jet with electrical bending instability.....	29
3.2 Straight electrified jet .....	30
3.3 Schematic drawing of electrospinning setup with movable inclined collector....	33
3.4 Camera set up for the observation of electrospinning jet. ....	33
3.5 a, b, c are from video camera (60 frames/second) images of an electrospinning jet at different collector parameters; e, f, g are high speed camera images (2000 frames/second; shutter speed 1/10,000) of the electrospinning jet. The distances from the orifice to the grounded collector (H) increased from left to right. For a and e, H=25 mm; for b and f, H=53 mm; for c and g, H=75 mm. The edge of the collector, seen as a broad white line showed the inclination. ....	34
3.6 Optical microscopy images ( $a_1, b_1, c_1$ ) and scanning electron microscopy images ( $a_2, b_2, c_2; a_3, b_3, c_3$ ) of electrospun fibers. The length of the horizontal edges of the optical microscopy images ( $a_1, b_1, c_1$ ) are 450 $\mu\text{m}$ ; The length of the horizontal edges of the SEM images are 65 $\mu\text{m}$ ( $a_2, b_2, c_2$ ) and 13 $\mu\text{m}$ ( $a_3, b_3, c_3$ ) . The distance from the orifice to the collector was about 25 mm in $a_1, a_2, a_3$ ; 53 mm in $b_1, b_2, b_3$ and 75 mm in $c_1, c_2, c_3$ . ....	36
3.7 High frame rate camera images of the onset and development of the electrical bending instability along an electrically driven jet. The time at which the voltage was lowered is shown in the upper left corner. ....	38

3.8 Electrospun fibers produced by a straight electrified jet	
a. Electrospun fibers collected by a static collector. ....	40
b. Electrospun fibers collected by collector moving at 0.785 m/s. ....	41
c. Electrospun fibers collected by collector moving at 1.57 m/s. ....	42
3.9 Two-dimensional patterns made from electrospun fibers	
a. Two-dimensional patterns made from electrospun fibers.....	43
b. Two-dimensional patterns made from electrospun fibers.....	43
4.1 Young’s double slits interference. ....	48
4.2 Single slit interference .....	50
4.3 The observation of the interference colors along the jet axis.....	52
4.4 Optical image of the straight segment of an electrospinning jet.....	53
4.5 A typical frequency spectrum from the Laser Doppler Velocimeter.....	54
4.6 Jet speed measurement by particle tracing. ....	55
4.7 Diagram of apparatus used by Zeleny .....	57
4.8 Taylor cone with the transition zone in an electrically-driven jet. ....	59
4.9 Sketch of a tapered straight jet, and lateral (bending) perturbation of its axis. .	60
4.10 Drawing of the experimental setup for measuring radius and velocity distributions and evaluating the stretching rate. (1) Pipette; (2) high voltage DC power supply; (3) ammeter; (4) grounded collector; (5) digital video camera ; (6) optical microscopy; (7) illumination light. ....	64
4.11 Profile of the transitional zone following the Taylor cone and the beginning of the jet. The cross-sectional radius is shown as $a = a(x)$ (the symmetric profile in the middle-left), where the axial coordinate $x$ is rendered from the first observable cross-section of the drop. At the end of the transition zone and the beginning of the jet, $x = x_e$ . The velocity distribution measured is shown by the solid curve below the profile $a = a(x)$ . The change in the jet diameter after the transition zone is practically unseen in this scale which is the reason that the velocity distribution in the figure in two cases extends beyond the profile of the transition zone. (a) Measured for the applied voltage of 3 kV, (b) 4 kV, (c) 5 kV.	65

4.12 Schematic drawing of the experimental setup for measuring longitudinal stresses in jets. (1) Pipette; (2) high voltage DC power supply; (3) ammeter; (4) grounded collector; (5) loudspeaker; (6) polystyrene bar; (7) high speed camera; (8) illumination light.....	67
4.13 Propagation and widening of a single lateral displacement pulse. (a) The inter-electrode distance $L=5.5$ cm, potential difference of $U= 3$ kV, and the electric current $I= 100$ nA. (b) The inter-electrode distance $L= 5.5$ cm, potential difference of $U= 4$ kV, and the electric current $I= 390$ nA. (c) The inter-electrode distance $L= 5.5$ cm, potential difference of $U= 5$ kV, and the electric current $I= 880$ nA. In all the cases the jet was straight before the lateral displacement pulse was applied. ....	68
4.14 Pulse peak location $P$ and width $w$ versus time. The broken lines connect the data points shown by symbols, the smoothed lines show the best fit of the data. The width-time curve is used to evaluate $\frac{\partial w}{\partial t} = W/\Delta t$ needed to calculate the longitudinal stress $\sigma_{xx}$ in the unperturbed jet using Eq. (4.17). The voltage applied to issue the jet was 3 kV in this case.....	70
4.15 Longitudinal stress distribution over the straight unperturbed electrified jet for different applied voltages. The inter-electrode distance was held at 5.5 cm. (a) Stress versus pulse-related time $t$ , $\sigma_{xx} = \sigma_{xx}(t)$ . (b) The Eulerian presentation as $\sigma_{xx} = \sigma_{xx}(x)$ . ....	71
4.16 The Lagrangian presentation $\sigma_{xx} = \sigma_{xx}(t_m - t_{me})$ . The time moments when the material element exits the transition zone and reaches the beginning of the jet is denoted by $t_{me}$ . The values of $t_{me}$ were 15145 ms, 1880 ms and 1183 ms for the voltages of 3 kV, 4 kV and 5 kV, respectively. The distributions of stress $\sigma_{xx}$ versus $t_m - t_{me}$ are plotted in semi-logarithmic scale. Symbols show the experimental data for different applied voltages; lines are plotted using Eq.(4.19) and Eq.(4.20).....	72
5.1 Sketch of the experimental setup.....	81
5.2 Straight electrified jet .....	83
5.3 Electrospinning jet with electrical bending instability.....	83
5.4 SEM image of some of the buckled PEO patterns collected on the horizontal collector which was moving at 0.785 m/s along the direction showed by the white arrow. ....	85

5.5 Optical micrographs of buckled bending electrospun PEO jets. ....	86
5.6 Optical images of bent and buckled PEO loops and patterns collected at different inter-electrode distances on the surface of a inclined collector which moved at 0.01m/s along the direction shown by the white wide arrow in Figure 5.6-a. ....	88
5.7 Optical images of buckled solidified PLLA patterns. The horizontal collector was moved in direction shown by the black arrow in Figure 5.7-a .The distance $\lambda$ (the wave length) corresponds to the lateral motion during one period of the formation of the buckling pattern .....	91
5.8 Optical micrographs of buckled polystyrene patterns. The horizontal collector was moved in the direction shown by the black arrow in Figure 5.8-a.....	93
5.9 Optical micrographs of buckled polystyrene patterns collected on a static water surface.....	94
5.10 Three-dimensional buckled patterns formed after the impingement of a polystyrene jet onto a water surface. The samples were dipped from the water with a glass microscopic slide and observed with the optical microscopy. ....	95
5.11 Buckled and bent electrospun nylon-6 deposits. The lengths of the horizontal edges of the images a, b, d, e are 0.18 mm; the length of the horizontal edge of the image c is 9.0 mm. The total change in the inter-electrode distance was about 0.3 cm from the left edge to the right edge in Figure 5.11-c. ....	97
5.12 Comparison of the buckled patterns created by electrified jets of polyethylene oxide in water, collected on glass slides, to patterns <sup>146</sup> produced by the buckling of uncharged gravity-driven syrup jets. ....	101
5.13 Comparison of the buckled patterns created by electrified nylon-6 jets collected on water to the buckling patterns <sup>146</sup> resulting from uncharged gravity-driven syrup jets. ....	102
5.14 Buckled patterns created by electrified nylon-6 jets collected on a water surface. These do not have analogies among those reported by Chiu-Webster et al. <sup>146,147</sup> .104	
6.1 Schematic drawing of the experimental setup.....	109
6.2 Figure 6.2 Setup for the observation of the jet. ....	110
6.3 High frame rate video image of an electrified pendulum-like jet above the collecting surface. ....	112

6.4 Optical microscopic images of patterns deposited by electrified jet moving as a pendulum. The voltage was 3 kV, the inter-electrode distance was 0.5 cm; the grounded electrode was moved horizontally at 0.001 m/s. ....	113
6.5 Optical microscopic images of patterns produced from electrified jet moving as a pendulum. The voltage was 4 kV, the inter-electrode distance was 0.8 cm; the grounded electrode was moved horizontally at 0.01 m/s. ....	114
6.6 Optical microscopic images of patterns produced from electrified jet moving as a pendulum. The voltage was 4 kV, the inter-electrode distance was 1.8 cm; the grounded electrode was moved horizontally at 0.01 m/s. ....	115
6.7 Optical microscopic images of patterns produced from electrified jet moving as a pendulum. The voltage was 4 kV, the inter-electrode distance was 2.0 cm; the grounded electrode was moved horizontally at 0.01 m/s. ....	116
6.8 Optical microscopic images of patterns produced from electrified jet moving as a pendulum. The Nylon-6 fibers were collected on the static water surface which served as a grounded electrode. The voltage was 4 kV; the inter-electrode distance was 3.0 cm. ....	117
6.9 The electrical current carried by the electrified straight jets as a function of the inter-electrode distance for different applied electrical voltages. A horizontal motionless aluminum sheet was used as a grounded collector (electrode). ....	118
6.10 The whole envelop angle about the electrified pendulum jet configurations as a function of the inter-electrode distance for different applied electrical voltages. A horizontal motionless aluminum sheet was used as a grounded collector (electrode). ....	119
6.11 Rotation frequency $f$ of the pendulum-like motion of the electrified jets as a function of the inter-electrode distance for different applied electrical voltages. A horizontal motionless aluminum sheet was used as a grounded collector (electrode). ....	120
6.12 Diameter of the collected circular deposits of the electrified jets as a function of the inter-electrode distance for different applied electrical voltages. A horizontal motionless aluminum sheet was used as a grounded collector (electrode). ....	121
6.13 The end velocity of the electrified jets as a function of the inter-electrode distance for different values of the applied electrical voltages. A horizontal static aluminum sheet was used as a grounded collector (electrode) .....	122

6.14 Schematic drawing of the pendulum-like motion of the electrified jet. .... 124

6.15 Theoretically predicted pendulum-like motion of an electrified jet for the initial conditions  $t = 0: x = 0.3, y = 0.3, V_x = -0.5, V_y = 0.5$  (a) Three-dimensional configurations of the jet at several times moments (here and hereinafter the  $xyz$  coordinates are rendered dimensionless by  $a$ ). (b) The trajectory of the jet end on the horizontal motionless grounded electrode. (c) The horizontal coordinates of the jet end on the grounded electrode as functions of time; time is rendered dimensionless by  $T$ . ..... 129

6.16 Theoretically predicted pendulum-like motion of an electrified jet for the initial conditions:  $t = 0: x = 0.3, y = 0.1, V_x = -0.5, V_y = 0.5$ . The trajectory of the landing point of the jet on the horizontal motionless grounded electrode is shown. .... 132

6.17 Theoretically predicted pendulum-like motion of an electrified jet for the initial conditions:  $t = 0: x = 0.9, y = 0.1, V_x = -0.5, V_y = 0.5$ . .... 133

## CHAPTER I

### INTRODUCTION

Electrospinning<sup>1</sup> is a method to produce nanofibers. Unlike mechanical fiber spinning techniques, electrospinning utilizes an electrical force to elongate a jet into nanometer size fibers. A polymer solution or a polymer melt is charged in a high electric potential that produces an electrical field of about 1 kV/cm between spinneret and collector. When the electric force acting on the surface of a liquid overcomes surface tension, a charged liquid jet is pulled from the liquid surface<sup>2</sup> and moves straight towards a grounded collector. If the distance between spinneret and collector is short the jet goes straight to the collector and buckles<sup>3,4</sup>; if the distance between spinneret and collector is large, the straight jet becomes unstable and bends into spiral loops. This electrical bending instability<sup>5,6</sup> is a unique characteristic of electrospinning. Electrospun fibers are often collected as nonwoven mesh.

Electrospinning can form continuous fibers with diameters in the range of nanometers; this is one or two orders of magnitude smaller than conventional textile fibers. Electrospun fibers have a large surface area to mass ratio (Figure 1.1).

Figure 1.2 shows the rapid development of the scientific publications and patents concerning electrospinning.

Donaldson Inc.<sup>7</sup> has incorporated nanofibers into filters to increase the efficiency of filtering small particles. Electrospun nonwoven mesh incorporated with catalyst has been used in clothing to provide protection from chemical and biological hazards<sup>8,9,10</sup>. Electrospun fibers are also ideal materials in biomedical applications.

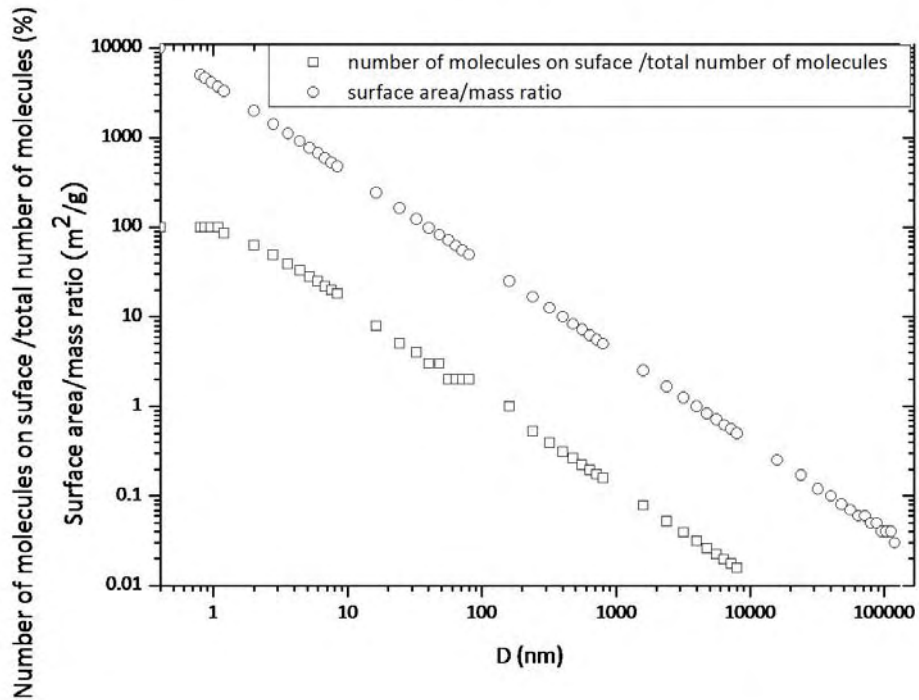


Figure 1.1 (Number of molecules on surface) divided by (total number of molecules) and surface area per unit mass plotted as functions of fiber diameter.

Electrospun fibers have been used as cell growth scaffolds for tissue engineering, drug delivery system, wound dressing and operation separation films<sup>11,12</sup>. Craighead et al.<sup>13,14,15,16,17</sup> and Greine et al.<sup>18,19,20,21,22</sup> utilized electrospun fibers as templates to produce micro channels and hollow fibers for various applications. Coaxial

electrospinning techniques recently developed by Sun et al.<sup>23</sup>, Larsen et al.<sup>24,25</sup>, Li and Xia<sup>26</sup> enable electrospinning of continuous hollow tubes and coaxial composite fibers<sup>27,28,29,30,31,32,33,34,35</sup>.

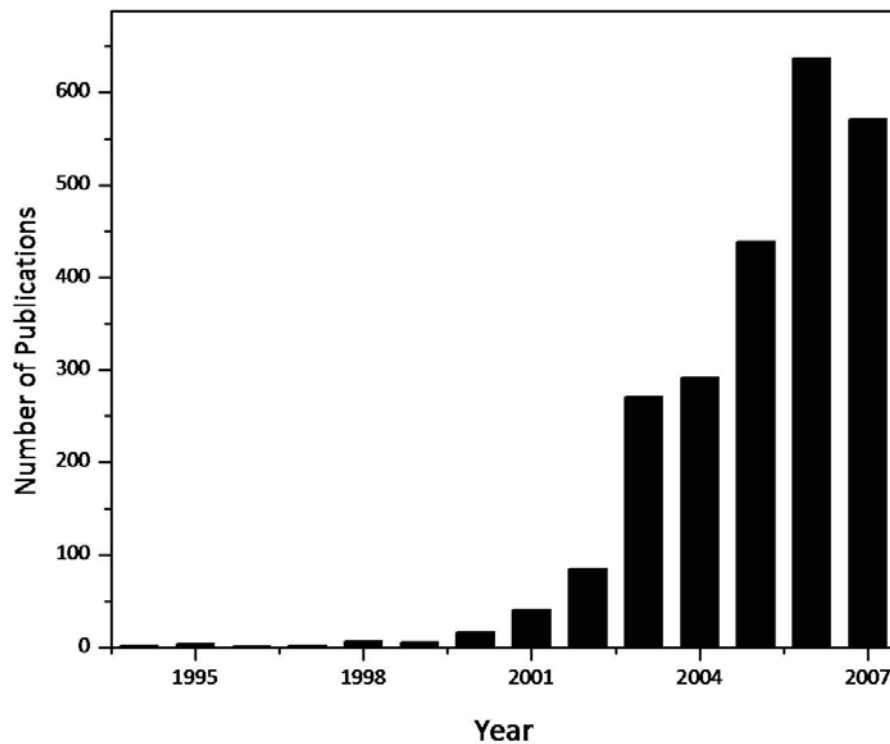


Figure 1.2 The annual number of publications on the research topic of “electrospinning”, obtained by SciFinder Scholar 2006 on 11/1/2007. For 2007, the number provided is the number of publications before 11/1/2007.

## CHAPTER II

### BACKGROUND OF ELECTROSPINNING

The stability of electrically charged liquid droplets and electrified liquid jets has been investigated for hundreds of years. These works provide the fundamental basis for electro spraying and electro spinning. The distinction between electro spraying and electro spinning is the stability of the electrified jets. Capillary instability of an electrified jet tends to break it into droplets. If the fluid lacks enough entanglements an electrified jet will undergo capillary instability and break into droplets (electro spraying). If the fluid is sufficiently entangled, this stabilizes the jet and prevents its breakdown. Thin filaments with or without beads are formed (electro spinning).

William Gilbert<sup>36</sup> found that a spherical drop of water on a dry surface is drawn up into a cone when a piece of rubbed amber is held at a suitable distance above it. This was the first experiment that described how a droplet is deformed in a uniform electric field. The reason is that the charges on the drop surface induced by the electric field set up “outward” electrostatic forces which oppose the surface tension forces of the liquid. A sufficiently high field can disrupt the liquid surface so that an aerosol spray of charged droplets is produced. The first electro spraying experiment was done by Bose<sup>37</sup> at 1745. Bose produced aerosols by applying high electric potentials to liquid droplets at the end of a glass capillary tube.

Lord Rayleigh<sup>38, 39, 40</sup> investigated the number of charges that are needed to overcome the surface tension of a liquid drop. He showed that an isolated, charged liquid sphere becomes unstable when the charge exceeds a critical value. He calculated the maximum charge that a drop of liquid can maintain before electrical forces overcame surface tension and created a jet.

In 1902, 1903 the first electrospray devices were patented by Cooley and Morton<sup>41, 42, 43</sup>. Zeleny<sup>44, 45, 46, 47</sup> published work about the instability of electrified liquid surfaces; this is the foundation of the modern electrospraying field. Zeleny showed that the theoretical relations for instability were satisfied when discharge of a jet began. Zeleny produced some threads that were about 4  $\mu\text{m}$  in diameter. These were “pulled-out” from the liquid surface at speed of 8 m/s. Zeleny reported different stages of discharge from a liquid surface, depending on the applied voltage. From low to high voltage, discharge took place in repeated pulses to steady discharge. He observed oscillation of discharge in some experiments. He also demonstrated a method to evaluate surface charge intensity by reading pressure change in a liquid reservoir. Zeleny recorded the motion of electrified jets and their breakup. He observed that fine threads of liquid often underwent very rapid changes in direction. This is similar to electrical bending instability proposed by Yarin and Reneker<sup>5, 6</sup>.

In 1929, Hagiwaba et al.<sup>48</sup> described fabrication of artificial silk through using electrical charge. Anton Formhals<sup>49,50</sup> filed the first patent about electrospinning of plastics. A spinning solution was discharged using a high electric field. Fine filaments were attracted towards a movable electrode that was of opposite polarity. A device

removed fibers in fibrous sliver. A major drawback was the difficulty removing fine fibers that adhered to moving parts (belts, drums, wheels). Formhals produced fibers from a solution of cellulose acetate in ethylene glycol at a potential difference of 57 kV.

Vonnegut and Neubauer<sup>51</sup> generated uniform streams of highly charged droplets with diameters around 0.1 mm. Monodisperse aerosols with a particle radius of a micron or less were produced from pendant droplets at the end of a pipette.

In the 1960s, Taylor<sup>52</sup> analyzed conditions where a droplet deformed by an electric field into a conical geometry (Taylor cone). By examining a range of low molecular weight fluids, Taylor concluded that the conical interface between air and fluid was stable at the semi-angle conical angle of  $49.3^\circ$ . Conductivity and viscosity both play an important role in electrostatic atomization. These influence the equilibrium angle and other aspects of the process. Taylor cones<sup>53</sup> define the onset of extensional velocity gradients in fiber formation. Taylor<sup>52, 54</sup> published a theoretical treatment about instability of conductive liquid surfaces. For a conductive fluid, the equilibrium semi-conical angle is  $49.3^\circ$ , a universal value now well known as the Taylor cone in the fields of electrospraying and electrospinning. Taylor<sup>55</sup> claimed that in a parallel electrical field an electrically driven water jet has two critical levels one where a jet breaks into droplets and another where a jet bends into spiral coils. The former instability is the Rayleigh instability<sup>56</sup> and the second one is an electrical bending instability. The Rayleigh instability is due to the surface tension, which is always trying to minimize surface area. For an electrically driven conductive viscous fluid, the Rayleigh instability is usually suppressed by the viscous stress which balances the surface tension. The second type of

instability is an electrical bending instability<sup>5,6</sup>, which is due to the competition between the viscous stress along the jet and the electrostatic force working on the jet. At this condition, surface tension is negligible compared to the viscous and electrostatic forces. When the electrostatic force is higher, it overcomes the viscous stress and elongates the jet. When the electrostatic force is so low that it cannot support the jet against the contracting viscous stress, the jet becomes unstable, analogous to that of Euler buckling when an elastic column is axially compressed. Jet diameter stops decreasing after the bending instability takes place. Taylor also pointed out the difference between 'bending instability' and 'buckling instability'. A buckling jet is under longitudinal compression. This is limited to a short distance from the point where its velocity is reduced to zero. It was discovered later by Han and Reneker that an electrospinning jet also undergoes a buckling instability<sup>3,4</sup>, when it impinges onto the collector.

Simons<sup>57</sup> invented a process to produce a patterned non-woven fabric by collecting electrospinning jets on a segmented collector. The segmented collector had two sets of segments at different potential which caused the preferential deposition of fibers. This led to a patterned fabric that had regions of low and high fiber density.

In 1971, electrospinning was studied by Baumgarten<sup>58</sup>. Acrylic fibers with the diameter less than 1 micrometer were electrospun from dimethylformamide solution. Baumgarten investigated the relationships between fiber diameter, jet length, solution viscosity, flow rate and composition of the surrounding gas. Baumgarten utilized high speed photography to observe the electrospinning jet path. He found the fiber loops that shot out radially from the jet at the velocity of 6 to 7 m/s and then fell toward the

screen at 1.8 to 3.7 m/s. He investigated the influence of solution viscosity on jet length and fiber diameter. He also calculated jet velocity from pictures and concluded that the jet velocity perhaps exceeds the velocity of the sound in air.

Martin et al.<sup>59,60</sup> introduced electrospinning of multiple components.

They electrospun polymer blends solutions simultaneously from multiple nozzles.

Collectors were either a stationary metal screen or a movable belt. The patent claimed that the mat was composed of fibers of high molecular weight thermoplastic polymer (fluorinated hydrocarbon, silicone or urea/formaldehyde). The mats were flexible, non-absorbent, porous, and hydrophobic. These were suggested for wound dressings and as a lining for prosthetic devices.

Simm et al.<sup>61</sup> fabricated a composite filter based on electrospun fibers. They invented a process for the production of filters. A solution of polystyrene in methylene chloride was electrospun from an annular electrode onto two equidistant collector electrodes that were movable belts. The electrodes were already covered with a layer of cellulose fibers produced by conventional spinning methods. Thus, a composite filter that had electrospun polystyrene fibers on top of a layer of cellulose fleece was fabricated.

Horning and Hendricks<sup>62</sup> published a study of an electrically driven glycerol jet. They found that the linear charge density of the jet decreased with distance from the tip, and calculated various forces (electric, viscous, surface tension and momentum) acting on the jet. They concluded that surface tension forces are in the same range of as

electric forces. The longitudinal stress along the electrically driven jet was in the range of  $10^5$  to  $10^6$  Pa.

Fine et al.<sup>63</sup> electrospun a thermoplastic elastomer. A cup-like apparatus contained charged polymer solution that rotated about its vertical axis. Centrifugal forces pushed polymer solution to the edge of the cup and into ambient air. An electrical field caused the formation of a jet that was attracted to a grounded movable aluminum screen that was driven slowly around rollers. The combined action of electrostatic and centrifugal forces led to the formation of high strength, fibrous sheets.

Guignard<sup>64,65</sup> described a melt electrospinning apparatus with two moving belts. One belt carried charged molten polymer that approached the grounded collecting belt. Electrospinning jets were formed on the surface of the exposed melt.

Larrondo and Manley<sup>66,67,68</sup> conducted systematic studies of melt electrospinning. They electrospun poly (ethylene) and poly (propylene) from the melt. The electrospun fibers were characterized by X-ray diffraction and mechanical testing. Unoriented and slightly oriented polyolefin fibers were produced in ambient air. Spherulitic structures were found in the unoriented fibers. Alignment of the crystalline phase along the fiber axis increased with increasing applied voltage. Weak birefringence was observed in the center of the electrospinning jet, near the exit of the orifice. Larrondo and Manley concluded that fiber diameter is determined by the applied voltage and the viscosity of the melt. The electrospun fibers had low values of tenacity and modulus. Larrondo and Manley also investigated the flow field of electrospinning jets from polymer melt. Streamline and stream velocities were investigated using a model fluid and

“trace/particle” photography. The velocity field was not purely extensional, but contained rotational components. The rate of extension increased rapidly with the electric field intensity and reached values above  $50 \text{ sec}^{-1}$ .

Bornat<sup>69,70</sup> conducted multi-jet electrospinning by using several nozzles to form fibers. Different polymer solutions were held in different nozzles and a rotating long metallic cylinder was the collector. The nozzles were kept at ground potential, while an electrical potential of -50 kV was applied to the collector. Electrostatic forces caused the formation of jets that were attracted toward the collector, forming a tubular product that could find applications as synthetic blood vessels and urinary ducts.

Reneker<sup>1,71,72,73</sup> and coworkers reexamined the electrospinning and applied it to produce nanofibers. They studied the effect of several process parameters on fiber formation of poly (ethylene oxide) and other polymers.

Saville<sup>74</sup> reviewed the electrohydrodynamic work done after Taylor. He found a whipping instability in an electrified liquid jet. Spivak and Dzenis<sup>75</sup> published work on the asymptotic decay of the radius of a weakly conductive viscous jet in an external electric field. Their model assumed that the electric field was uniform and constant unaffected by the charge carried by the jet. Their model only deals with a straight electrically driven jet or the straight segment in an electrospinning jet.

Capillary instability of an electrospinning jet can cause a cylindrical electrospinning jet break up into droplets<sup>76</sup>. Electrical charge on the surface of a jet tends to stabilize it by supplying pressure that opposes surface tension. An electrified fluid jet of entangled polymer was sometimes affected by capillary instability. Collapse

of the jet created droplets that were held like a string of beads by a thin fiber. Bead formation is an extrusion process driven by surface tension. Fong et al.<sup>76</sup> reduced the excess electrical charge on a jet by supplying counter ions from a corona discharge in air. When the concentration of the counter ions was small, the electrospun nanofibers were smooth. As the concentration of ions increased, more of the charge on the jet was neutralized by airborne ions. As the charge density on the surface of a jet decreased, the number of beads per unit length increased, and the volume of polymer in the form of nanofibers, relative to the volume of polymer in beads, decreased. They also found that increasing the viscosity of the electrospinning solution or increasing the concentration of dissolved salt in the polyethylene oxide solution tended to stabilize the jet against the formation of beads.

Scardino et al.<sup>77</sup> patented a process to make a hybrid/composite yarn. Electrospun fibers were suctioned into an air vortex and then combined with carrier filaments to form nonwoven or linear assemblies. The yarns were later utilized for weaving, braiding or knitting fabrics. Utilizing the similar approach to make composite fibrous mats, Zarkoob<sup>78</sup> et al. patented a process to produce silk nanofibers and silk nanofiber composites.

Spivak, Dzenis and Reneker<sup>79</sup> proposed a model of steady state jet in the electrospinning process. This work initiated the rebirth of the theoretical investigation of electrospinning process. It considered a straight electrified jet and did not deal with the sophisticated instability of an electrospinning.

Reneker, Yarin and coworkers<sup>2,5,6</sup> published series papers about the theoretical

modeling of the development of Taylor Cone and electrospinning jet. Their model successfully explained the onset and development of the electrical bending instability of an electrospinning jet. They modeled a polymer jet by a linear Maxwell equation. Columbic repulsions between charges on the jet surface generate bending forces that destabilize the jet and introduces the electrical bending instability. Jet paths simulated from the model agreed well with experimental observations. Draw ratio, jet velocity, longitudinal stress along the jet were calculated and compared with the experimental data. From their calculation, strain rate in the straight segment of the electrospinning jet is in the  $20 \text{ sec}^{-1}$  range and up to  $100000 \text{ sec}^{-1}$  in the bending loops which suggest strong orientation and stretching of the molecular chains. Yarin, Koombhongse and Reneker<sup>2</sup> reported the value of Taylor cone is  $33.5^\circ$  based on a non-self similar assumption.

Electrospun fibers in the form of ribbons with various cross sections were observed by Koombhongse et al.<sup>80</sup>. These ribbons were resulted from a thin skin formed by the rapid evaporation of the solvent. The skin had little influence during the early part of the jet path, where jet diameter was much larger than the thickness of the skin.

Branched fibers<sup>80, 81</sup> were formed in the electrospinning process by the ejection of smaller jets from the surface of the primary jets. This was similar to the ejection of a jet from the surface of a charged droplet. Split fibers were formed by the separation of a primary jet into two smaller jets.

Hohman, Shin, Rutledge and Brenner<sup>82, 83, 84, 85</sup> published a whipping model of an electrospinning jet. They developed a slender-body theory for electrospinning that couples jet stretching, charge transport, and the electric field. They defined three

different instabilities of an electrospinning jet: the Rayleigh instability, an electric field induced axisymmetric instability, and a whipping instability. At increasing field strength, the electrical instabilities are enhanced whereas the Rayleigh instability is suppressed. Which instability wins depends strongly on the surface charge density and the radius of the jet. They reported that the mechanics of electrospinning is best described as a disintegrating whipping jet. Surface charge density is the most important parameter dictating the stability of the jet. The detailed shape and material properties of the nozzle affect the stability of the jet, even when the jet is far from the nozzle.

Reneker et al.<sup>86</sup> reported a new phenomenon: nanofiber garland in electrospinning. Electrospinning of a polycaprolactone in acetone solution caused a dramatic appearance of a fluffy, columnar network of fibers that moved slowly in large loops. Reneker et al.<sup>86</sup> named this columnar network 'garland'. Open loops of the single jet came into contact just after the onset of the electrical bending instability and then merged into a cross-linked network which created and maintained the garland. Contacts between loops occurred when the plane of some of the leading loops of the jet rotated around a radius of the loop. A small following loop, expanding in a different plane, intersected a leading loop that was as many as several turns ahead. Mechanical forces overcame the repulsive forces from the charge carried by the jet, the open loops in flight made contact and merged at the contact point, to form closed loops. The closed loops constrained the motion to form a fluffy network that stretched and became a long roughly cylindrical column a few millimeters in diameter. This garland, which was electrically charged, developed a path of large open loops that are characteristic of a

large scale electrical bending instability. Over a long period of time, the fluffy garland never traveled outside a conical envelope similar to, but larger than the conical envelope associated with the electrical bending instability of a single jet. The curly path of the garland appears to be the result of an electrical bending instability that is similar to what occurs in a single electrospinning jet.

Feng<sup>87, 88</sup> published studies about the stretching of a straight electrically charged viscoelastic jet. He pointed out that the whipping model for electrospinning proposed by Hohman et al.<sup>82, 83, 84, 85</sup> has a problem with the boundary condition at the nozzle. In the whipping model, unless the initial surface charge density is zero or very small, the jet bulges out upon exiting the nozzle in a “ballooning instability,” which never occurs in reality. No steady solution was possible for fluids with higher conductivities from the whipping model. Feng described a slightly different Newtonian model that avoids this kind of instability. Well-behaved solutions were produced that are insensitive to the initial charge density, except inside a tiny “boundary layer” at the nozzle. A non-Newtonian viscosity function was introduced into the model and the effects of extension thinning and thickening were explored. His result showed two distinct regimes of stretching. For a “mildly stretched” jet, the axial tensile force in the fiber resists stretching, so that extension thinning promotes stretching and thickening hinders stretching. For a “severely stretched” jet, on the other hand, the tensile force enhances stretching at the beginning of the jet and suppresses it farther downstream. The effects of extensional viscosity then depend on the competition between the upstream and downstream dynamics. He concluded that the stretching is more pronounced at the

beginning but weakens later, and ultimately thicker fibers are produced because of strain hardening.

The influence of solution concentration, molecular weight, amount of entanglements, and intermolecular interactions on the stability of the electrospinning jets and the morphologies of electrospun fibers have been investigated by several research groups. Lee et al.<sup>89</sup> reported the controllability of bead morphology formed on electrospun polystyrene fibers by adjusting the combination of different solvents. In their experiment, Polystyrene (PS) dissolved in the mixture of tetrahydrofuran (THF) and N, N-dimethyl formamide (DMF) was electrospun into submicron fibers. The electrospun fibers contained irregular beads and the bead concentration was controlled by the DMF content. The aspect ratio of the formed beads and the diameter of fibers were increased with increasing solution concentration. When PS was dissolved in only THF, an unexpected half hollow spheres structure appeared.

Mckee et al.<sup>90</sup> determined the effects of concentration regime and molecular topology on electrospun fiber morphology. Fiber morphology was dependent on the zero shear rate viscosity ( $\eta_0$ ), with the presence of three distinct morphology regimes: polymer droplets, beaded nanofibers, and uniform, defect-free fibers. Moreover, the fiber diameter scaled with the  $\eta_0$  to the 0.8 power. For most of the copolymers studied, entanglement concentration ( $C_e$ ) was the minimum concentration required for electrospinning of beaded nanofibers, while 2 to 2.5 times  $C_e$  was the minimum concentration required for electrospinning uniform, defect-free fibers. Low molecular weight ( $M_w$ ) linear PET-co-PEI required  $C > C_e$  to form beaded fibers since this is not far

above the critical molecular weight for entanglements of PET-co-PEI in the melt. When the concentration was normalized using  $C_e$ , the influence of chain length and branching architecture on the electrospinning process was removed, and the fiber diameter universally scaled with the normalized concentration to the 2.6 power.

Shenoy et al.<sup>91</sup> reported how many entanglements are required to affect fiber formation in electrospinning. Polymer solution rheology arguments were extrapolated to formulate a semi-empirical analysis to explain the transition from electro spraying to electrospinning in the good solvent. Utilizing entanglements and weight average molecular weights ( $M_e, M_w$ ), the requisite polymer concentration for fiber formation can be determined. Incipient, incomplete fiber formation is correctly predicted for a variety of polymer/solvent systems at one entanglement per chain. Complete, stable fiber formation occurs at  $\geq 2.5$  entanglements per chain.

Gupta et al.<sup>92</sup> explored the scaling relationship between viscosity and concentration in a good solvent and investigated their impacts on fiber formation. Only polymer droplets were observed from electrospinning of dilute solutions due to insufficient chain overlap. As the concentration was increased, droplets and beaded fibers were observed in the semidilute unentangled regime; and beaded as well as uniform fibers were observed in the semidilute entangled regime. Uniform fiber formation was observed at  $C/C^* \sim 6$  for all the narrow molecular weight distribution (MWD) polymers where  $C$  is the solution concentration and  $C^*$  is the critical chain overlap concentration. For the relatively broad MWD polymers, uniform fibers were not formed until higher concentrations,  $C/C^* \sim 10$ , were utilized. Dependence of fiber

diameter on concentration and viscosity was also determined, viz. fiber diameter  $\sim (C/C^*)^{3.1}$  and fiber diameter  $\sim \eta_0^{0.71}$  respectively.

Shenoy et al.<sup>93</sup> investigated the influence of the physical gelation on the fiber formation in electrospinning. Close to the gelation threshold, the combination of thermo-reversible junctions and chain entanglements stabilize the liquid jet and overcome capillary forces giving nanofibers. Cooling time and dissolution temperature besides polymer concentration and molecular weight determine the physical gelation in the polymer solution thus the fiber formation.

Yu et al.<sup>94</sup> investigated the role of fluid elasticity in the formation of fibers from polymer solution by electrospinning. The model solutions with different degrees of elasticity was prepared by blending small amounts of high molecular weight polyethylene oxide (PEO) with concentrated aqueous solutions of low molecular weight polyethylene glycol (PEG). The formation of beads-on-string and uniform fiber morphologies was observed for a series of solutions having the same polymer concentration, surface tension, zero shear viscosity, and conductivity but different degrees of elasticity. A high degree of elasticity was observed to arrest the breakup of the jet into droplets by the Rayleigh instability and in some cases to suppress the instability altogether. The susceptibility of the jet to the Rayleigh instability was examined in two ways. First, a Deborah number, defined as the ratio of the fluid relaxation time to the instability growth time, was shown to correlate with the arrest of droplet breakup, giving rise to electrospinning rather than electro spraying. Second, a critical value of elastic stress in the jet, expressed as a function of jet radius and capillary

number, was shown to indicate complete suppression of the Rayleigh instability and the transition from 'beads-on-string' to uniform fiber morphology.

Carroll and Yoo<sup>95</sup> reported experimental and theoretical investigation of electrospinning Newtonian and viscoelastic jets. The effects of electrical conductivity and viscoelasticity on the jet profile during the initial stage of electrospinning were examined. The fluid was described as a leaky dielectric with charges only on the jet surface and viscoelastic models for polymer solutions fully coupled with the fluid momentum equations and Gauss' law. The model was derived using a thin filament approximation, and the resulting differential equations governing electrically charged, stable polymeric jets were solved numerically. They investigated two different solutions: Newtonian solutions of glycerol containing trace amounts of lithium chloride salt, and viscoelastic PIB/PB Boger fluid solutions. The experimental jet profiles from electrospinning experiments were compared with the model predictions. The experimental results revealed that increasing the electrical conductivity of the fluid by adding salt tends to delay the jet thinning. Increasing the fluid viscoelasticity caused a more rapid initial jet thinning, however further away from the spinneret viscoelastic jets are thicker than their Newtonian counterparts due to the higher elongational viscosity.

Higuera<sup>96</sup> published work on stationary viscosity-dominated electrified capillary jets. He used numerical computations and order-of-magnitude estimates to describe the stationary creeping flow of a jet of a Newtonian liquid with finite electrical conductivity that is injected into a dielectric medium subject to a uniform electric field. Electric current carried by a jet increased with increasing conductivity, increasing flow

rate, and increasing intensity of the electric field. The current depended on the wetting conditions of the liquid at the injection orifice. He proposed scaling laws for the electric current and other properties of the solution based on the analysis of the transfer of current to the surface of the liquid and of the evolution of the jet under the electric stresses that act at its surface.

Koombhongse, Zhong and Reneker<sup>97</sup> investigated the influence of the humidity on the formation of beads along the electrospun fibers. Evaporation and solidification affected the fiber diameter and morphology. Fiber diameter became smaller when evaporation and solidification happened more slowly because of the higher vapor concentration of solvent. Linear decrease in the diameters of electrospun fibers with increasing humidity provides an effective process control parameter. Beaded fibers were formed when jet diameter was very thin and the charge per unit area was smaller. The size of the beads and the length of fibers between them changed systematically as the relative humidity increased.

Loscertales et al.<sup>24</sup> reported encapsulation via electrified co-axial liquid jets which bring the co-electrospraying technology to the electrospinning and electrospinning field. By this method they produced monodisperse capsules with diameters varying between 10 and 0.15 micrometers, depending on the running parameters. Larsen et al.<sup>25</sup> described a method for making inorganic and hybrid fibers and vesicles with diameters in the micrometer range via sol-gel chemistry and co-axial double capillary tip electrospinning. Sanders et al.<sup>98</sup> reported two phase electrospinning from single electrified jet. They produced EVA electrospun fibers containing aqueous

reservoirs by electrospinning from the suspension. Osmotic swelling of these fibers can lead to expansion and eventually the bursting of these reservoirs.

Sun et al.<sup>23</sup> introduced a modified electrospinning process, co-axial electrospinning, which can produce core-shell electrospun fibers from co-electrospinning from two materials. Two concentrically aligned nozzles were used for spinning. Same voltage was applied to both nozzles, and it deforms the compound droplet. A jet was generated on the tip of the deformed droplet, and in an ideal case, a core-shell nanofiber was created.

Co-axial electrospinning is not limited to the production of core-shell fibers with a continuous core. Systems with discontinuous drop-shaped inclusions inside a continuous shell can also be generated. This type of morphology is of interest for the inclusion of biological objects, for example, the green fluorescent protein (GFP), in an aqueous environment, or for the storage and controlled release of drugs<sup>31</sup>.

Hollow core-shell fibers/ tubes<sup>26, 27, 99</sup> were successfully manufactured through co-electrospinning process by choosing the appropriate combination of core/shell materials. To produce ceramic hollow fibers/tubes by co-electrospinning, mineral oil was used as the core material with polyvinylpyrrolidone and Ti(OiPr)<sub>4</sub> (in ethanol) as the shell material. After removal of the oil and calcinations, hollow titanium fibers were obtained.

Díaz et al.<sup>100</sup> described a utilization of electrified co-axial jets for encapsulating hydrophobic liquids in hydrophilic polymer melts, a product that would have applications in various technological fields, such as drug delivery. The process, in which a coaxial jet of polymer (outside) and a hydrophobic liquid (inner) is electrospun,

produces beaded fibers, encapsulating the hydrophobic liquid into these beads. The beads were regularly distributed along the fibers, and their size exhibits a mono- or bimodal distribution, depending on the operating conditions (mainly the inner liquid flow rate). Both the bead to- bead distance and fiber diameter were controlled by the outer liquid flow rate, while the bead diameter was controlled by adjusting the inner liquid flow rate.

Loscertales<sup>101</sup> reported the electrospinning of hollow and core/sheath nanofibers using a microfluidic manifold. They showed the multi-source microfluidic device enables parallel fiber electrospinning, making the process efficient and versatile for large scale production of nanofibers.

Dror et al.<sup>35</sup> reported one-step production of polymeric micro-tubes by co-electrospinning. With the choice of appropriate solvent combinations, they produced hollow core-shell fibers. Upon evaporation of the solvent, the core polymer precipitated on the walls of the previously formed shell.

Co-electrospinning have been successfully applied to encapsulated drugs, nanoparticles, nano-tubes, nano-rodes, enzymes and liquids or non-fiber-forming materials into electrospun fibers<sup>28,29,30,32,33,34,102</sup>.

The growth of multiwall carbon nanotubes on carbon nanofibers created hierarchical structures which can lead to the design and construction of electrodes, on a much smaller scale than heretofore possible, for fuel cells, batteries, electrochemistry, and the control of bioelectric potentials at the cellular level<sup>103</sup>.

Ceramic, carbon, and metal nanofibers were created from polymeric nanofibers by electrospinning, followed by heat treatment and chemical reactions<sup>104, 105</sup>. Hydrocarbon nanofibers such as polyacrylonitrile were converted to carbon nanofibers by low temperature oxidation followed by heating in an inert atmosphere. Ceramic nanofibers were made from organo-metallic sols by heating in an oxidizing atmosphere, or, in at least a few cases, to a metal fiber or nanowire, by heating in a reducing atmosphere.

Doiphode et al.<sup>106</sup> developed a method for creating polymer nanofibers and spheres on a variety of substrates. Cyanoacrylate monomer vapor was collected on a solid surface and polymerized to form nanofibers. Tiny spots of initiator on the surface of a substrate and small monomer droplets in a monomer vapor were required for the growth of the polycyanoacrylate nanofibers. The polycyanoacrylate nanofibers created a network and increased the specific surface area significantly.

Kessick, Fenn and Tepper<sup>107, 108</sup> published studies on electro spraying and electrospinning utilizing AC potential. They electro sprayed carboxymethylcellulose (CMC) onto semiconducting and insulating substrates using DC and AC potentials. On the semiconducting substrate, both AC and DC methods were capable of producing significant CMC coverage. However, only the AC potential was capable of producing significant coverage on the insulating substrate, possibly due to a reduction in the amount of surface charging. They electro spun poly (ethylene oxide) (PEO) fibers into mats using both DC and AC potentials. The AC potential resulted in a significant reduction in the amount of electrical bending instability of the electrospinning jet and

the resulting mats exhibited a higher degree of fiber alignment. The average fiber diameter for both DC and AC-spun mats exhibited a strong dependence on solution concentration. When a pure AC potential was used, the net charge on the fiber was very small resulting in a correspondingly small attractive force between the fiber and the collecting electrode, making fiber collection somewhat challenging.

Sarkar, Deevi and Tepper<sup>109</sup> introduced a method for minimizing the inherent electrical bending instability in the electrospinning. The method, dubbed “biased AC electrospinning”, employed a combination of DC and AC potentials and resulted in highly-aligned mats of polymer or composite polymer fibers. The applied AC voltage introduced alternating positively and negatively charged regions in the fiber, resulting in a decrease in electrostatic repulsion and an increase in fiber stability. The DC potential gave the net surface charged and enhanced the interaction between the jet and the collector then facilitated the collecting of the electrospinning jet. The relationship between specific processing variables such as the AC frequency and the magnitude of the DC offset was investigated and related to the resulting fiber stability and uniformity. When the AC frequency fell within a relatively narrow range the electrical bending instability was damped dramatically. The upper and lower frequency limits were measured for a small group of polymers and polymer composites and were qualitatively related to solution properties and processing variables. They concluded that the magnitude of the DC bias must be less than half the total amplitude of the AC potential and the AC frequency should be between 500 and 1000 Hz for optimum fiber stability.

aligned electrospun fibers but with only a limited success. Examples include increasing the rotational speed of the collecting drum, introducing a potential across a gap or series of gaps in the collecting electrode, introducing an external lens element or a viscous liquid environment, or rapidly oscillating a grounded frame within the liquid jet. All of these methods rely on minimizing the fiber instability by applying external forces on the fibers during production.

Dersch et al.<sup>110</sup> collected well aligned electrospun fibers by using a grounded collector with two parallel electrodes. Theron, Zussman and Yarin<sup>111,112</sup> reported a technique for the hierarchical assembly of nanofibers into crossbar nanostructures. By controlling the electrostatic field and the polymer rheology, the nanofibers were assembled into parallel periodic arrays. They collected the electrospun fibers on a flat table located on the edge of a rotating disk. When the rotation rate was high enough (5 m/s), the fibers were straightened by both mechanical and electrical repulsion forces during wrapping. Sundaray, Subramanian and Natarajan<sup>113</sup> reported the formation of aligned polymer fibers, several centimeters in length, with separation between the fibers in the range of 5 to 100 mm. They employed about 4500 V and a separation distance of about 1 to 3 cm between the electrodes. Smaller distance between electrodes provided better control on the formation of the fibers. Li et al.<sup>114,115,116</sup> generated uniaxially aligned electrospun fibers arrays over large areas using a collector composed of two conductive strips separated by an insulating gap of variable width. Mutli-layered architectures with controllable hierarchical structures were manufactured. Li et al.<sup>114, 115,116</sup> studied the effect of the area and geometric shape of the insulating gap

on the deposition of fibers. By modeling the electrostatic forces acting on the fiber, it was established that the fibers tended to be oriented along a direction such that the net torque of electrostatic forces applied to the two ends of a discrete segment of the fiber were minimized. By varying the design of electrode pattern, it was possible to control both alignment and assembly of the electrospun nanofibers. Katta, Alessandro, Ramsier and Chase<sup>117</sup> presented a simple method for spinning sheets with one centimeter wide strips of aligned nanofibers. Their technique utilized copper wires spaced evenly in the form of a circular drum as a collector of the electrospun nanofibers. Smit, Buttner and Sanderson<sup>118</sup> made continuous uniaxial fiber bundle yarns from electrospun fibers. The technique consisted of spinning onto a water reservoir collector and drawing the resulting non-woven web of fibers across the water before collecting the resulting yarn. Kameoka<sup>13</sup> et al. published work on the scanning tip electrospaying technique and later they applied similar setup to electrospinning. Kameoka and Craighead<sup>14</sup> fabricated oriented polymeric nanofibers on planar surfaces using electrospinning from an integrated microfluidic device. A triangular-shaped polymeric film was lithographically fabricated and aligned at the exit of an embossed microfluidic channel. This tip acted as a wick and helped to establish a Taylor cone. The apex angle of the triangular thin film was 90° and the thickness was 3 μm. The electrospinning device was placed on a linear translation stage and the deposition distance between the tip and a counter electrode was 2 cm. A 300 nl/min polymer solution flow rate was created with a syringe pump, connected to the pipette reservoir by silica capillary tubing. A voltage of 3 to 4 kV was applied to the gold wire in the reservoir to establish a Taylor cone. A silicon counter

electrode was attached to a speed-controlled rotating motor. The linear velocity of the counter electrode relative to the microfabricated electrospinning source was varied from 0 to 168 cm/s. They successfully fabricated oriented polyethylene oxide nanofibers using this device. The orientation of nanofibers was controlled by the linear velocity of the counter electrode relative to the source. This ability to deposit nanowires oriented with respect to surface electrodes or other nanowires enabled rapid formation of molecular electronic architecture, sensor, detector, field effect transistor, and light emitting devices<sup>15, 16, 17,119,120,121,122</sup>.

Sun, Chang, Li and Lin<sup>123</sup> developed a near-field electrospinning (NFES) process to deposit solid nanofibers in a direct, continuous, and controllable manner. A tungsten electrode with tip diameter of 25  $\mu\text{m}$  was used to construct nanofibers of 50 to 500 nm line width on silicon-based collectors while the liquid polymer solution was supplied in a manner analogous to that of a dip pen. The minimum applied bias voltage was 600 V, and minimum electrode-to-collector distance was 500  $\mu\text{m}$  to achieve position controllable deposition. NFES is a simple yet powerful method for direct-write deposition of nanofibers with unprecedented controllability at resolutions comparable to those achieved with much more expensive and sophisticated lithography tools.

## CHAPTER III

### ELECTRICAL BENDING INSTABILITY IN ELECTROSPINNING JET

#### 3.1 INTRODUCTION

The electrospinning jet is a continuous fluid flow ejected from the surface of a fluid when the applied electrical force overcomes the surface tension<sup>1</sup>. The jet moves straight away from the tip for some distance and then becomes unstable and bends into coiled loops (Figure 3.1), this instability phenomenon is well-known as electrical bending instability<sup>5,6</sup>. When the distance between spinneret and grounded collector is reduced to less than the length of the straight segment, the electrical bending instability does not occur instead only a straight jet is produced. (Figure 3.2)

Zeleny<sup>46</sup> recorded the motion of electrified liquid jets. He reported electrical force acting on some of the fine threads of liquid often underwent very rapid changes in direction on account of the liquid droplets in front.

Taylor<sup>55</sup> discovered in a parallel electrical field an electrically driven water jet bent into spiral coils under some conditions. He explained this type of instability is due to the competition between viscous stress along the jet and electrostatic force working on the jet. When the electrostatic force is higher, it overcomes the viscous stress and elongates the jet. When the electrostatic force is so low that it cannot support the jet against the contracting viscous stress, the jet becomes unstable, analogous to that of

Euler buckling when an elastic column is axially compressed. Jet diameter stops decreasing after the bending instability starts which means the strong stretching of the electrospinning jets stops along the bending spiral loops.

Reneker, Yarin and coworkers<sup>5,6</sup> published the theoretical modeling of the electrospinning jet. Their model successfully explained the onset and development of the electrical bending instability in an electrospinning jet. They modeled the polymer jet by a linear Maxwell equation. Columbic repulsions between charges on the jet surface generate bending forces that destabilize the jet and introduce the electrical bending instability. Jet paths calculated from the model agree well with the experimental observations. Strain rate in the straight segment of the electrospinning jet is in the 20  $\text{sec}^{-1}$  range and up to 100000  $\text{sec}^{-1}$  in the bending spiral loops which suggest strong orientation and stretching of the molecular chains.

Electrical bending instability gives the electrospinning jets enough space and time to be thinned and solidified into submicron sized fibers. At the same time the electrical bending instability bring difficulties for the orderly collection of the electrospun fibers because the random distribution of the bending spiral loops in the space. Usually the electrospun fibers are collected in a non-woven cloth mat.

The methods applied to orderly collect the electrospun fibers are mainly relying on the fast picking up of the electrospun fibers. In these methods, the mechanical rotating devices which have high rotating speed are used and the rotating speeds have to be high enough to match with the spread out speeds of the bending spiral coils which are usually in the 10 m/s range.

The scanning tip electrospinning technique<sup>13, 14,15,16,17</sup> and the near field electrospinning technique<sup>123</sup> make the orderly collection of the electrospun fibers easier which do not require very high picking up speed. Actually scanning tip electrospinning technique and near-field electrospinning technique are identical and they utilize the straight electrically driven jets (Figure 3.2) with small initial jet diameters. These straight electrically driven jets don't have electrical bending instability (or maybe only a couple of bending loops at the very end of the jets) which can be easily orderly collected by a moving collector.



Figure 3.1 Electrospinning jet with electrical bending instability

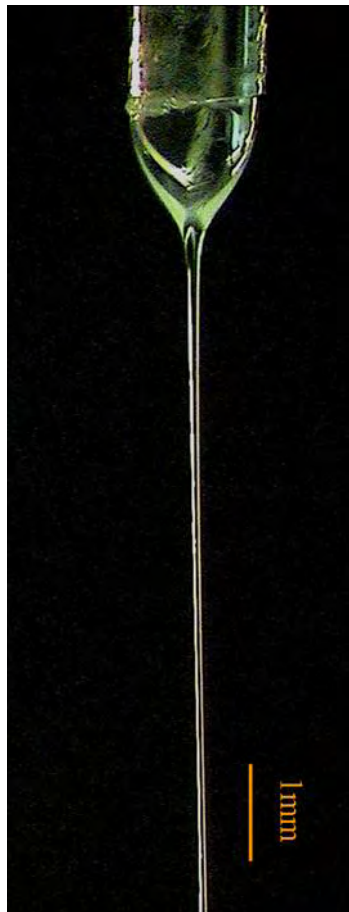


Figure 3.2 Straight electrified jet

From these previous research works we can see that the determination of the behavior of the jet path in the vicinity of the onset of the first electrical bending instability is important for the orderly collection of the nanofibers produced by electrospinning. And here are no direct experiment results ever reported about the onset and the development of the electrical bending instability in the electrospinning jets. All the experiment results reported are about the fully developed bending spiral coils. In this chapter, the direct experimental observation about the onset and the

development of the electrical bending instability will be presented. And the morphologies of the electrospun fibers produced under different stages of the electrospinning jet will be discussed.

### 3.2 EXPERIMENTAL

Polyethylene oxide (PEO),  $M_w=400,000$  g/mol, 6wt% solution in deionized water; Poly (-L-lactide) (PLLA),  $M_w= 152,000$  g/mol, 5% solution in Hexafluoroisopropanol (HFIP); Nylon-6, 10% solution in HFIP/Formic acid mixture, HFIP:Formic acid =8:2 (weight ratio). All polymers used were purchased from Scientific Polymer Products. All solvents used were purchased from Sigma-Aldrich Company.

The polymer solutions were held in a glass pipette which has a 2 cm long capillary at one end. The capillary's inner diameter was 160  $\mu\text{m}$ . A copper wire was immersed in the solution and connected with a high voltage power supplier which could generate DC voltage up to 13 kV. A grounded plate was placed below the capillary tip served as the collector, it could move at the speed of 0 m/s to 3 m/s. The distance between the capillary and the collector could be adjusted from 1 mm to 100 mm. An ampere meter was connected between the collector and the grounded wire which was used to measure the current carried by the electrospinning jet.

The collected fibers were observed with optical microscopy and scanning electron microscopy (JEOL 5310 Scanning Electron Microscopy, Olympus 51BX Optical Microscopy).

### 3.3 RESULTS AND DISCUSSIONS

Electrical bending instabilities as functions of distance from the orifice and applied voltages are discussed. Onset of the bending instability and morphologies of electrospun fibers are presented.

#### 3.3.1 Electrical bending instability as a function of distance from the orifice

The onset of the electrical bending instability was investigated by continuously increasing the distance from the orifice to the collector. An inclined grounded collector was placed beneath the electrospinning spinneret (Figure 3.3). The perpendicular distance from the orifice to the collector was set at 1 mm and then the inclined collector was moved laterally. PEO in an aqueous solution was used. The distance between the orifice and the collector surface was continuously increased to 75 mm as the inclined collector moved. The voltage between the spinneret and the collector was 5.4 kV. A flash camera and a high speed camera were used to record the morphology of the jet path (Figure 3.4). The Fresnel lens produced a converging cone of white light at the location of the electrospinning jet. The opaque disk on the Fresnel lens prevented light from the Xenon arc lamp from entering the camera, but enough light scattered by the jet entered the camera and recorded the path of the jet.

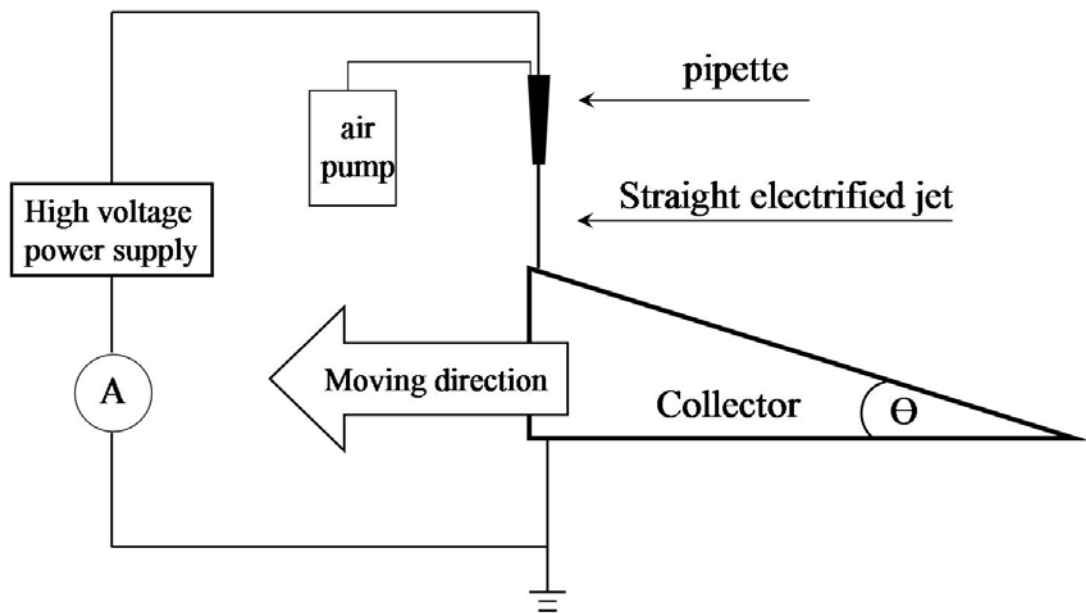


Figure 3.3 Schematic drawing of electrospinning setup with movable inclined collector.

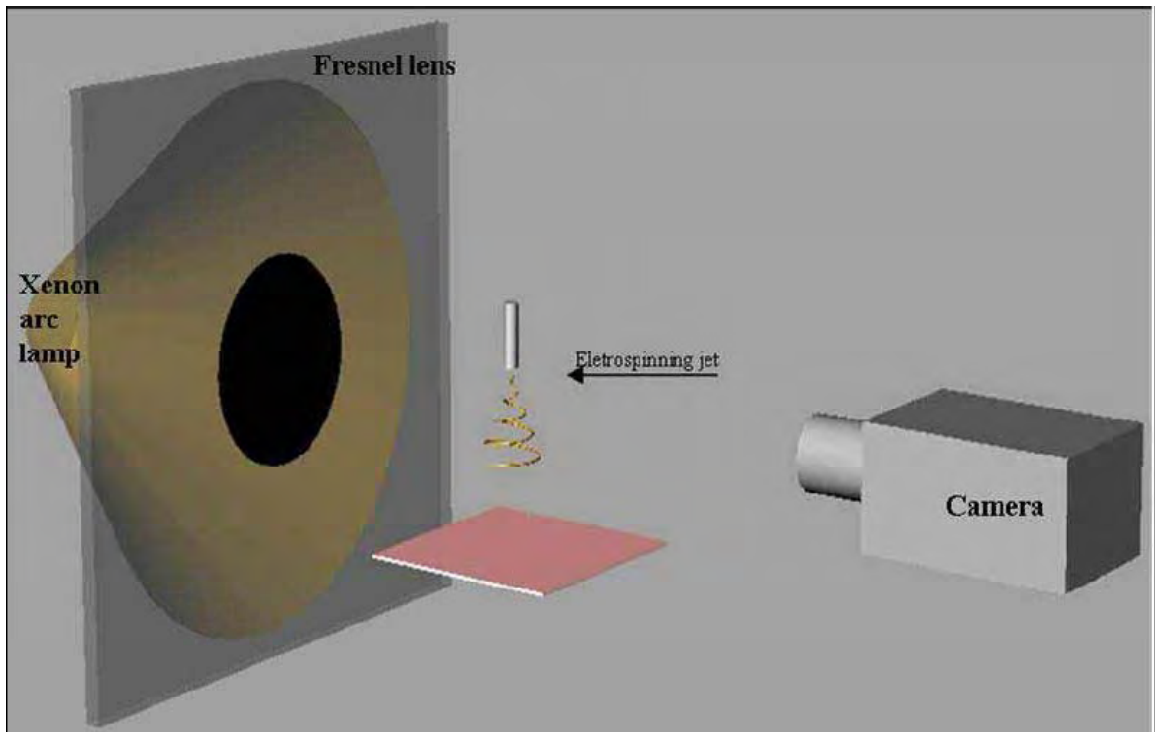


Figure 3.4 Camera set up for the observation of electrospinning jet.

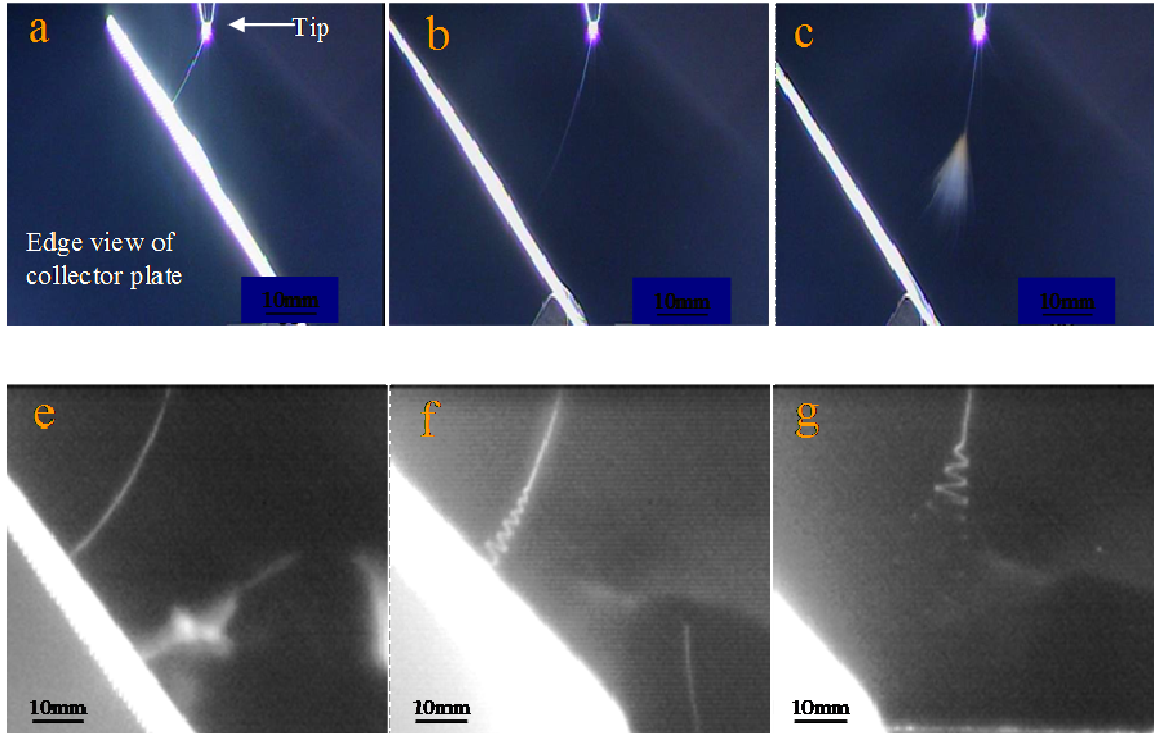


Figure 3.5 a, b, c are from video camera (60 frames/second) images of an electrospinning jet at different collector parameters; e, f, g are high speed camera images (2000 frames/second; shutter speed 1/10,000) of the electrospinning jet. The distances from the orifice to the grounded collector ( $H$ ) increased from left to right. For a and e,  $H=25$  mm; for b and f,  $H=53$  mm; for c and g,  $H=75$  mm. The edge of the collector, seen as a broad white line showed the inclination.

Figure 3.5 shows time averaged (a, b, c) and instantaneous (e, f, g) paths of the electrospinning jet at different distance between the orifice and the collector. When the jet left the orifice, it moved to the collector and produced a straight jet. No electrical bending instability was observed when the orifice to collector distance was short. Both the digital camera image (Figure 3.5-a) and the high speed camera image (Figure 3.5-e)

showed an essentially straight jet. When the distance increased to 53 mm in this experiment, the digital camera showed a blurred image (Figure 3.5-b) of the jet and the high speed camera image (Figure 3.5-f) showed that electrical bending instability had occurred. The coiled loops grew in radius and propagated along a slightly curved electric field line as they moved downwards at a speed of about 2 m/s to 5 m/s.

With increasing collection distance, the digital camera (Figure 3.5-c) showed interference colors indicating that the jet had a diameter of more than 10  $\mu\text{m}$  at the top and about 2  $\mu\text{m}$  at the onset of the electrical bending instability; the high speed camera (Figure 3.5-g) showed clearly the coiled loops of the electrical bending instability. Before the electrical bending instability, the path curved so that the jet approached the plane of the collector in a more nearly perpendicular direction. In each repetition of this experiment, one single trace of the electrospun fiber was collected on the laterally moving collector.

The optical and scanning electron microscopy images (Figure 3.6- a<sub>1</sub> to Figure 3.6- c<sub>2</sub>) showed the changes in the collected fibers as the orifice to collector distance increased. The straight electrospinning jet produced conglutinated fibers and buckled fibers (Figure 3.6-a<sub>1</sub>). These fiber segments had a wide diameter distribution that ranged from 300 nm to 1  $\mu\text{m}$  (Figure 3.6- a<sub>2</sub>). After the start of an electrical bending instability, the jet produced loops (Figure 3.6- b<sub>1</sub>) with diameters ranging from 50 to 200  $\mu\text{m}$ . Figure 3.6- b<sub>2</sub>, b<sub>3</sub> showed short segments of the electrical bending instability coils in Figure 3.6- b<sub>1</sub> at a higher magnification. The amount of conglutination was smaller than that shown in Figure 3.6-a<sub>2</sub>, a<sub>3</sub>. The segments of fibers in Figure 3.6- c<sub>1</sub> were collected after the

electrical bending instability loops were much larger than the area shown. The segments shown are only slightly curved. Some segments have nearly periodic curved shapes and small loops that are characteristic of buckling. Figure 6- c<sub>3</sub> showed an enlarged image of a loop made by buckling.

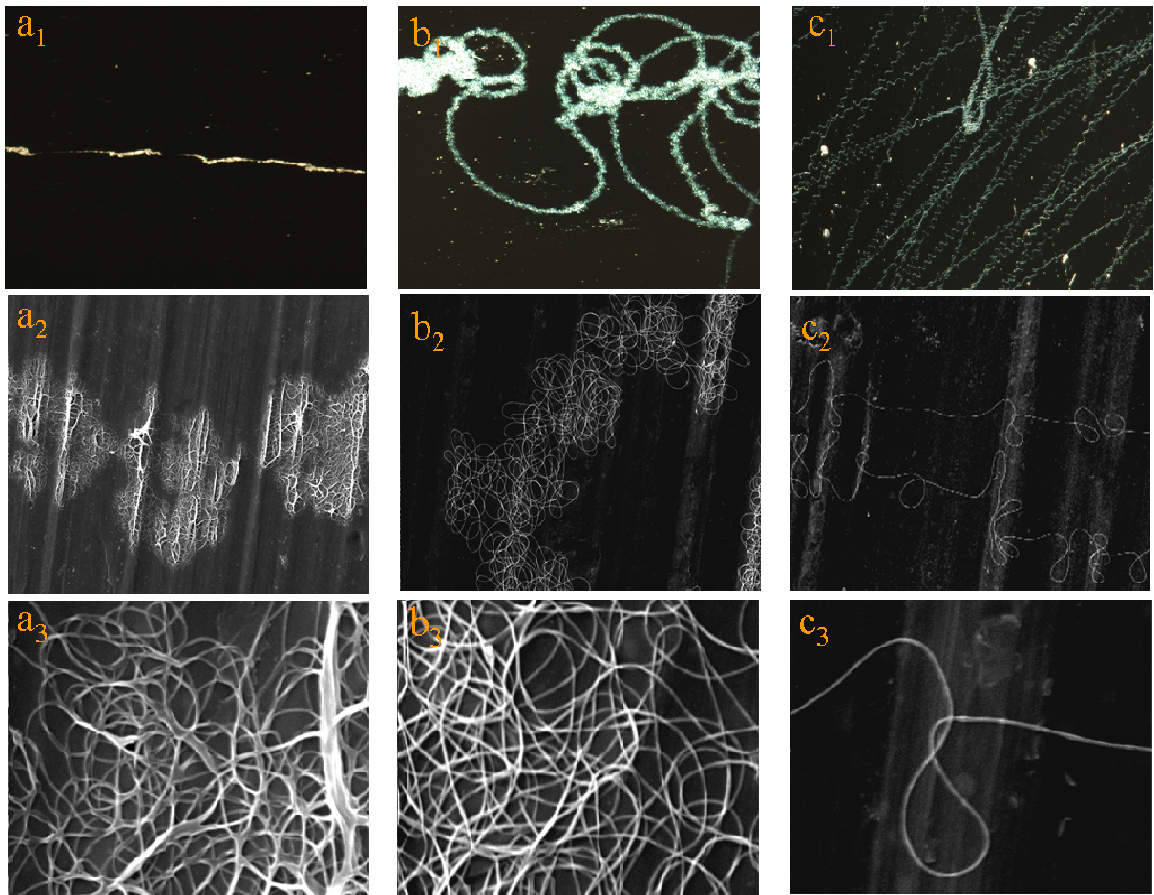


Figure 3.6 Optical microscopy images (a<sub>1</sub>, b<sub>1</sub>, c<sub>1</sub>) and scanning electron microscopy images (a<sub>2</sub>, b<sub>2</sub>, c<sub>2</sub>; a<sub>3</sub>, b<sub>3</sub>, c<sub>3</sub>) of electrospun fibers. The length of the horizontal edges of the optical microscopy images (a<sub>1</sub>, b<sub>1</sub>, c<sub>1</sub>) are 450 μm; The length of the horizontal edges of the SEM images are 65 μm (a<sub>2</sub>, b<sub>2</sub>, c<sub>2</sub>) and 13 μm (a<sub>3</sub>, b<sub>3</sub>, c<sub>3</sub>) . The distance from the orifice to the collector was about 25 mm in a<sub>1</sub>, a<sub>2</sub>, a<sub>3</sub>; 53 mm in b<sub>1</sub>, b<sub>2</sub>, b<sub>3</sub> and 75 mm in c<sub>1</sub>, c<sub>2</sub>, c<sub>3</sub>.

### 3.3.2 Electrical bending instability as a function of applied voltage

The PEO aqueous solution held in the pipette was connected to the power supply. The distance from the orifice to the horizontal grounded collector was 53 mm. The high frame rate camera was used to observe the jet path. The voltage applied between the pipette and the collector was continuously increased from 0 kV to 13 kV by increase 0.1 kV every step.

The dripping of the liquid from the end of the pipette was observed when the applied voltage was set from 0 kV to 2 kV. An electrospinning jet with electrical bending instability was observed between 3 kV to 5.4 kV. A straight electrified jet was observed between 5.5 kV to 11 kV. When the applied voltage was above 11 kV, the multi-jets ejected from the tip of the pipette were observed. From these results we came to the conclusion that when the distance is set as 53 mm, here is a transition between the onset and disappear of the electrical bending instability when the applied voltage is between 5.4 kV and 5.5 kV.



Figure 3.7 High frame rate camera images of the onset and development of the electrical bending instability along an electrically driven jet. The time at which the voltage was lowered is shown in the upper left corner.

### 3.3.3 Onset of an electrical bending instability in the straight segment

The PEO aqueous solution held in the pipette was connected to the power supply. The distance from the orifice to the horizontal grounded collector was 53 mm. The high frame rate camera was used to observe the jet path.

The straight segment of the jet extended from the orifice to the collector when the voltage was set at 5.5 kV. Then after the second frame, the voltage was reduced in a short time to 5.4 kV. The reduced voltage led to a thinner jet which has lower bending stiffness. The electrical bending instability began to form about 36 mm below the orifice (Figure 3.7, 0.5 ms). In 1.5 ms the instability was carried down to about 43 mm (Figure 3.7, 2.0 ms). At 3.0 ms a new electrical bending instability occurred at about 30 mm (Figure 3.7, 3.0 ms). At 4.5 ms, the coils of the first electrical bending instability were about to move out of the field of view. A new instability developed at about 30 mm (Figure 3.7, 4.5 ms) and developed more fully. At 6.0 and 7.5 ms, the electrical bending instability started at 30 mm and moved downward at a velocity of 4 m/s (Figure 3.7, 6.0 ms, 9.0 ms). From this series of images we found that the frequency of the electrical bending instability was in the range of  $10^3$  to  $10^4$  Hz. If the voltage was increased to 5.5 kV, the onset of the electrical bending instability moved downward and the straight segment reached to the collector.

### 3.3.4 Electrospun fibers produced by a straight electrified jet

The PEO aqueous solution held in the pipette was connected to the power supply. The distance from the orifice to the horizontal grounded collector was 1.6 cm.

The applied voltage was set at 2.0 kV. A rotating drum (diameter = 10 cm) was used as collector which can rotate at 0 to 3000 rpm. The collected fibers were characterized by Scanning Electron Microscopy. (Figure 3.8)

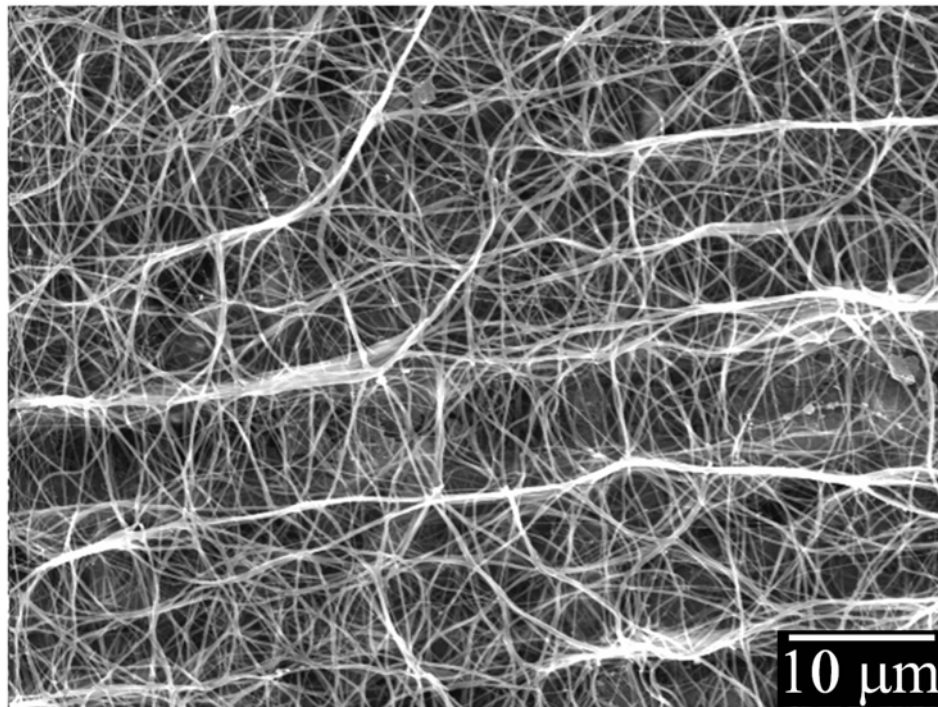


Figure 3.8 Electrospun fibers produced by a straight electrified jet.

(a) collected by a static collector.

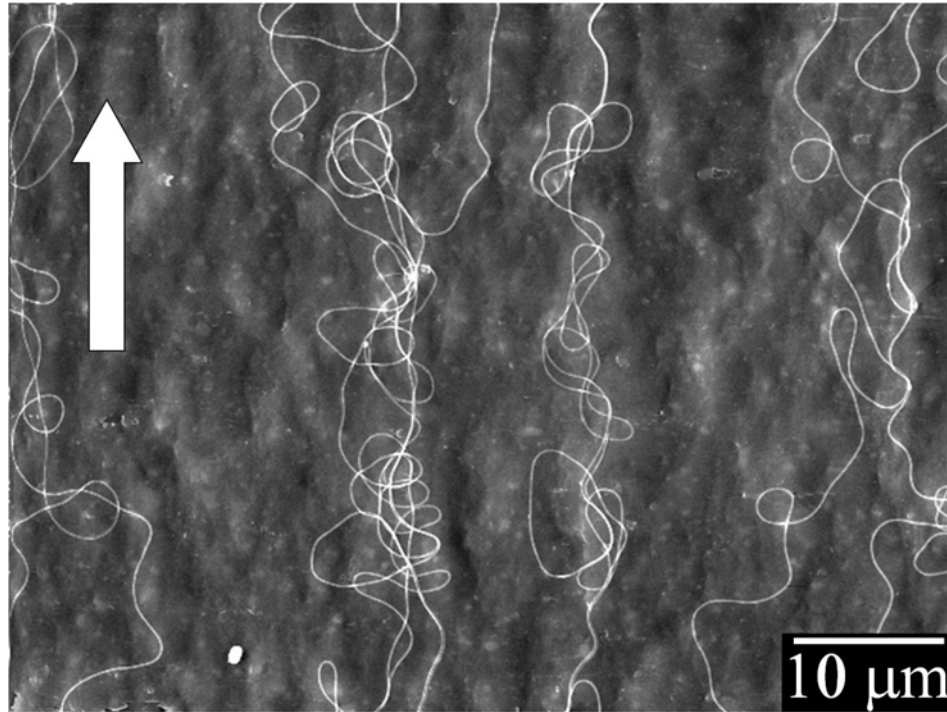


Figure 3.8 Electrospun fibers produced by a straight electrified jet.(continued)

(b) collected by collector moving at 0.785 m/s.

The bright white arrow represents the moving direction of the collector.

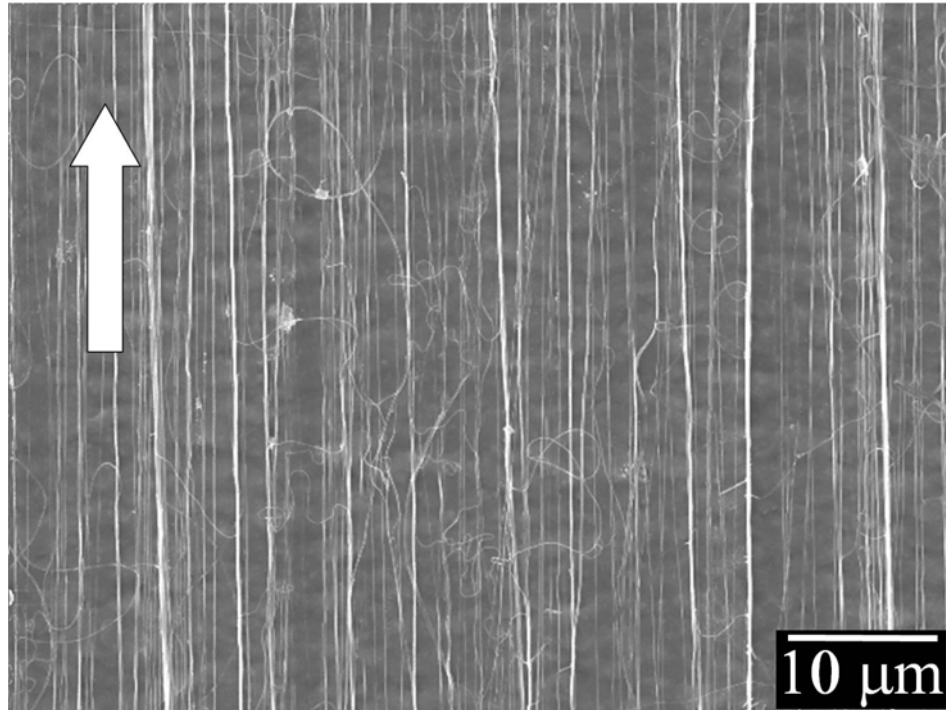


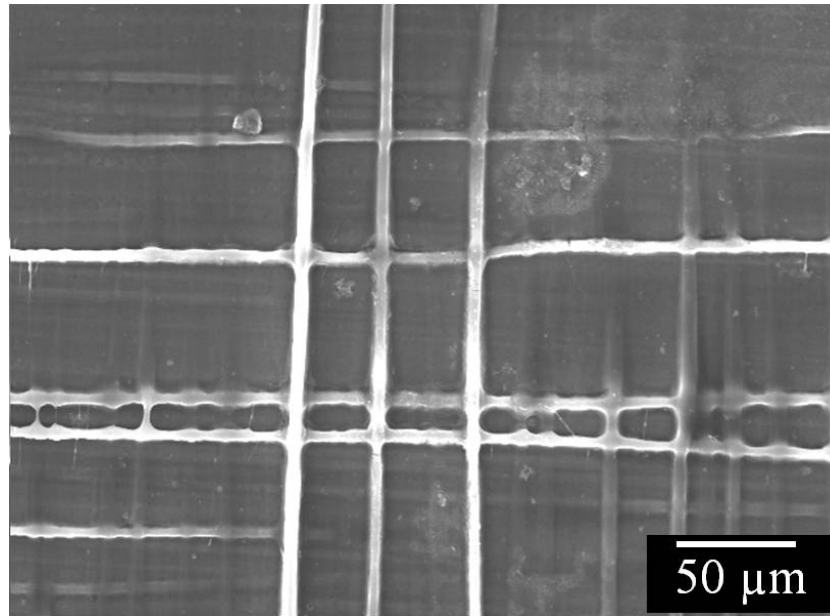
Figure 3.8 Electrospun fibers produced by a straight electrified jet. (continued)

(c) collected by collector moving at 1.57 m/s.

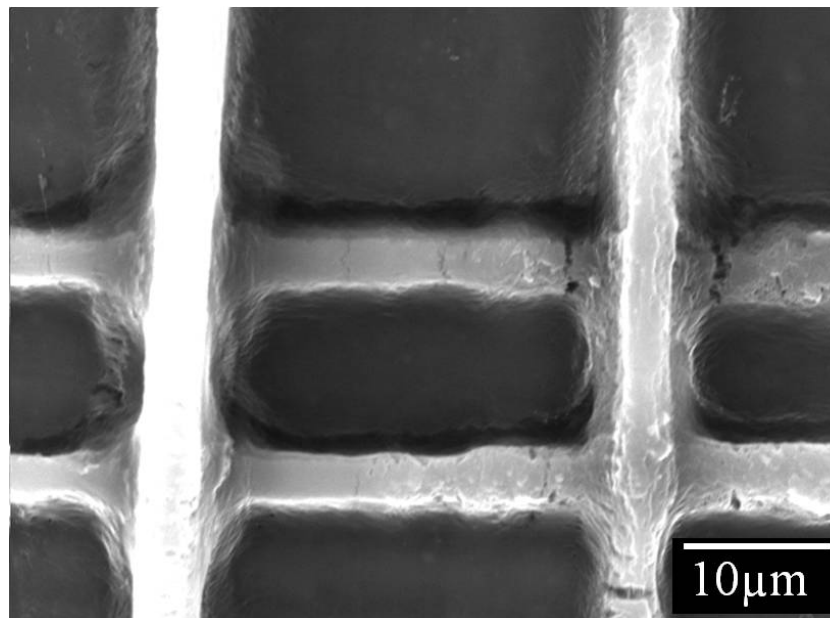
The bright white arrow represents the moving direction of the collector.

Figure 3.8 showed the SEM images of electrospun fibers produced by collecting a straight electrified jet on a collector located on the surface of a rotating drum. The surface velocity of the rotating drum can be adjusted from 0 to 2.5 m/s. Figure 3.8-a, the collector was static; the electrospun fibers showed non-woven mat morphology. Figure 3.8-b, the collector was moving at speed of 0.785 m/s; the curved fibers were partially aligned along the collector moving direction dedicated by the bright white arrow. Figure 3.8-c, the collector was moving at 1.57 m/s; the straight fibers were well aligned along

the collector moving direction. The diameters of the electrospun fibers were around 300 nm and not affected by the moving speed of the collector greatly.



(a)



(b)

Figure 3.9 Two-dimensional patterns made from electrospun fibers.

Figure 3.9 showed the two-dimensional structures produced by collecting a straight electrified jet on a moving collector. The collector was moving at 1.57 m/s. The fibers were collected over 10 second period and then stopped. The collector was rotated 90 degree and then the fibers were collected on the rotating collector for another 10 second. The separation between the parallel fibers varied from 1  $\mu\text{m}$  to 20  $\mu\text{m}$ .

### 3.4 SUMMARY

Electrical bending instabilities of an electrospinning jet collected on a solid surface, at a continuous series of distances from the orifice from which the jet emerged were observed. The frequency of the electrical bending instability was in the range of  $10^3$  Hz. Increased voltage delayed the onset of the electrical bending instability and produced a longer straight segment in an electrospinning jet. Under certain conditions, high applied voltage delayed the onset of the electrical bending instability and the straight segment reached to the collector. Electrospun fibers were produced by collecting a straight electrified jet on a moving collector. A minimum collector velocity was needed to produce straight fibers. When the collector velocity was below this minimum value, buckled fibers were produced. The resulting two-dimensional structures were periodical arrays which can be used in microelectronics, bio-medical device for example.

## CHAPTER IV

### INVESTIGATION OF THE DIAMETER, VELOCITY, AND LONGITUDINAL STRESS PROFILE OF THE ELECTROSPINNING JETS

#### 4.1 INTRUCTION

The electrospinning jet is a continuous fluid flow ejected from the surface of a fluid when the applied electrical force overcomes the surface tension<sup>1</sup>. The jet moves straight away from the tip for some distance and then becomes unstable and bends into coiled loops. The jet is a micro scale, tapered and electrically charged fluid flow with a high tensile stress along the axis. The nature of the jet creates many difficulties in characterizing its diameter, velocity, elongation strain rate and longitudinal stress along the jet axis<sup>124</sup>. The chaotic electrical bending instability makes the characterization of these parameters along the bending spiral loops of electrospinning jets even more difficult. No successful experiments have ever been done to directly measure these parameters along the bending spiral loops. So far, all the measurements are mainly dealing with the straight segment of the electrospinning jet or the straight electrified jet.

Doshi and Reneker used a laser diffraction method to measure the diameter of the straight segment of the electrospinning jet<sup>125</sup>. A straight jet was treated as a double slits to approximate the size of the jet from the diffraction pattern. The distance between the first constructive interference and the central bright peak was used to

calculate the jet diameter. Xu<sup>124</sup> used a single slit diffraction method measure the diameter of an electrospinning jet. Optical imaging was used by Koombhongse to study the jet development during electrospinning<sup>126</sup>. Interference color model was introduced to characterize the jet diameter by Xu<sup>124</sup>. The diameter of the straight jet was measured by analyzing the color pattern which was produced when a polychromatic light beam was diffracted by the cylinder jet.

Doshi<sup>125</sup> measured the velocity of the jet by Laser Doppler Velocimeter<sup>125</sup>. A particle tracing technique was applied to measure the diameter of the electrospinning jet by Xu<sup>124</sup>. The velocity of the jet also can be calculated indirectly based on the volumetric flow rate and the jet diameter profile.

Up to now, no experiment has ever been done to measure the longitudinal stress along the electrospinning jet.

In this chapter, jet diameter and jet velocity measured by methods mentioned above are presented. A novel method of characterization of viscoelastic longitudinal stresses in electrospinning jets of semi-dilute and concentrated polymer solutions and melts is introduced.

## 4.2 THEORETICAL BACKGROUND

Theoretical principles and mathematic descriptions of various characterization techniques will be discussed in this chapter.

#### 4.2.1 Measurement of the jet diameter

Double slits laser diffraction, single slit laser diffraction, interference color model and optical microscopic imaging have been used to characterize the jet diameter.

##### 4.2.1.1 Double slits laser diffraction

In the double slits interference, the interference intensity at an observation angle  $\theta$  is:

$$I = 4I_0 \cos^2\left(\frac{\pi}{\lambda} d \sin\theta\right) \quad (4.1)$$

When the path length difference ( $d \sin\theta$ ) of the light coming from the two slits equals to an integral number of the wavelength, light wave add in phase and a constructive interference takes place (Eq. (4.2)). At these positions, intensity maximum show up. When the path length difference equals to an odd number of the half wavelength, light waves are out of phase and a destructive interference takes place (Eq.(4.3)). At these positions, intensity minimum show up.

$$d \sin\theta = \pm n\lambda, (n = 1,2,3 \dots) \quad (4.2)$$

$$d \sin\theta = \pm(2n - 1)\frac{\lambda}{2}, (n = 1,2,3 \dots) \quad (4.3)$$

Where,  $\theta$  is the diffraction angle or observation angle

$\lambda$  is the wavelength of the light

$d$  is the spacing between two slits (diameter of the jet)

$n$  is the order of the interferences peak

The geometric relation is defined by

$$\sin\theta = \frac{D_n}{L} \quad (4.4)$$

Where  $D_n$  is the distance between the  $n^{\text{th}}$  order constructive or destructive interference and the central bright peak, and  $L$  is the distance from the double slit to the screen.  $D_n$  is measured from the digital image of the diffraction pattern on the screen, and then the diameter of the jet can be calculated from Eq. (4.2) and Eq. (4.3)

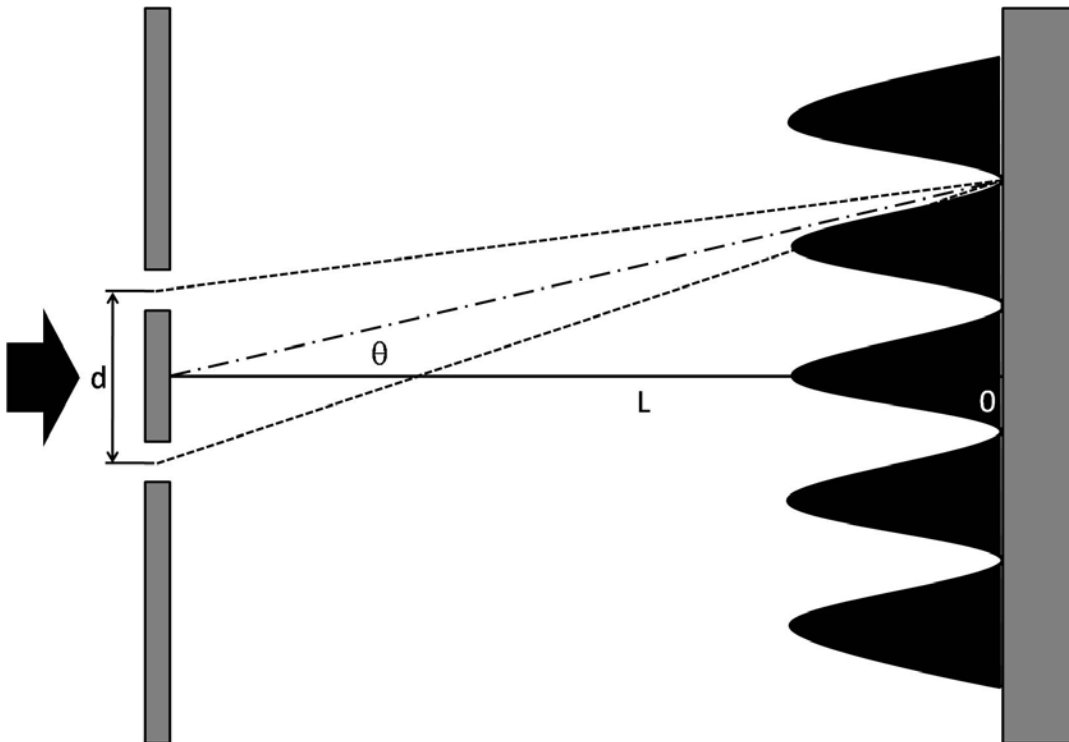


Figure 4.1 Young's double slits interference

#### 4.2.1.2 Single slit laser diffraction

When a laser illuminates a single slit, as demonstrated in Figure 4.2, a diffraction pattern will spread behind this slit. Huygens's Principle states that every point on a propagating wavefront serves as a source of spherical secondary wavelets, such that the wavefront at some later time is the envelope of these wavelets. In this case, the intensity on the screen is the summation of all the waves emitted from different positions along the slit.

$$I = I_0 \left( \frac{\sin \beta}{\beta} \right)^2 \quad (4.5)$$

$$\beta = \frac{\pi}{\lambda} d \sin \theta$$

$d$  is the length of the single slit

$\theta$  is the diffraction angle or observation angle

$\lambda$  is the incident beam wavelength

$I_0$  is the incident beam intensity.

The diffraction intensity at different angle is shown in Eq. (4.5). Since the light from the center of the slit differs by a half wavelength in phase and the overall effect produces destructive interference, one wavelength difference in path-length from the edges of the slit produces a minimum,. Thus, minimums are at those positions satisfying Eq. (4.6). Note that these positions would be for constructive interference in double slit interference.

$$d \sin \theta = \pm n \lambda, n = 1, 2, 3 \dots \quad (4.6)$$

Maximum positions calculated from  $\frac{d}{d\beta} \left(\frac{\sin\beta}{\beta}\right)^2 = 0$  are at

$$d \sin \theta = \pm 1.43 \lambda, \pm 2.46 \lambda, \pm 3.47 \lambda \dots \quad (4.7)$$

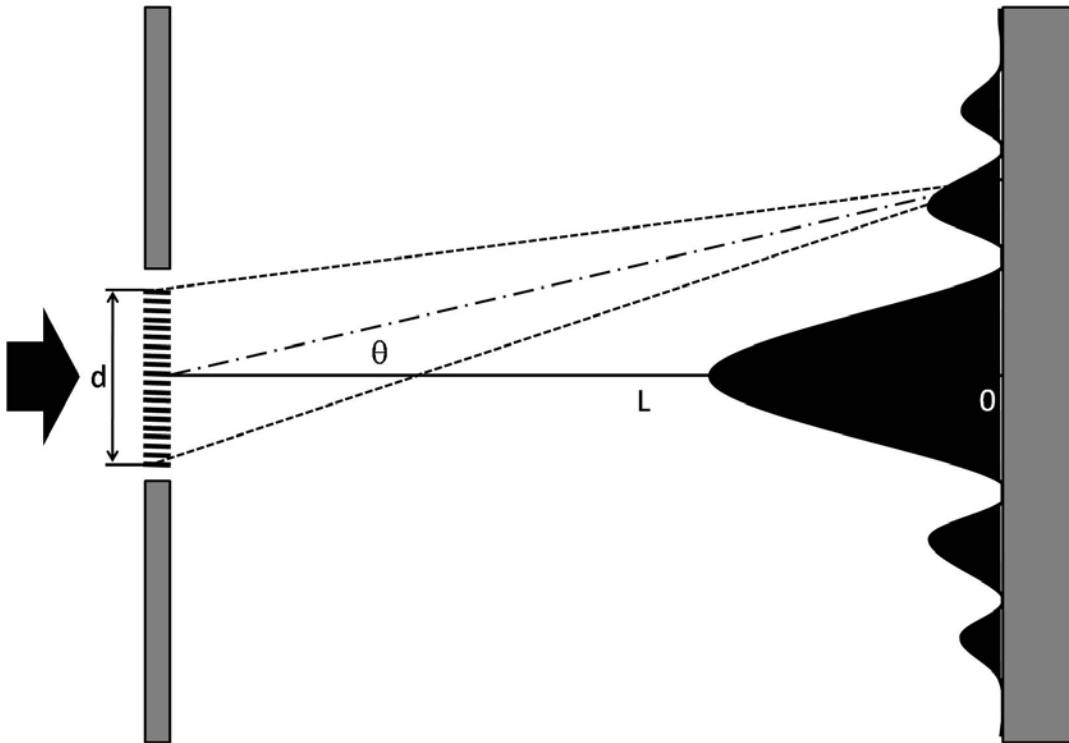


Figure 4.2 Single slit interference

In the single slit diffraction theory, an infinite number of secondary wavelets emitted along the slit were integrated to calculate the intensity on the screen. In the double slit interference theory, only two secondary wavelets emitted from the upper slit and the lower slit were considered. Since light waves were able to penetrate through the center of the cross section of the electrospinning jet, it was more appropriate to

approximate the cross section of a fluid jet as a single slit rather than as a double slit. The disadvantage of the laser diffraction technique was that it is difficult to get a nice measurement from the very beginning of the jet due to large diameter jet gives out narrowly separated diffraction pattern which is difficult to be analyzed. It was also difficult to get a clear diffraction pattern from the lower part of the straight jet due to the vibration. It was not possible to measure the jet diameter by this method when the jet path bent into spiral coils.

#### 4.2.1.3 Interference color model

When a polychromatic light beam incidents on a cylindrical jet, it will be diffracted by the jet to different angles according to the different wavelengths. These light waves produce constructive interference peaks at different positions on the screen. Colors are actually spread out and sorted according to their wavelengths. Camera set at a certain observation angle will be able to catch those colors entered its aperture.

The observed color patterned is determined by the diameter of the cylindrical jet as well as the observation angle. At a fixed observation angle, a certain color observed by the camera will correspond to a certain diameter of the jet that diffracts the incoming light (Figure 4.3). The advantage of the interference color technique consists in the fact that it allows an immediate estimate of local values of jet diameter just by naked eye observation.

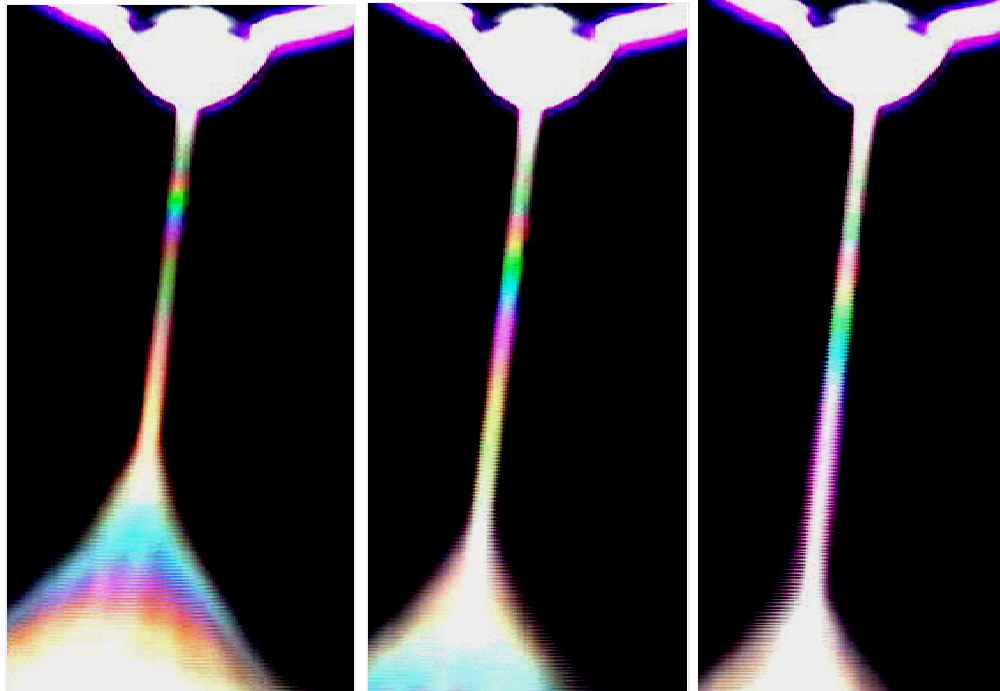


Figure 4.3 The observation of the interference colors along the jet axis

#### 4.2.1.4 Optical imaging

Optical imaging was used by Koombhongse to study the jet development during electrospinning<sup>126</sup>. As shown in Figure. 4.4, the optical picture taken by a camera connected with a microcopy give the information of the diameter profile of an electrospinning jet. Observation of a micron meter diameter jet requires very high magnification as well as elimination of vibrations. When jet diameter approaches the wavelength of light, optical imaging becomes inaccurate.

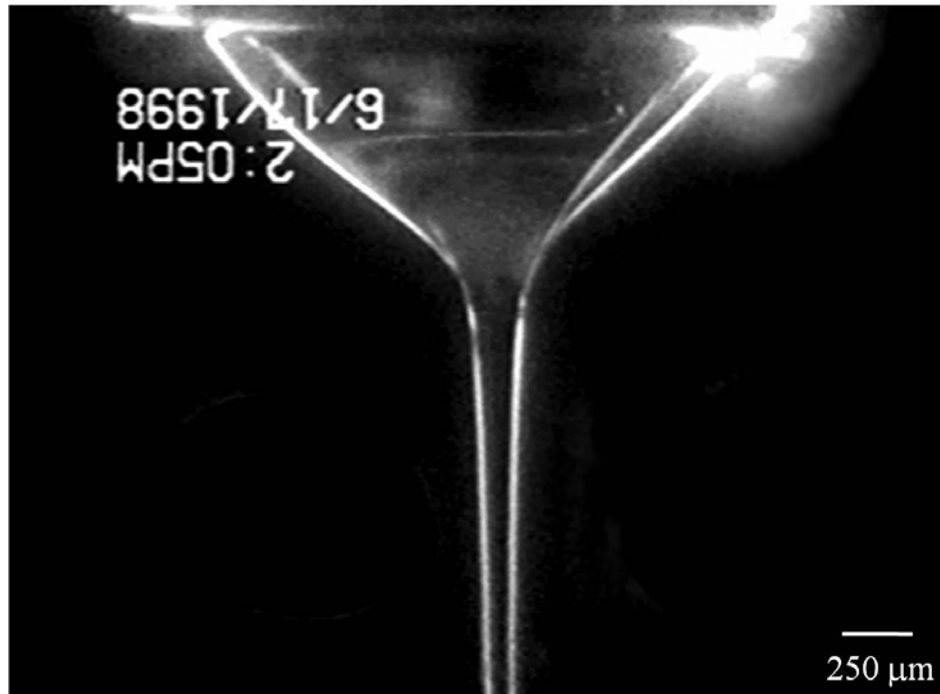


Figure 4.4 Optical image of the straight segment of an electrospinning jet<sup>126</sup>.

#### 4.2.2 Measurement of jet velocity

Laser Doppler Velocimeter, Particle tracing technique and indirect methods have been used to determine the jet velocity.

##### 4.2.2.1 Laser Doppler Velocimeter

Doshi<sup>125</sup> measured the velocity of the jet by Laser Doppler Velocimeter<sup>125</sup>. Two coherent monochromatic, linear, laser light beams were focused to cross at a small region by a small angle. At the crossing point of the beams, Young's interference fringes of known spacing are formed. When the electrospinning jet moved through this region, the particles imbedded in the jet scattered light whose intensity fluctuated with a

frequency related to the particles velocity. The jet velocity was calculated from the frequency spectrum (Figure 4.5) by Eq.(4.8).

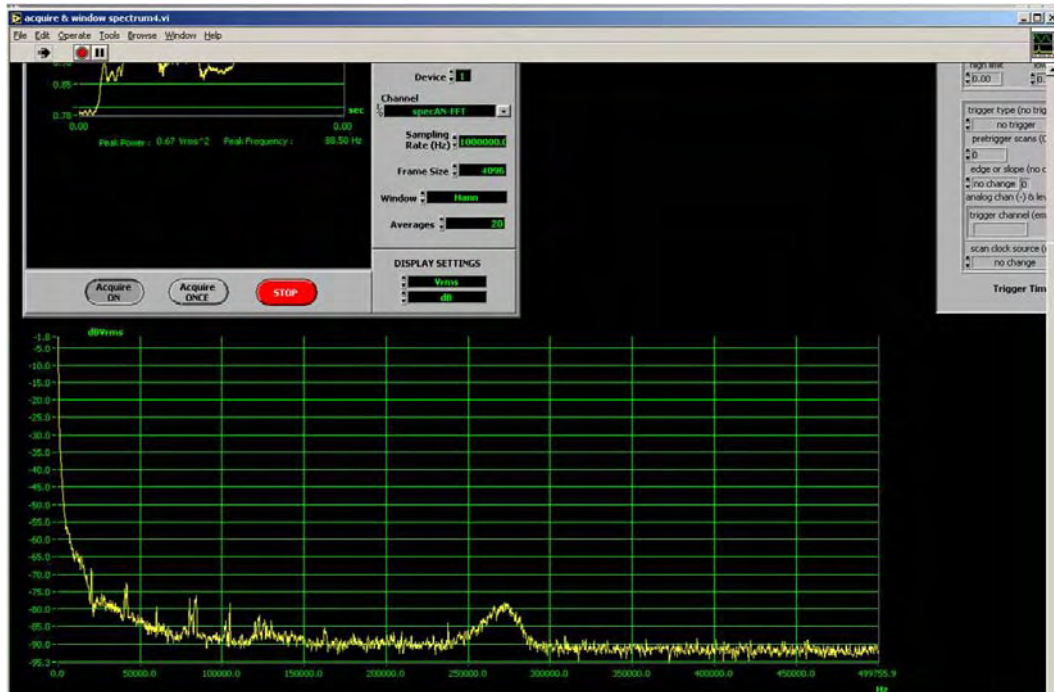


Figure 4.5 A typical frequency spectrum from the Laser Doppler Velocimeter.

$$V = \frac{\lambda f_D}{2 \sin(\frac{\theta}{2})} = 7.9 \mu m \times f_D \quad (4.8)$$

$f_D$  is the Doppler frequency read from the working window shown above

$\lambda$  is the wavelength of the laser light (632.8 nm)

$\theta$  is the angle between two incident laser beams (4.65°)

#### 4.2.2.2 Particle tracing technique

A particle tracing technique was applied to measure the diameter of the electrospinning jet by Xu<sup>124</sup>.

The speed at which the fluid jet travels along its axial is an essential parameter to calculate the stain rate during electrospinning. A particle tracing technique was used to characterize the electrospinning jet velocity. Tracer particles were incorporated into the polymer solution and carried by the fluid flow during electrospinning. A camera running at 2000 frames per second was used to trace the movement of the glass beads during the electrospinning.

Figure 4.6 shows an overlap of 12 movie frames during electrospinning. The position of the particle in each frame was marked by circle. The particle speed was calculated by dividing the calibrated distance between circles by the time elapsed between neighbor frames. Fluid velocities as a function of positions along the jet axis were characterized.

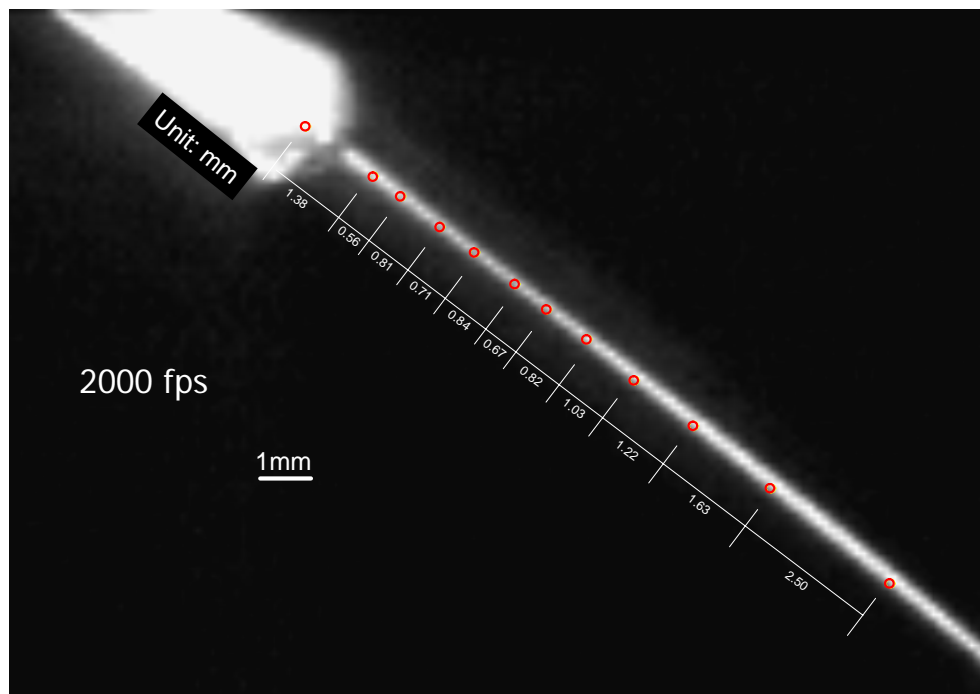


Figure 4.6 Jet speed measurement by particle tracing.

#### 4.2.2.3 Indirect measurement

The velocity of the jet also can be calculated indirectly by volumetric flow rate and the jet diameter ( $d$ ) profile. At the steady state, the volumetric flow rate is  $Q$  and the diameter of the jet is  $d$ , then the velocity  $V$  of the jet can be calculated by Eq.(4.9)

$$V = \frac{4Q}{\pi d^2} \quad (4.9)$$

#### 4.2.3 Measurement of longitudinal stress along jet

In electrospinning jets the longitudinal viscoelastic stresses begin to build up in the orifice, and become large in the transition zone from the Taylor cone to a completely formed jet. This is due to the building up of the surface charge density in the transition from the conductive domain to the convective domain. After the jet becomes convection dominates, the surface charged density begins decreasing as the decreasing jet diameter<sup>5,6,62,82,83,84,85,87,88,94,95,96</sup>. Therefore in a straight electrified jet, the electrical stress exerted by the external electrical field decreases along the jet axis away from the tip which has been concluded from the simulation modeling results. No experiment has ever been done to measure the longitudinal stress along the electrospinning jet so far.

1917 Zeleny<sup>44</sup> measured the electrical intensity by reading the pressure change in the liquid reservoir which was the only attempt to measure the electrical pulling force on the liquid surface. (Figure 4.7)

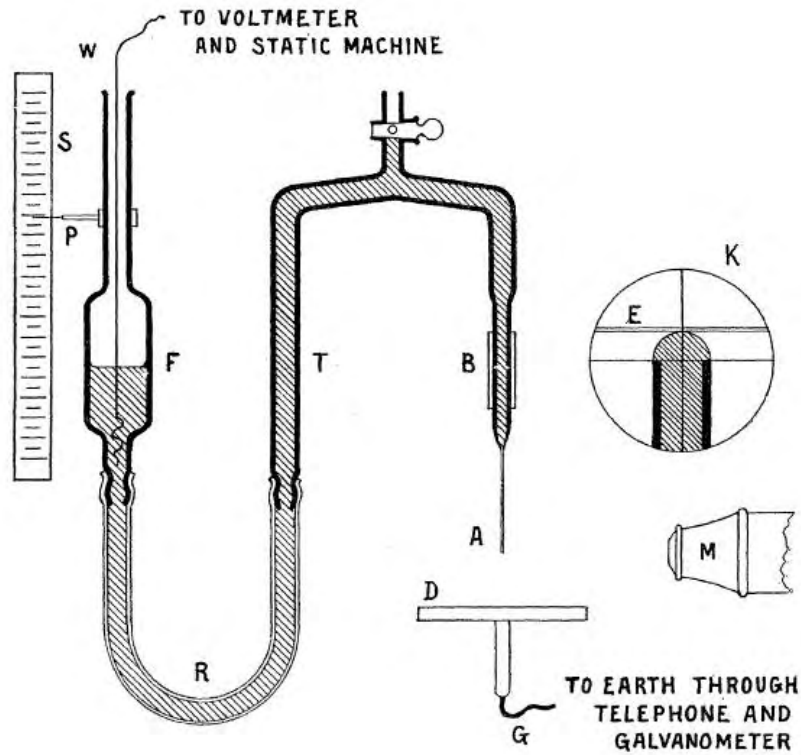


Figure 4.7 Diagram of apparatus used by Zeleny<sup>44</sup>.

For an uncharged viscoelastic liquid jets rapidly propagating in air and experiencing the aerodynamically-driven bending instability, the crucial role of the initial viscoelastic stresses is well understood theoretically<sup>130</sup> and their level was measured in a number of experiments<sup>132, 133, 134, 135</sup>. In particular, the method of periodic transverse vibrations was proposed which allows measurement of the level of the longitudinal stresses in uncharged jets freely moving in air, as well as an estimate of the viscoelastic relaxation time of the liquids in such jets<sup>132, 133, 134, 135, 136</sup>.

In this chapter we introduce a novel measurement method based on the analysis of a single transverse pulse imposed on a jet, and to apply it for measurements of

longitudinal viscoelastic stresses and relaxation time in the electrically-driven jets characteristic of electrospinning.

Stretching of polymer solutions in electrospun jets begins in the transition zone, between the Taylor cone where liquid is practically unloaded, and the beginning of the thin jet, where the liquid can already be significantly pre-stretched<sup>2</sup>. As a result of this pre-stretching, the jet can possess a significant initial stress which might affect its further evolution. The rate of strain in this strong and extremely short pre-stretching process<sup>2</sup> is of the order of 100 sec<sup>-1</sup> to 1000 sec<sup>-1</sup>. Due to the mass conservation in the transition zone (practically no solvent evaporation yet), the elongation of a material element there is:

$$\lambda = \left(\frac{a_b}{a_e}\right)^2 \quad (4.10)$$

$a_b$  is the cross-sectional radii at the beginning of the transition zone

$a_e$  is the cross-sectional radii at the end of the transition zone

It is well-known that polymer solutions react to strong and almost instantaneous stretching almost as an elastic neo-Hookean (rubber-like) body with practically no relaxation involved<sup>130</sup>. The stress  $\sigma_{xxe}$  at the end of the transition zone (the initial stress in the jet) is then given by

$$\sigma_{xxe} = 2G\lambda^2 = 2G\left(\frac{a_b}{a_e}\right)^4 \quad (4.11)$$

$G$  is the modulus of elasticity

$a_b$ ,  $a_e$  are measured from the photograph (Figure 4.8).

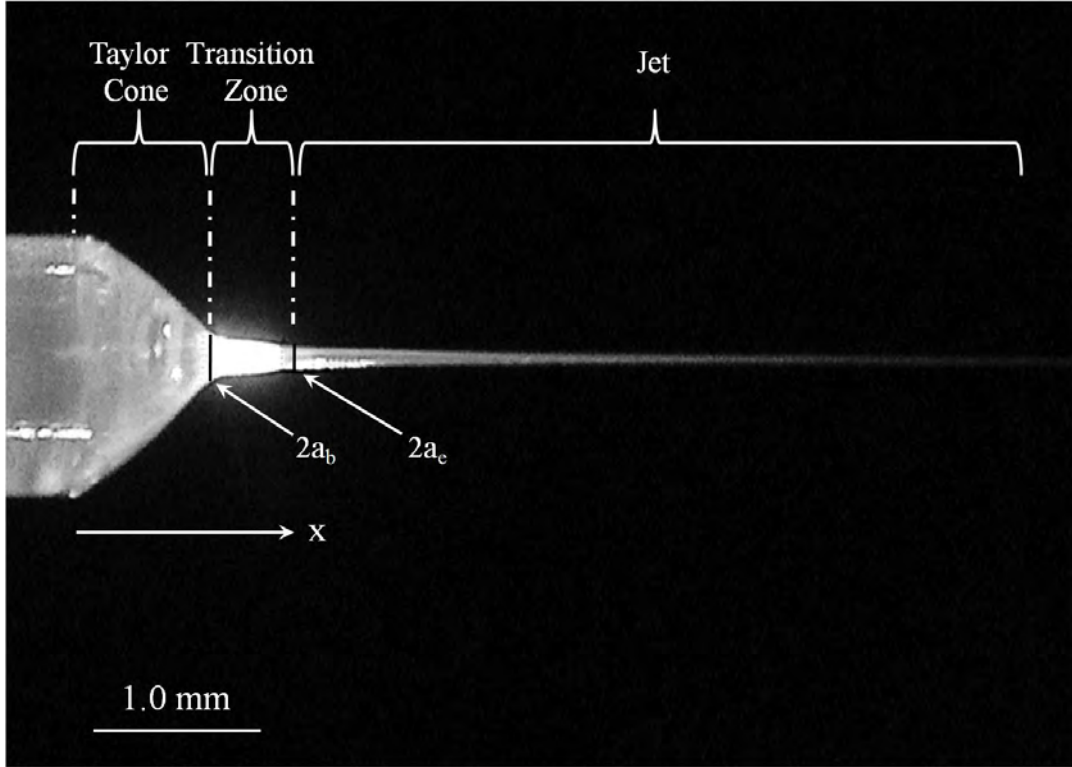


Figure 4.8 Taylor cone with the transition zone in an electrically-driven jet.

Consider now a straight tapering electrified viscoelastic jet moving in air. The electric force acting on the jet section is longitudinal and is established by the high electrical charge density in the jet cross-section and over its surface<sup>5, 6, 131</sup>. The pulse perturbations imposed on the straight electrified jet are assumed to be sufficiently small and planar. Based on the momentless quasi-one-dimensional equations of the dynamics of free liquid jets<sup>130, 138</sup>, the normal projection of the momentum balance equation takes the following form:

$$\frac{\partial^2 H}{\partial t^2} + 2V(x) \frac{\partial^2 H}{\partial t \partial x} + \left[ V(x)^2 - \frac{\sigma_{xx}(x)}{\rho} \right] = 0 \quad (4.12)$$

$t$  is time

$x$  is the longitudinal Cartesian coordinate along the unperturbed jet axis

$H = H(t, x)$  is the normal displacement of the jet axis

$V = V(x)$  is the longitudinal liquid velocity along the jet

$\sigma_{xx} = \sigma_{xx}(x)$  is an unperturbed tensile stress in the jet cross-section

$\rho$  is the liquid density

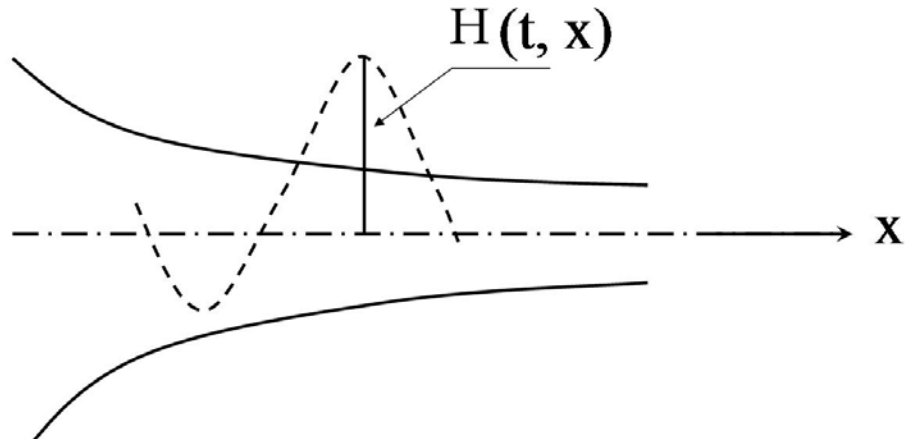


Figure 4.9 Sketch of a tapered straight jet, and lateral (bending) perturbation of its axis.

The hyperbolic Eq. (4.12) describes propagation of sufficiently small bending perturbations along a straight tapering viscoelastic jet. The normal (lateral) velocity of the jet related to bending perturbations is given by  $V_n = \frac{\partial H}{\partial t}$ .

The hyperbolic Eq. (4.12) possesses two characteristics:

$$\xi(t, x) = \int_0^x \frac{dx}{V + \sqrt{\sigma_{xx}/\rho}} - t = C_1 \quad (4.13)$$

$$\eta(t, x) = \int_0^x \frac{dx}{V - \sqrt{\sigma_{xx}/\rho}} - t = C_2 \quad (4.14)$$

where  $C_1$  and  $C_2$  are constants.

The general solution of Eq. (4.12) is given by:

$$H(t, x) = \Phi \left( \int_0^x \frac{dx}{V + \sqrt{\sigma_{xx}/\rho}} - t \right) + F \left( \int_0^x \frac{dx}{V - \sqrt{\sigma_{xx}/\rho}} - t \right) \quad (4.15)$$

where  $\Phi = \Phi(\cdot)$  and  $F = F(\cdot)$  are arbitrary functions.

For any particular perturbation pattern (e.g., time-periodic perturbations or a single pulse) these functions can be always found via the initial conditions:

$$H = H_0(x) \text{ at } t = 0; \quad V_n = \frac{\partial H}{\partial t} = V_{n0}(x) \text{ at } t = 0 \quad (4.16)$$

where the initial wave pattern  $H_0(x)$  and the lateral velocity distribution related to it  $V_{n0}(x)$  can be measured experimentally. The longitudinal velocity distribution in the unperturbed jet is also known in principle as  $V(x) = \frac{Q}{\pi a(x)^2}$  where  $Q$  is the volumetric flow rate and the cross-sectional radius distribution  $a = a(x)$  can be measured experimentally or calculated using the existing theoretical models<sup>5, 6, 130, 131</sup>. The unperturbed tensile stress distribution  $\sigma_{xx}(x)$  along the jet is not immediately measurable, and our aim is to establish it using the above results.

Determination of  $\sigma_{xx}(x)$  does not require knowledge of  $V(x)$  (or  $a(x)$ ) and  $V_{n0}(x)$ . The solution (4.15) represents a superposition of two d'Alembert waves (signals)  $\Phi$  and  $F$ , which propagate with speeds  $V + \sqrt{\sigma_{xx}/\rho}$  and  $V - \sqrt{\sigma_{xx}/\rho}$ , respectively. Any pulse-like perturbation widens by  $2\sqrt{\sigma_{xx}/\rho}\Delta t$  during time  $\Delta t$ , since it

is propagated by the two signals. The widening of the pulse  $W$  between  $t = 0$  and  $t = \Delta t$  can be measured. Then,

$$\sigma_{xx} = \rho \left( \frac{W}{2\Delta t} \right)^2 \quad (4.17)$$

- (i). Repeating the experiment with the pulse being applied at different coordinates  $x$ , one can measure the whole profile of the unperturbed stress  $\sigma_{xx}(x)$  along the jet.
- (ii). If the duration of the pulse observation time  $\Delta t$  is taken much less than the shortest expected relaxation time (say,  $\Delta t$  is taken of the order of 0.5 ms), one can avoid multiple pulse application at different locations  $x$ .

In case (ii) observing a single pulse propagating along the whole jet, we can consider it as different pulses applied at different locations, while the local observation time  $\Delta t$  is taken that short that the elastic relaxation time characteristic of stress  $\sigma_{xx}(x)$  in an observed jet segment will be longer than the observation period from  $t$  to  $t + \Delta t$ . Then, the measured value of  $W$  and thus  $\sigma_{xx}(x)$  could be attributed to the location of the pulse peak between  $t$  and  $t + \Delta t$ . The experimental procedure based on observations of a single pulse (ii) was implemented in the present work.

### 4.3 EXPERIMENTAL

Polyethylene oxide, PEO, ( $M_w = 400,000$  g/mol), purchased from Scientific Polymer Products, Inc., was used as a 6 wt% solution in water. Density of the solution was  $10^3$  kg/m<sup>3</sup>, zero shear viscosity 5 Pa·s, surface tension 61 mN/m, and the electrical conductivity 0.0125 S/m. The experiments were done under ambient conditions at room temperature and relative humidity of about 25%.

A digital video camera attached to an optical microscope was used to record the profile of the transition zone between the Taylor cone and the beginning of the jet (Figure 4.10). The experiment was conducted as follows. Polymer solutions were held in a glass pipette which had tip several centimeters long with an 800  $\mu$ m inner diameter. A copper wire was immersed in the solution and connected with a high voltage power supply which could generate DC voltage up to 13 kV. A grounded horizontal plate was placed below the pipette tip to serve as a collector-electrode. The distance between the pipette tip and the grounded plate could be adjusted from 0.1 cm to 30 cm. An ammeter was connected between the collector plate and ground to measure the current carried by the electrically driven jet.

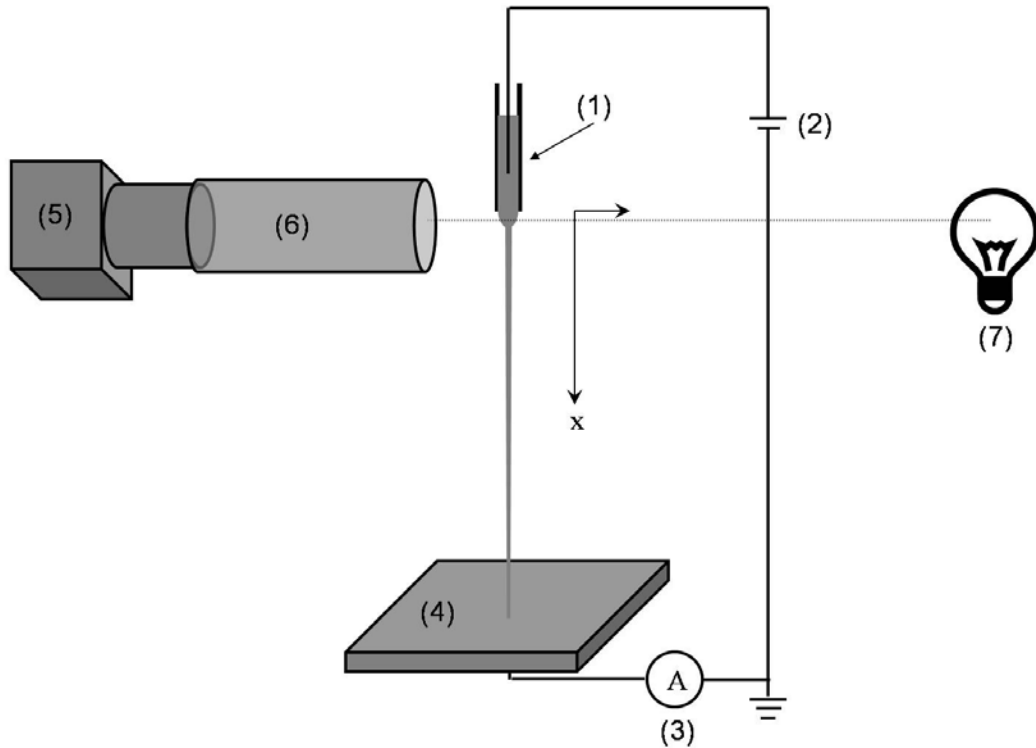
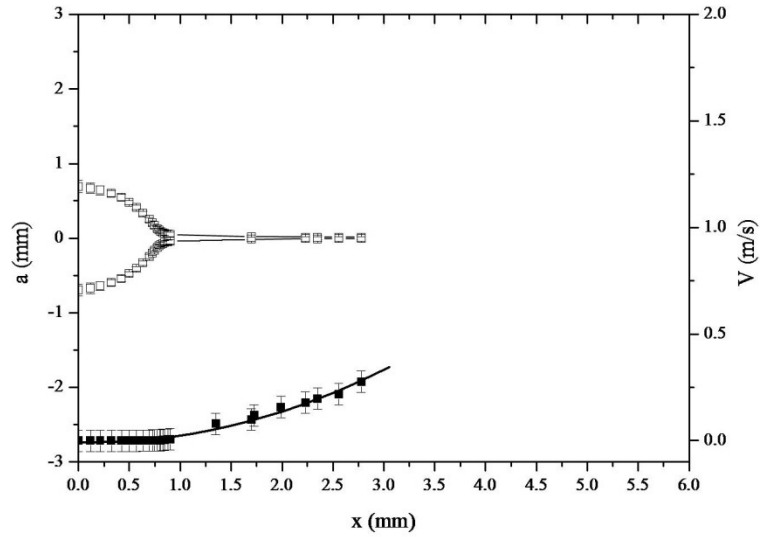
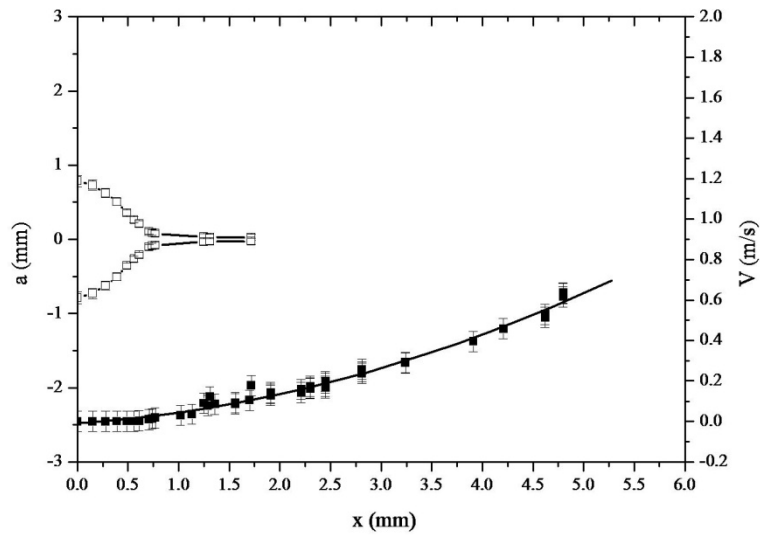


Figure 4.10 Schematic drawing of the experimental setup for measuring radius and velocity distributions and evaluating the stretching rate. (1) Pipette; (2) high voltage DC power supply; (3) ammeter; (4) grounded collector; (5) digital video camera ; (6) optical microscopy; (7) illumination light.

The cross-sectional radius in the transition zone  $a = a(x)$  was measured from the images of the transition zone (Figure 4.11). Then, the longitudinal velocity  $V = V(x)$  was calculated as  $V = \frac{Q}{\pi a^2}$ , where  $Q$  is the volumetric flow rate sustained in the experiment. A Laser Doppler Velocimeter was used to measure the velocity of the jet following the transition zone. The velocity profiles in the transition zone and the jet were combined and matched each other smoothly (Figure 4.11).



(a)

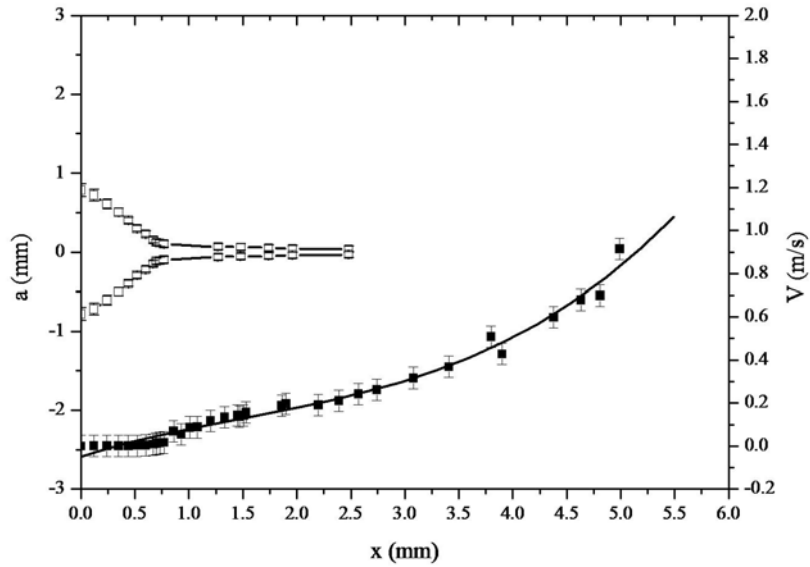


(b)

Figure 4.11 Profile of the transitional zone following the Taylor cone and the beginning of the jet. The cross-sectional radius is shown as  $a = a(x)$  (the symmetric profile in the middle-left), where the axial coordinate  $x$  is rendered from the first observable cross-section of the drop. At the end of the transition zone and the beginning of the jet,  $x = x_e$ . The velocity distribution measured is shown by the solid curve below the profile  $a = a(x)$ . The change in the jet diameter after the transition zone is practically unseen in this scale which is the reason that the velocity distribution in the figure in two cases extends beyond the profile of the transition zone.

(a)  $U = 3$  kV

(b)  $U = 4$  kV



(c)

Figure 4.11 Profile of the transitional zone following the Taylor cone and the beginning of the jet. The cross-sectional radius is shown as  $a = a(x)$  (the symmetric profile in the middle-left), where the axial coordinate  $x$  is rendered from the first observable cross-section of the drop. At the end of the transition zone and the beginning of the jet,  $x = x_e$ . The velocity distribution measured is shown by the solid curve below the profile  $a = a(x)$ . The change in the jet diameter after the transition zone is practically unseen in this scale which is the reason that the velocity distribution in the figure in two cases extends beyond the profile of the transition zone. (continued)

(c)  $U = 5$  kV.

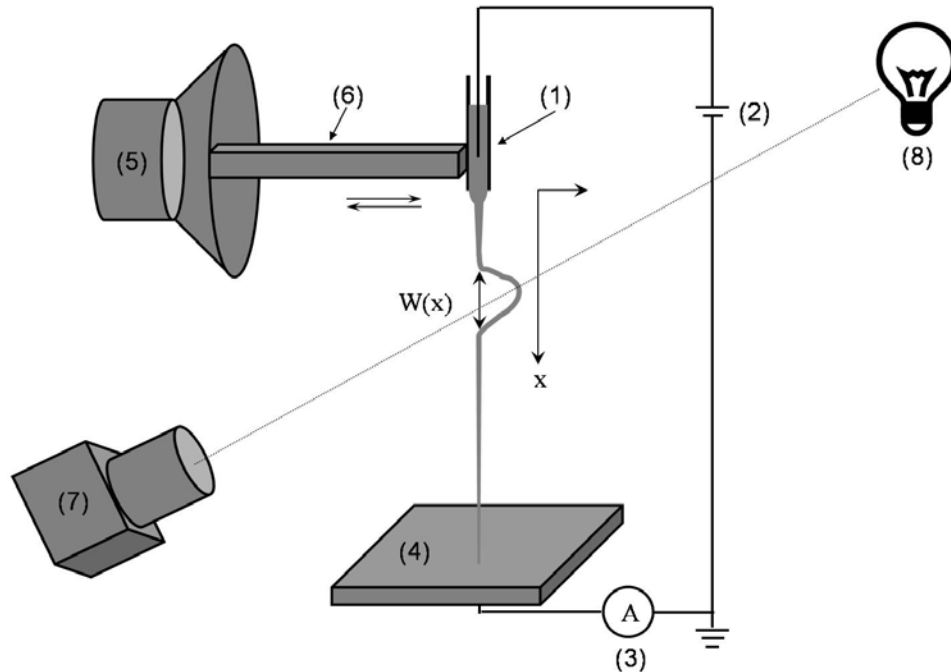
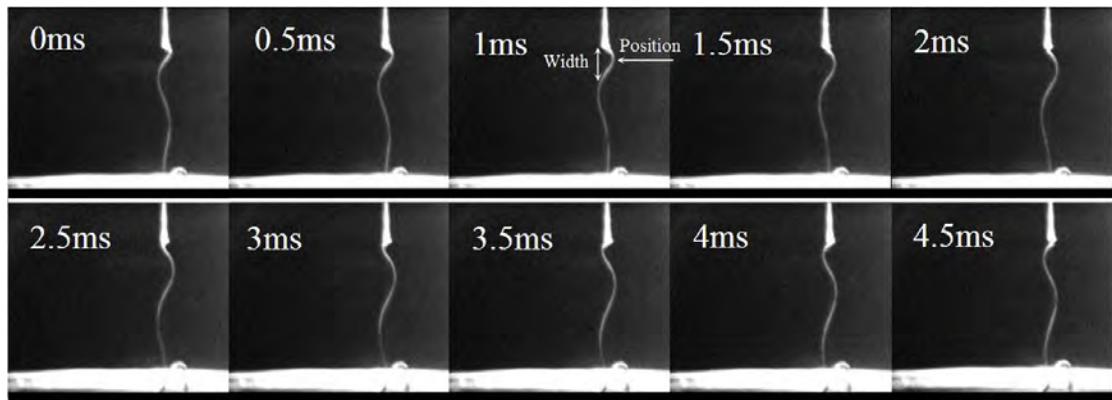


Figure 4.12 Schematic drawing of the experimental setup for measuring longitudinal stresses in jets. (1) Pipette; (2) high voltage DC power supply; (3) ammeter; (4) grounded collector; (5) loudspeaker; (6) polystyrene bar; (7) high speed camera; (8) illumination light.

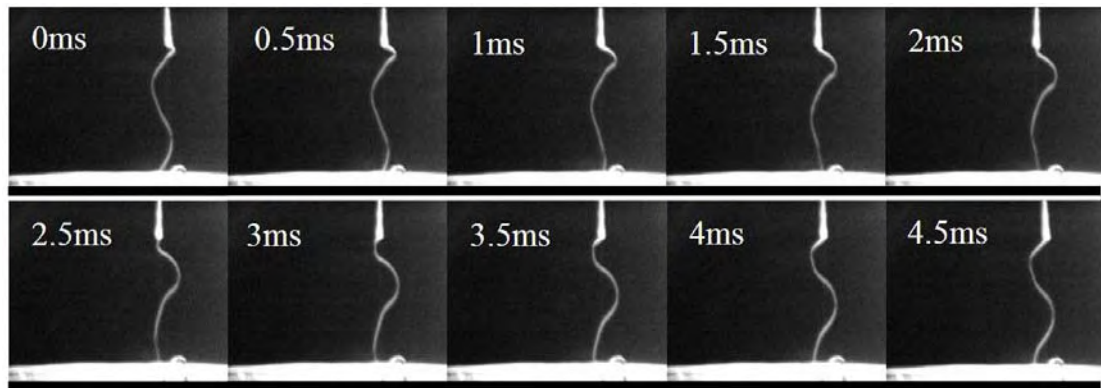
The single-pulse experiment was conducted as follows. A polystyrene bar with a high stiffness and low density was glued onto a loudspeaker which produced a single displacement pulse when a suitable electrical pulse was applied. The polystyrene bar was positioned as shown in Figure 4.12, so that the displacement pulse from the loudspeaker imparted a pulse-like lateral motion to the tip of the pipette. The amplitude of the lateral motion of the jet was about 2 mm. The time from the beginning to the end of the pulse was about 4 ms to 5 ms. As a result of the tip motion, a lateral displacement was imposed on the jet.

#### 4.4 Results and discussion

The stretching rate in the transition zone is equal to  $dV/dx$ . Its values were found using the data depicted in Figure 4.11 and were in the range  $100 \text{ sec}^{-1}$  to  $1000 \text{ sec}^{-1}$ . This is a tremendously high rate of strain for 6% polymer solutions which could be hardly achieved in any other experiment.



(a)



(b)

Figure 4.13 Propagation and widening of a single lateral displacement pulse. The inter-electrode distance  $L=5.5 \text{ cm}$ .

(a)  $U= 3 \text{ kV}$ ,  $I= 100 \text{ nA}$ .

(b)  $U= 4 \text{ kV}$ ,  $I= 390 \text{ nA}$ .

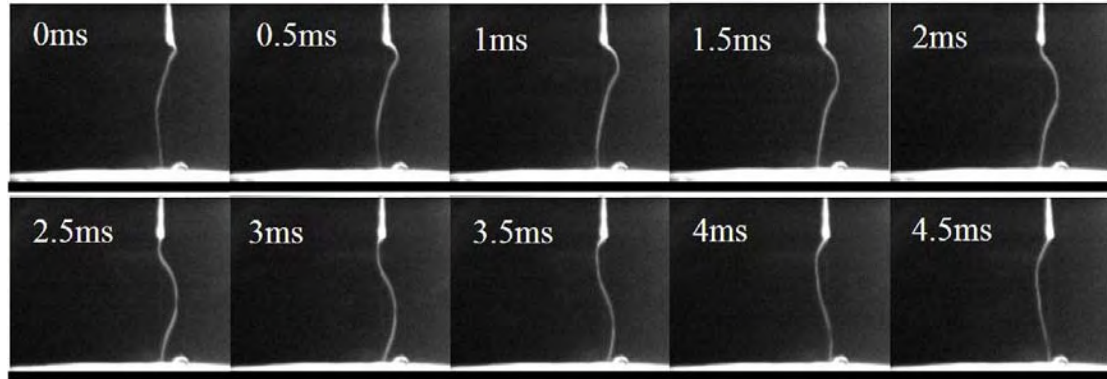


Figure 4.13 Propagation and widening of a single lateral displacement pulse. The inter-electrode distance  $L= 5.5$  cm. (continued)  
(c)  $U= 5$  kV,  $I= 880$  nA.

The pulse propagation and widening images are presented in Figure 4.13 for the applied voltage pulling the jet to the grounded electrode in the range from 3 kV to 5 kV. The images in Figure 4.13 were measured to determine the location of the pulse peak,  $P$ , and the width,  $w$ , versus time. Peaks observations and measurements were done at sufficiently short time intervals. The observations of a single peak propagating over the jet were used to acquire information for the entire length of the jet. An example of such processing is shown in Figure 4.14. Data for  $w(t)$  was approximated by a smooth function shown in Figure 4.14 as a solid line. It was possible to differentiate  $w(t)$  and find the derivative  $\partial w/\partial t$  corresponding to any instantaneous location of the lateral displacement pulse propagating over the whole jet. The data in Figure 4.14 was used to calculate the widening rate of the pulse at different locations along the jet. It was possible to calculate the pulse widening over time intervals much shorter than any expected relaxation time value. Using  $W/\Delta t = \partial w/\partial t$ , the stress  $\sigma_{xx}$  in the unperturbed jet was calculated via Eq. (4.17).

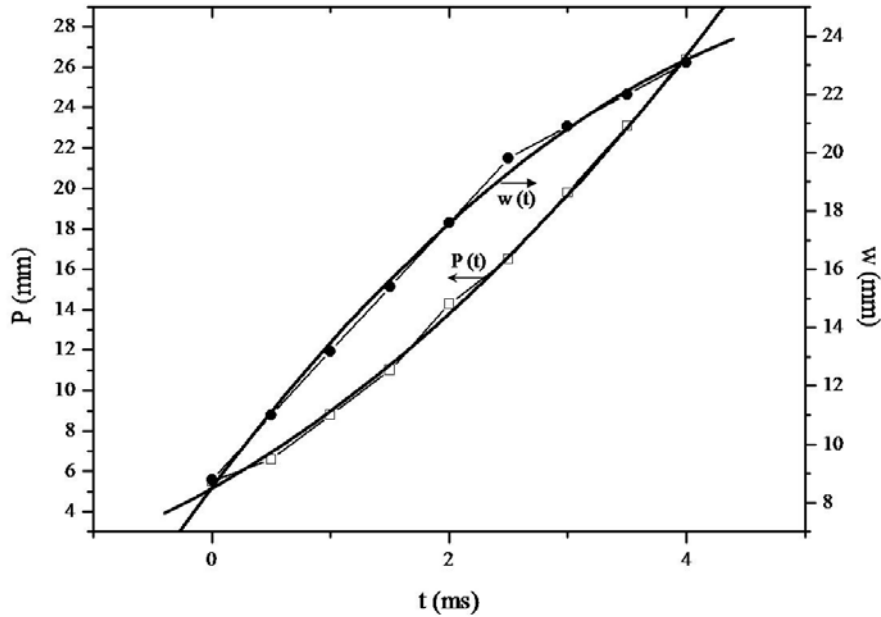
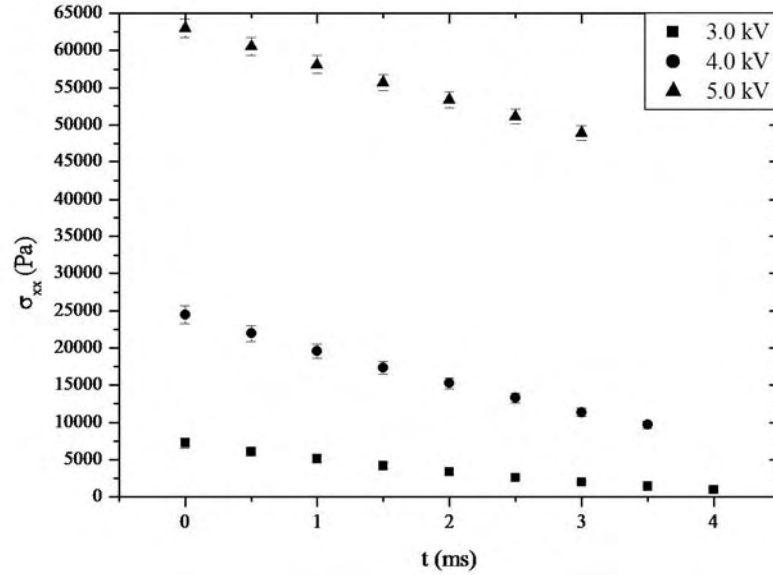
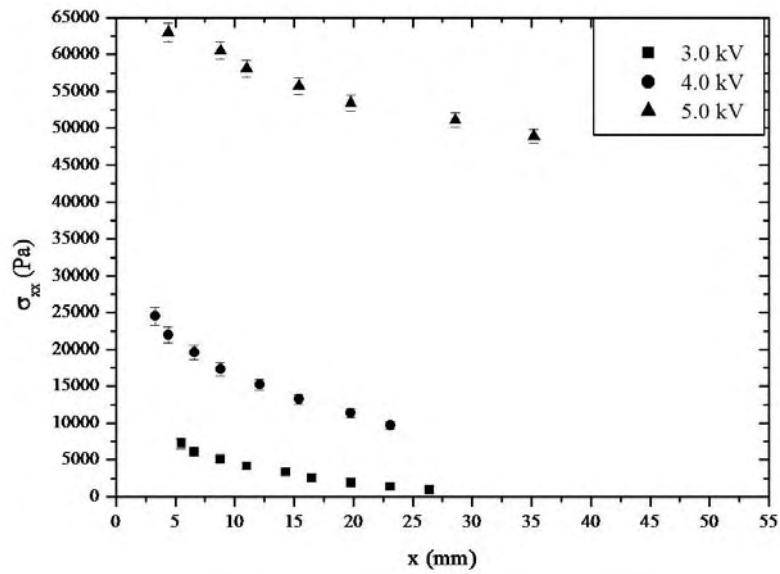


Figure 4.14 Pulse peak location  $P$  and width  $w$  versus time. The broken lines connect the data points shown by symbols, the smoothed lines show the best fit of the data. The width-time curve is used to evaluate  $\frac{\partial w}{\partial t} = W/\Delta t$  needed to calculate the longitudinal stress  $\sigma_{xx}$  in the unperturbed jet using Eq. (4.17). The voltage applied to issue the jet was 3 kV in this case

The value of  $\sigma_{xx}$  thus found can be associated with the value of  $t$  used to calculate the derivative  $\frac{\partial w}{\partial t} = W/\Delta t$  or the corresponding peak location  $P = P(t) = x$ . Thus,  $\sigma_{xx} = \sigma_{xx}(t)$  can be recast into  $\sigma_{xx} = \sigma_{xx}(x)$ . These distributions are presented in Figure 4.15.



(a)



(b)

Figure 4.15 Longitudinal stress distribution over the straight unperturbed electrified jet for different applied voltages. The inter-electrode distance was held at 5.5 cm.

(a) Stress versus pulse-related time  $t$ ,  $\sigma_{xx} = \sigma_{xx}(t)$ . Symbols show the experimental data for different applied voltages.

(b) The Eulerian presentation as  $\sigma_{xx} = \sigma_{xx}(x)$ . Symbols show the experimental data for different applied voltages.

For a material element of the jet to reach a location  $x$ , it takes a different time  $t_m$  than for a pulse  $t$  (the latter moves over the liquid jet). For a material element it takes time  $t_m$  to reach  $x$ . Then, the stress distribution  $\sigma_{xx}(x)$  (in the Eulerian sense) can be recast into  $\sigma_{xx}(t_m)$ , as shown in Figure 4.16.

$$t_m = \int_0^x \frac{dx}{v(x)} \quad (4.18)$$

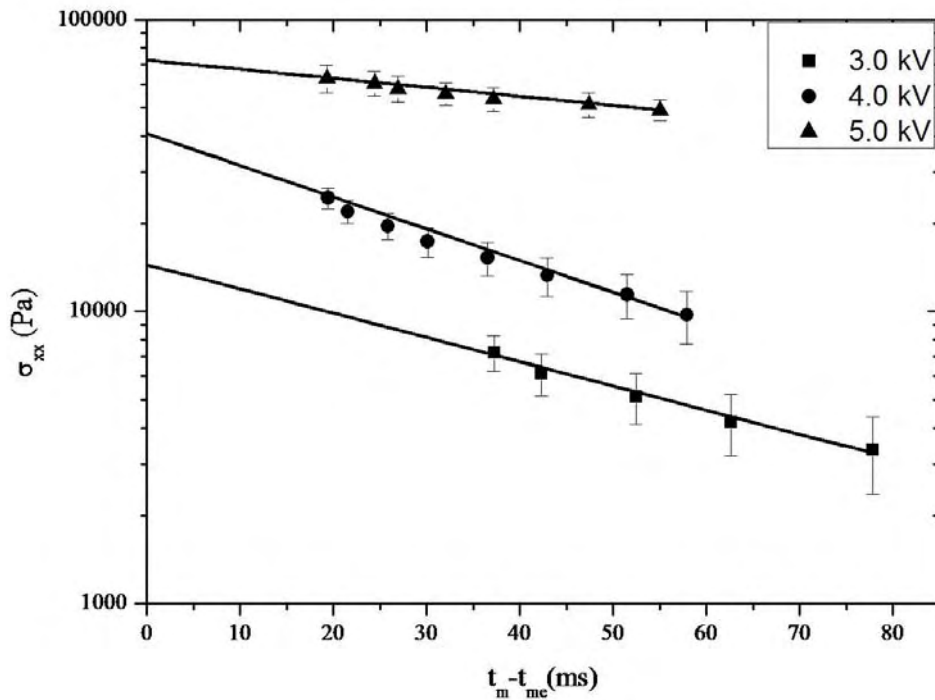


Figure 4.16 The Lagrangian presentation  $\sigma_{xx} = \sigma_{xx}(t_m - t_{me})$ . The time moments when the material element exits the transition zone and reaches the beginning of the jet is denoted by  $t_{me}$ . The values of  $t_{me}$  were 15145 ms, 1880 ms and 1183 ms for the voltages of 3 kV, 4 kV and 5 kV, respectively. The distributions of stress  $\sigma_{xx}$  versus  $t_m - t_{me}$  are plotted in semi-logarithmic scale. Symbols show the experimental data for different applied voltages; lines are plotted using Eq.(4.19) and Eq.(4.20).

The initial stresses at the beginning of the jets generated because of the pre-stretching in the transition zone at the end of the Taylor cone appeared to be of the order of 10 kPa to 100 kPa (Figure 4.15 and Figure 4.16). The latter value is larger than those reported for the uncharged jets<sup>133, 134,135</sup> by two orders of magnitude. This reveals the strong electrical forces affecting polymer solutions in the transition zone prior they form a jet. The higher the applied voltage is (at a fixed inter-electrode distance), the higher is the value of the initial longitudinal stress generated in the jets. Figure 4.15 and Figure 4.16 show that relaxation effects in the straight part of the electrospinning jets dominate the stretching effect of the electric stresses acting on them (which means that the flow is weak there, following the terminology used in polymer physics). Therefore, the longitudinal stresses relax along the jet. This result, in fact, invalidates all the theoretical models of the straight part of the viscoelastic electrospinning jets published so far, since they disregard the existence of these high initial longitudinal stresses generated in the transition zone between the Taylor cone and the beginning of the jet. Moreover, the results in Ref. 130 (Figure 3.25 , pp. 141) showed that growth of bending perturbations is delayed by initial high longitudinal stresses in the pre-stretched jets. Even though this result was found in Ref. 130 for the aerodynamically-driven bending instability, it can be immediately recast for the electrically-driven bending instability, since the equivalence of the two phenomena was established<sup>6</sup>. This equivalence allows the following interpretation of the results presented in Figure 4.15 and Figure 4.16: the electrically-driven bending instability is impossible from the tip of the Taylor cone up to the distance of about 2cm to 4 cm from it, because there the stabilizing longitudinal

stresses are sufficiently high. This indeed happens in reality<sup>5, 6,131</sup>. Moreover, the results depicted in Figure 4.15 and Figure 4.16 suggest that the straight section of an electrospinning jet should be longer if the jet is formed at a higher applied voltage. Again, the predicted increase in the length of the straight segment of the jet with an increase in the applied voltage is seen in experiments<sup>5, 6,131</sup>.

The initial longitudinal stress  $\sigma_{xxe}$  should be attributed to  $t_m - t_{me} = 0$  in each experiment depicted in Figure 4.16. The values of  $t_{me}$  for these experiments are listed in the caption to Figure 4.16. It is emphasized that these values incorporate all the prehistory of the fluid particles when they moved from the very bottom of the Taylor cone where the flow is extremely slow and the residence time is large. That is the reason that the values of  $t_{me}$  (and  $t_m$ ) are of the order of  $10^3$  ms to  $10^4$  ms. Then, fitting of Eq. (4.11) (with  $a_b$  and  $a_e$  being measured from the images similar to that in Figure 4.8) reveals the corresponding values of the modulus of elasticity  $G$ . It was found that  $G = 53.26$  Pa, 163.3 Pa and 395.4 Pa for the applied voltages  $U = 3.0$  kV, 4.0 kV and 5.0 kV, respectively. Stress relaxation in a material liquid element moving along the jet seen in Figure 4.19 can be interpreted using the expression derived via the integration of the equations of the Upper-Convected Maxwell model (UCM) with a single relaxation time

$$\sigma_{xx} = \sigma_{xxe} \exp \left[ \frac{-(t_m - t_{me})}{\theta_{eff}} \right] \quad (4.19)$$

$$\theta = \frac{\theta_{eff}}{1 + 2 \left( \frac{dV}{dx} \right)_{max} \theta_{eff}} \quad (4.20)$$

where  $\theta_{eff}$  is the effective relaxation time

$\theta$  is the real relaxation time corresponding to contraction of macromolecules to their equilibrium length (the Rouse relaxation process)<sup>4,21</sup>

$\left(\frac{dV}{dx}\right)_{max}$  is taken as the largest (positive) value of the stretching rate.

Fitting Eq.(4.19) and Eq.(4.20). to the experimental data in Figure 4.16, one can find  $\sigma_{xxe}$  and  $\theta$  (shown in Table 4.1). Therefore, both characteristic rheological parameters of polymer solutions  $G$  and  $\theta$  can be established in one experiment. The initial elongational viscosity in the jet is then estimated as  $\mu = \sigma_{xxe}\theta$  (Table 4.1).

Eq. (4.19) and Eq. (4.20) follow from the integration of the following rheological constitutive equations of the UCM model

$$\frac{d\tau_{xx}}{dt_m} = \left(2 \frac{dV}{dx} - \frac{1}{\theta}\right) \tau_{xx} + 2 \frac{\mu}{\theta} \frac{dV}{dx} \quad (4.21)$$

$$\frac{d\tau_{yy}}{dt_m} = -\left(\frac{dV}{dx} + \frac{1}{\theta}\right) \tau_{yy} - \frac{\mu}{\theta} \frac{dV}{dx} \quad (4.22)$$

valid for uniaxial elongation in a jet, where  $\tau_{xx}$  and  $\tau_{yy}$  are the longitudinal and lateral deviatoric stresses in the jet, while the longitudinal stress  $\sigma_{xx} = \tau_{xx} - \tau_{yy}$ . The initial conditions are:  $t = t_{me}$ ,  $\tau_{xx} = \tau_{xxe}$ ,  $\tau_{yy} = \tau_{yye}$  (and thus  $\sigma_{xx} = \sigma_{xxe} = \tau_{xxe} - \tau_{yye}$ ).

The integration leading to Eq. (4.19) and Eq. (4.20) is done for  $\frac{dV}{dx} = \left(\frac{dV}{dx}\right)_{max} = const.$

The result shows (as expected in jets) that  $\tau_{xx} \gg \tau_{yy}$ , and thus  $\sigma_{xx} \approx \tau_{xx} \approx$

$$\sigma_{xxe} \exp \left\{ -(t_m - t_{me}) \left[ \frac{1}{\theta} - 2 \left( \frac{dV}{dx} \right)_{max} \right] \right\}$$

The fact that the experimental data show that the stress  $\sigma_{xx}$  decreases when a material element moves along the jet, means that in the present case the viscoelastic relaxation reduces the tensile stress faster than the elongation due to the electric field increases the stress, and thus  $\frac{1}{\theta} > 2 \left( \frac{dV}{dx} \right)_{max}$ . In this sense, the flow in the straight part of the jet is weak, whereas the flow in the preceding transition zone is strong (since it results in a build-up of the longitudinal stress). It is emphasized that Eq. (4.19) and Eq. (4.20) account for the jet stretching by the electric field which determines the value of  $\left( \frac{dV}{dx} \right)_{max}$ . In a more detailed analysis, the integration of Eq. (4.21) and Eq. (4.22) could be conducted with accounting for the fact that  $\frac{dV}{dx}$  could vary along the jet. The latter is described in the framework of a conjugate problem incorporating the quasi-one-dimensional equations of the mass and momentum balance for jets, the rheological constitutive equations Eq. (4.21) and Eq. (4.22) and the electric field description accounting for the interaction of the surface charges on the jet with the imposed electric field. In the present work we avoid dealing with the conjugate problem and detailed calculation of the electric field about the jet, because we use the experimental data for  $V(x)$  to evaluate  $\frac{dV}{dx}$ . Since the experimental data obviously reflect the effects of the electric field via  $V(x)$ , the parameter values obtained and presented in Table 4.1 are affected by the electric field properly.

Electrospinning jets consist of four distinct zones: Taylor cone (a very weak, almost Newtonian flow), transition zone (a strong elongational flow at rates of 100 to 1000 sec<sup>-1</sup>), straight part (a weak elongational flow<sup>5</sup> at a strain rate averaged above the entire length of the straight segment that is of the order of 20 sec<sup>-1</sup>), and bending loops (with an initial strong elongational flow with strain rates of the order of 1000 sec<sup>-1</sup> which decreases rapidly with length<sup>5</sup>).

Stretching in the transition zone is strong (at the rates of 100 sec<sup>-1</sup> to 1000 sec<sup>-1</sup>). Therefore, the method outlined here can be used for the elongational rheometry of concentrated polymer solutions and melts under an extremely strong elongation. We are unaware of any other method which could be used for elongational measurements of concentrated polymer systems with such high rates of strain

Table 4.1 Characteristics of the Polyethylene oxide solution calculated from Eq. (4.19) and Eq. (4.20).

$U(kV)$	$\sigma_{xxe}(Pa)$	$G(Pa)$	$\theta(ms)$	$\mu(Pa \cdot s)$
3.0	14431.0	53.26	8.27	119.3
4.0	26455.8	163.3	3.04	80.4
5.0	64050.3	395.4	2.97	190.2

#### 4.5 SUMMARY

A novel method of measurement of viscoelastic longitudinal stresses in straight electrically driven jets of polymer solutions was proposed and applied to the cases characteristic of electrospinning. The method was based on the observation of propagation of a single lateral pulse imposed on the jet and of the profile of the

unperturbed jet. The results revealed that the initial longitudinal stress created by the electric stretching of the jet as it transforms from the Taylor cone is of the order of 10 kPa to 100 kPa. These values are one or two orders of magnitude larger than those values for uncharged, viscoelastic jets. This showed that stretching of polymer solutions in the transition zone of the electrically-driven jets following the Taylor cone is very strong (the rates of stretching are of in the range of  $100 \text{ sec}^{-1}$  to  $1000 \text{ sec}^{-1}$ ). This elucidated the real physical phenomena responsible for the formation of the straight part of the electrospinning jets. The liquid stretching by the electrical field in the straight part of the jet weakened, as the jet elongated, to the level of  $20 \text{ sec}^{-1}$  to  $100 \text{ sec}^{-1}$  according to Refs. 5 and 131, and the initial longitudinal stresses relaxed at a distance of about 2 cm to 4 cm from the transition zone at the end of the Taylor cone. These observations of the transition zone from a Taylor cone to a thin jet revealed why the straight section of an electrospinning jet is longer at a higher voltage. This is because higher initial stress is generated in the transition zone at a higher applied voltage so the straight jet is stabilized for a longer distance. After that, the electrically driven bending instability<sup>5</sup>, characteristic of electrospinning, begins and dramatic elongation, somewhat similar to the elongation following the Taylor cone, occurs at rates of about  $1000 \text{ sec}^{-1}$ . The results also pointed to an opportunity to build an elongational rheometer for semi-dilute and concentrated polymer solutions and melts for stretching rates of the order of  $100 \text{ sec}^{-1}$  to  $1000 \text{ sec}^{-1}$ .

## CHAPTER V

### BUCKLING INSTABILITY OF ELECTROSPINNING JETS

#### 5.1 INTRODUCTION

Buckling of highly viscous Newtonian liquid jets was studied experimentally in the seminal work of Taylor<sup>140</sup>. He assumed that buckling of a liquid jet results from the compressive force imposed by an obstacle the jet impinges upon or a distributed compressive force imposed by an environment. In this sense buckling of liquid jets is kindred to the classical buckling of compressed elastic bars and columns discovered by Euler<sup>141</sup>. Further experiments on buckling of highly viscous liquid jets were published by Cruickshank et al.<sup>142, 143</sup>. The explanation that buckling of liquid jets and films is caused by longitudinal compressive forces was fully confirmed in the framework of the detailed theoretical analysis based on the quasi-one-dimensional equations of dynamics of liquid jets<sup>130, 144, 145</sup>. In all the above-mentioned works jet buckling occurred when a jet impinged on motionless surfaces or liquid-liquid interfaces. Recently jet buckling on laterally moving solid surfaces nearly perpendicular to the jet axis was reported by Chiu-Webster et al.<sup>146</sup>. The stability analysis in that case was also based on the quasi-one-dimensional equations of dynamics of liquid jets similar to the results by Yarin et al.<sup>130, 144, 145</sup> and revealed that characteristic frequencies of buckling are practically unaffected

by the lateral motion of the surface and stay the same as in the case of collection of a liquid jet on stationary hard flat surface<sup>147</sup>.

In the papers cited above the liquid jets were not electrified and patterns evolved only under the action of forces of mechanical origin. In electrospinning, jets of viscoelastic polymer solutions evolve primarily under the action of the electric forces. In particular, electrified jets experience the bending instability that is driven by the mutual repulsion of the excess electric charges carried by electrospinning jets<sup>5, 6, 131</sup>, as well as a secondary branching also rooted in charge repulsion<sup>81</sup>. The present work reports the observation of the deposited fibers resulting from the electrospinning jets that were coiled by the electrical bending instability, as well from the straight segment of electrically-driven jets which impinged onto a collector surface before electrical bending occurred<sup>3, 4</sup>. The effects of the laterally moving collector surfaces were observed. Buckling may or may not accompany bending instability of electrospinning jets, but in fact, represents a totally different and distinguishable phenomenon that occurred very close to the collector.

## 5.2 EXPERIMENTAL

Polyethylene oxide (PEO),  $M_w = 400,000$  g/mol, 6 wt% solution in deionized water; Poly (-L-lactide) (PLLA),  $M_w = 152,000$  g/mol, 5 wt% solution in hexafluoroisopropanol (HFIP); Polystyrene (PS),  $M_w = 350,000$  g/mol, 25 wt% in

Dimethylformamide (DMF); nylon-6, 25 wt% solution in formic acid (FA, 88%); nylon-6, 10 wt% solution in HFIP/FA mixture with the HFIP/FA ratio being 8/2 (by weight). Nylon-6, Poly (-L-lactide) and all solvents were purchased from Sigma-Aldrich Co. Polystyrene and polyethylene oxide were purchased from Scientific Polymer Products, Inc. and used as received.

The experimental setup for electrospinning was similar to those used previously in Chapter III. The ground collector might be tilted at different angles from  $\theta = 0$  to  $45^\circ$  (Figure 5.1). The collector might be either motionless or move horizontally at a constant speed of typically  $V_c = 0$  to 3 m/s. In some experiments a grounded liquid surface was used as collector. When the lateral moving inclined collector was used, the lateral motion of the collector was in the direction that caused the separation between the tip and the collector to increase.

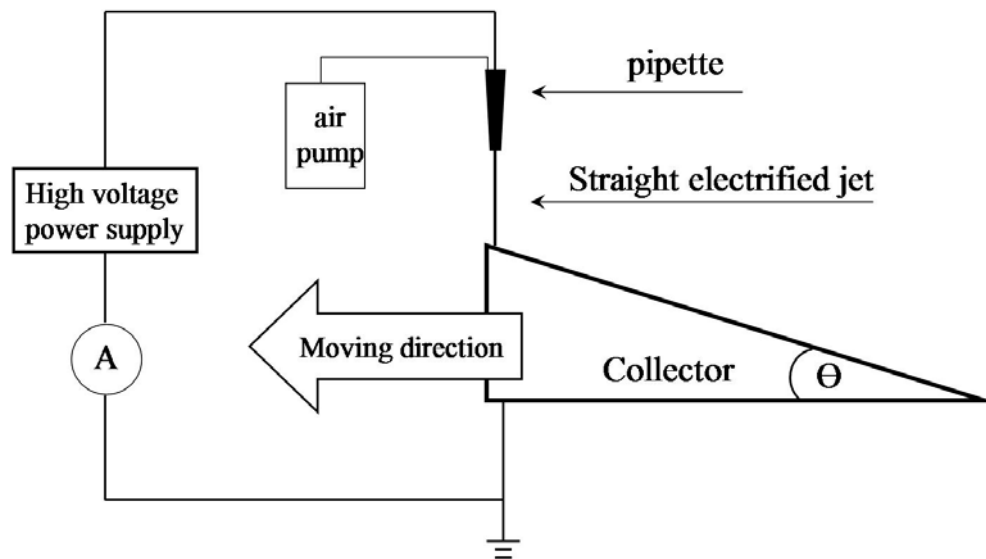


Figure 5.1 Sketch of the experimental setup.

The experiments were conducted under ambient conditions at room temperature and relative humidity of about 25 %. Polymer solutions were held in a glass pipette which had a 2 cm long capillary at one end. The inner diameter of the capillary was 160  $\mu\text{m}$ . A copper wire was immersed in the solution and connected with a high voltage power supply which could generate DC voltage up to 13 kV. The flow was controlled by the outward electric pressure and the air pressure or partial vacuum applied to the surface of the liquid in the pipette. The distance between the capillary and the collector along the straight vertical line could be adjusted from 0.1 cm to 100 cm. An ammeter was connected between the wedge-like collector and electrically grounded wire to measure the current carried by the straight or electrospinning jets.

Collected solidified electrospun fibers were observed with optical microscopy (Olympus 51BX) and Scanning Electron Microscopy (JEOL 5310).

### 5.3 RESULTS AND DISCUSSIONS

Figure 5.2 and Figure 5.3 depict the images of two electrically-driven jets sufficiently above the collecting surface. In the case of a short (for a particular polymer solution) nozzle-collector distance the jet is typically straight (Figure 5.2), whereas at a longer distance (for the same solution) the jet length was sufficiently long for the electrical bending instability to occur (Figure 5.3).

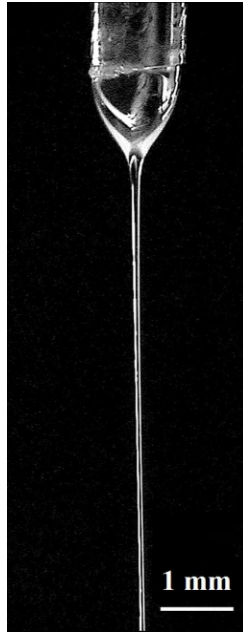


Figure 5.2. Straight electrified jet.



Figure 5.3. Electrospinning jet with electrical bending instability

### 5.3.1 Buckling of straight electrified jets: PEO solution collected on a horizontal moving grounded plate

The PEO solution, held in the pipette, was connected to high voltage power supply. The distance from the capillary orifice to the horizontal grounded collector was 1 cm. The horizontal collector was moved sideways at  $V_c = 0.785$  m/s. The voltage was 2 kV. Under these conditions, the electrical bending instability did not occur and only a straight electrified jet was observed. In this case the relative velocity between the jet and collector  $V_r$  was equal to  $V_c$ , since straight jets did not move sideways prior to buckling. The buckled patterns collected were observed using scanning electron microscopy. Figure 5.4 shows the collected buckled PEO fibers. Sinuous folding, zigzag folding and helical coiling occurred. The rate at which the periodic patterns were created was determined from the known velocity of the substrate. The product of the frequency of the buckling instability and the distance advanced by each cycle ( $\lambda$ , wave length of the deposited buckling pattern) is equal to the relative velocity between the oncoming jet and moving collector. The wave lengths ( $\lambda$ ) of the buckled patterns were around 5  $\mu\text{m}$ . The corresponding frequencies ( $\omega = V_r/\lambda$ ) were around  $3.42 \times 10^5$  Hz. The morphologies of the buckled patterns found in the case of a straight electrified jet resemble those found for buckling of uncharged rectilinear jets impinging on moving plates<sup>146,147</sup>.

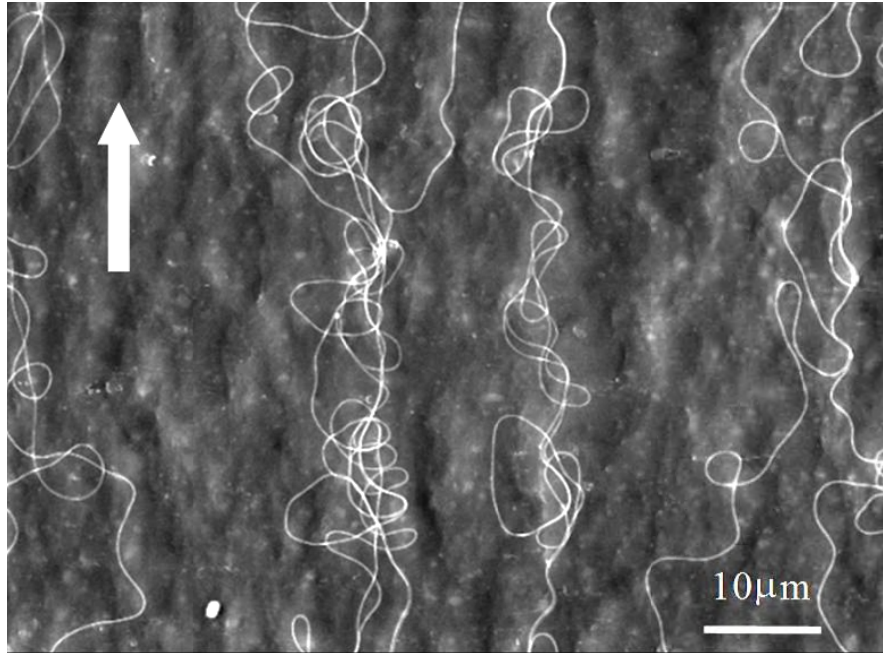


Figure 5.4 SEM image of some of the buckled PEO patterns collected on the horizontal collector which was moving at 0.785 m/s along the direction showed by the white arrow.

### 5.3.2 Buckling of bending electrospinning jets: PEO solution collected on a horizontal moving grounded plate

The deposits resulting from the bending and buckling electrospinning jets are shown in Figure 5.5. It is emphasized that they clearly demonstrate the difference between the effects of bending and buckling. The patterns associated with bending are the large loops corresponding to frequencies of the order of  $10^3$  Hz<sup>10</sup>. The buckling-related patterns appear as tiny wiggles that occurred at frequencies of the order of  $10^5$  to  $10^6$  Hz.

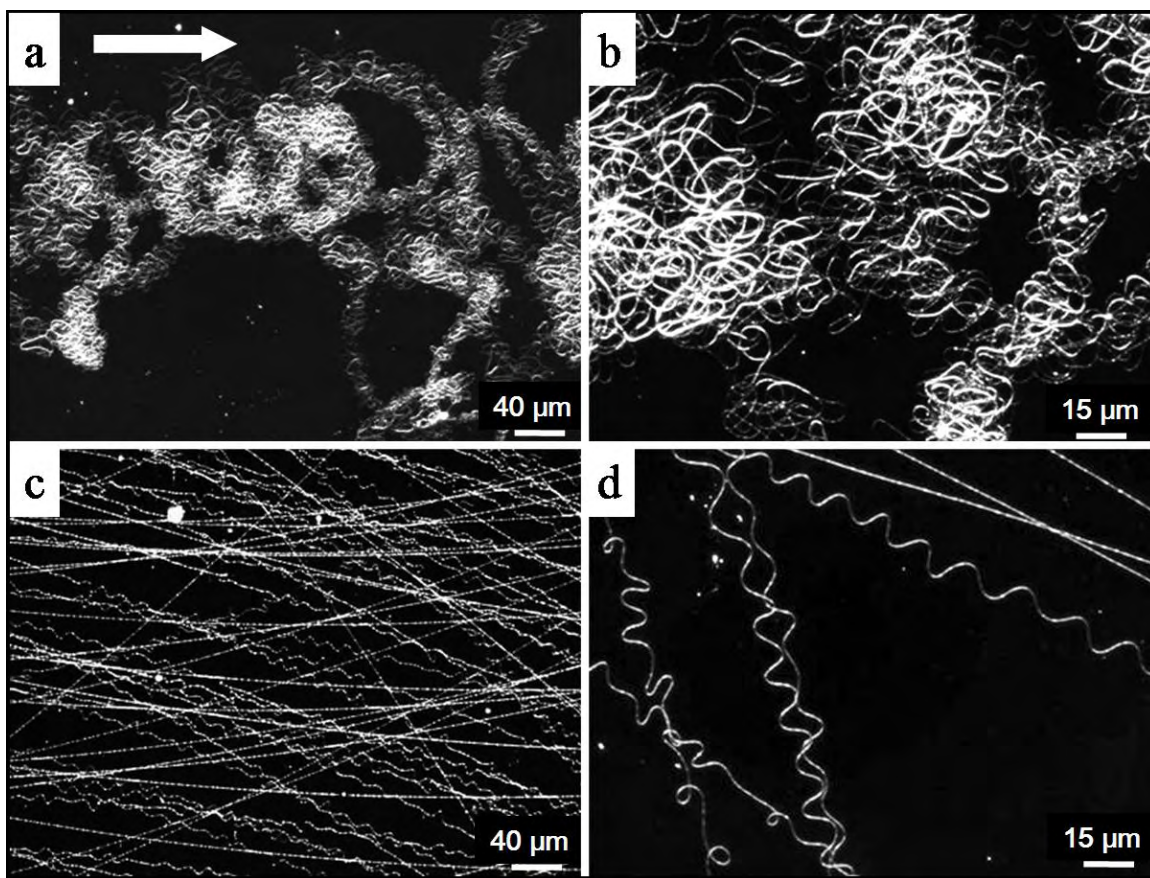


Figure 5.5 Optical micrographs of buckled bending electrospun PEO jets.

The horizontal grounded collector was moving laterally at 0.01 m/s along the direction of white arrow in Figure 5.5-a. The distance from the tip to collector was 1.5 cm (Figure 5.5-a, b) and 5 cm (Figure 5.5-c, d), respectively. At these conditions, electrical bending of the jets occurred prior to impingement onto the collector surface. The diameters of the bending loops at 1.5 cm inter-electrode distances ranged from 100  $\mu\text{m}$  to several millimeters. The diameters of the bending loops at 5 cm inter-electrode distances were several centimeters. Figure 5.5-a, b, c, d also show that the bending loops buckled when they impinged onto the collector surface. The buckling patterns were densely piled along the path of the bending loops. The wavelengths of the buckling

patterns were around 15  $\mu\text{m}$ . Here, as before, we define the wavelength as the distance between adjacent identical segments of the repeating patterns. Figure 5.5-a and Figure 5.5-b show the wavelengths of the buckling patterns were several  $\mu\text{m}$ . The buckling patterns, figure-eights and small circles, were densely piled along the bending loops. Figure 5.5-c and Figure 5.5-d show that the wavelength of the buckling patterns in the wiggles were around 15  $\mu\text{m}$ . The buckling patterns were loosely distributed along the bending loops, producing again sinuous wave, figure-of-eight and small circles. Some of the segments of bending circles in Figure 5.5-d were not buckled, probably because some parts of the bending circles landed in the way that there was no compressive force along them (a tangential landing), or maybe because these segments solidified before they landed.

### 5.3.3 Buckling of bending electrospinning jets: PEO jets onto an inclined moving collector

A moving grounded collector wedge with an inclination of  $\theta = 5^\circ$  was used to collect electrospun PEO jets electrically bent into coils which buckled at the collector. The voltage between the spinneret and collector was 3 kV. Since the inter-electrode distance increased with time due to the lateral motion of the inclined collector, different features of the electrical bending circles and buckling patterns were collected along the slope of the moving collector (Figure 5.6).

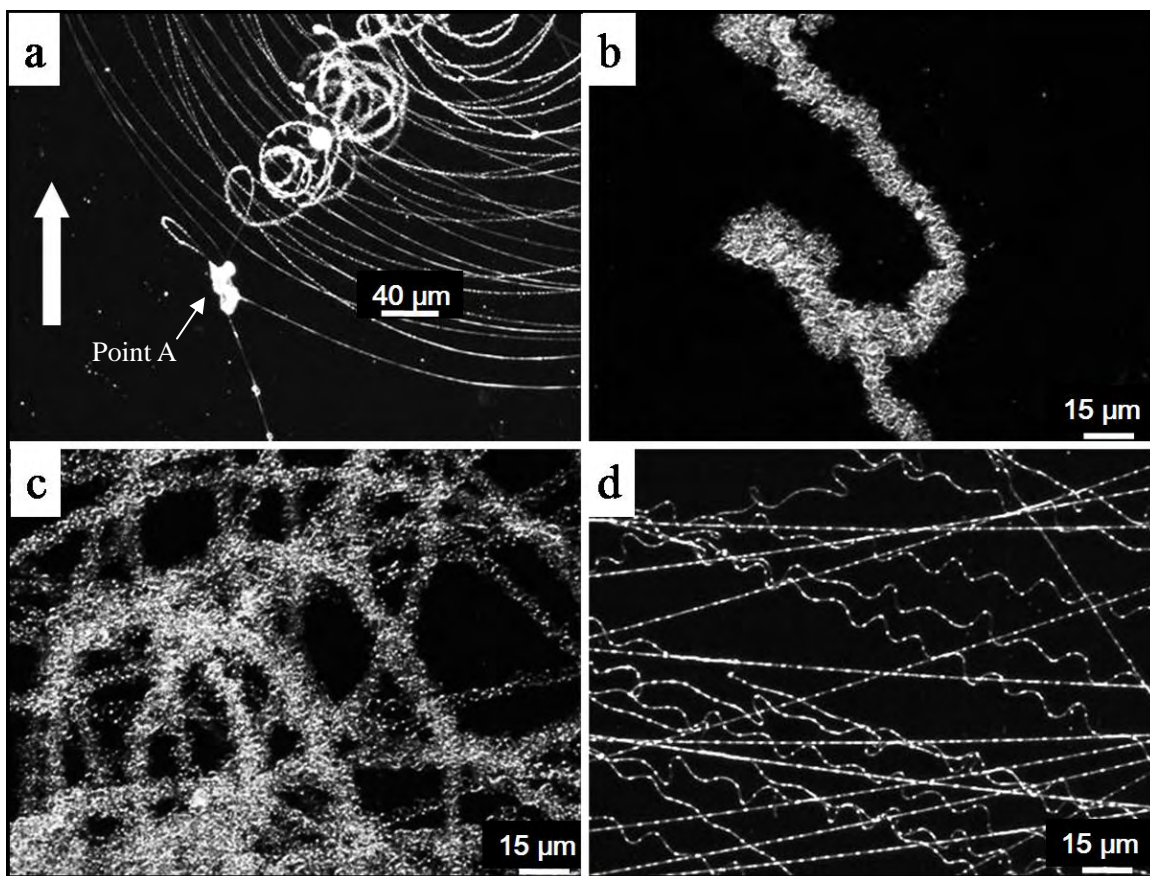


Figure 5.6 Optical images of bent and buckled PEO loops and patterns collected at different inter-electrode distances on the surface of a inclined collector which moved at 0.01m/s along the direction shown by the white wide arrow in Figure 5.6-a.

Figure 5.6-a shows the large-scale loops originating from the electrical bending instability corresponding to a relatively short inter-electrode distance. The fluid jet accumulated into a droplet near point A in Figure 5.6-a as the motion started, and then deposited small bending circles which buckled. The bending circles rapidly became larger in diameter and the piled rows of buckling patterns formed the patterns shown in Figure 5.6-b. This figure details the buckling patterns superimposed on the very first bending loops. Figure 5.6-c shows the bending loops with the superimposed buckling patterns corresponding to the intermediate inter-electrode distances. Figure 5.6-d

shows the bending loops with the superimposed buckling patterns corresponding to the largest inter-electrode distance. The above-mentioned figures demonstrate that the buckling frequency and wave length both vary with the inter-electrode distance. This results from the fact that as the inter-electrode distance increases, the impinging jet becomes thinner, acquires a higher velocity, and has different rheological parameters, due to solvent evaporation. So the buckling frequency is higher at shorter collecting distances and lower at larger distances. As a result, the piled buckling patterns were more densely packed at the shorter inter-electrode distances and more loosely packed at the larger distances.

#### 5.3.4 Buckling of straight electrified jets: PLLA jets collected on a horizontal moving grounded plate

PLLA 5wt% solution in HFIP was used. The distance from the capillary orifice to the grounded collector was 2 cm. The collector was moved laterally at 1 m/s. The applied voltage was 1.5 kV. Under these conditions, for this particular polymer solution the electrical bending instability did not occur and the path of the jet toward the collector was straight. Near the collector the jet buckled. The deposited and solidified buckled patterns collected on glass microscope slides were observed using optical microscopy. The charge carried by the jet was quickly relaxed due to the surface conductivity of the glass. Figure 5.7 shows the solidified buckled patterns produced from the straight PLLA

jet. The diameters of the solidified PLLA fibers were around 1  $\mu\text{m}$  to 2  $\mu\text{m}$ . Sinuous patterns are shown in Figure 5.7-a and helical patterns are shown in Figure 5.7-b. Zig-zags with straight segments only about 45  $\mu\text{m}$  long were found in twisted rows, Figure 5.7-c and in flat arrays, Figure 5.7-d.

For such patterns the micrographs allow measurement of the corresponding wavelength  $\lambda$  (Figure 5.7-a, b, d). The measured wave lengths were around 6  $\mu\text{m}$  to 12  $\mu\text{m}$ . The corresponding frequencies  $\omega$  defined as  $\omega = V_r/\lambda$  (with  $V_r$  being the lateral velocity of the collector  $V_c$ , since the straight jet did not have any lateral motion of its own) were around  $0.83 \times 10^5$  Hz to  $1.67 \times 10^5$  Hz. In some cases (Figure 5.7-c) the buckled deposits were rather chaotic, so that it was impossible to ascribe them to any  $\lambda$ . The buckling patterns produced by the straight electrified jets resemble those found for buckling of uncharged rectilinear jets impinging on moving plates<sup>146, 147</sup>.

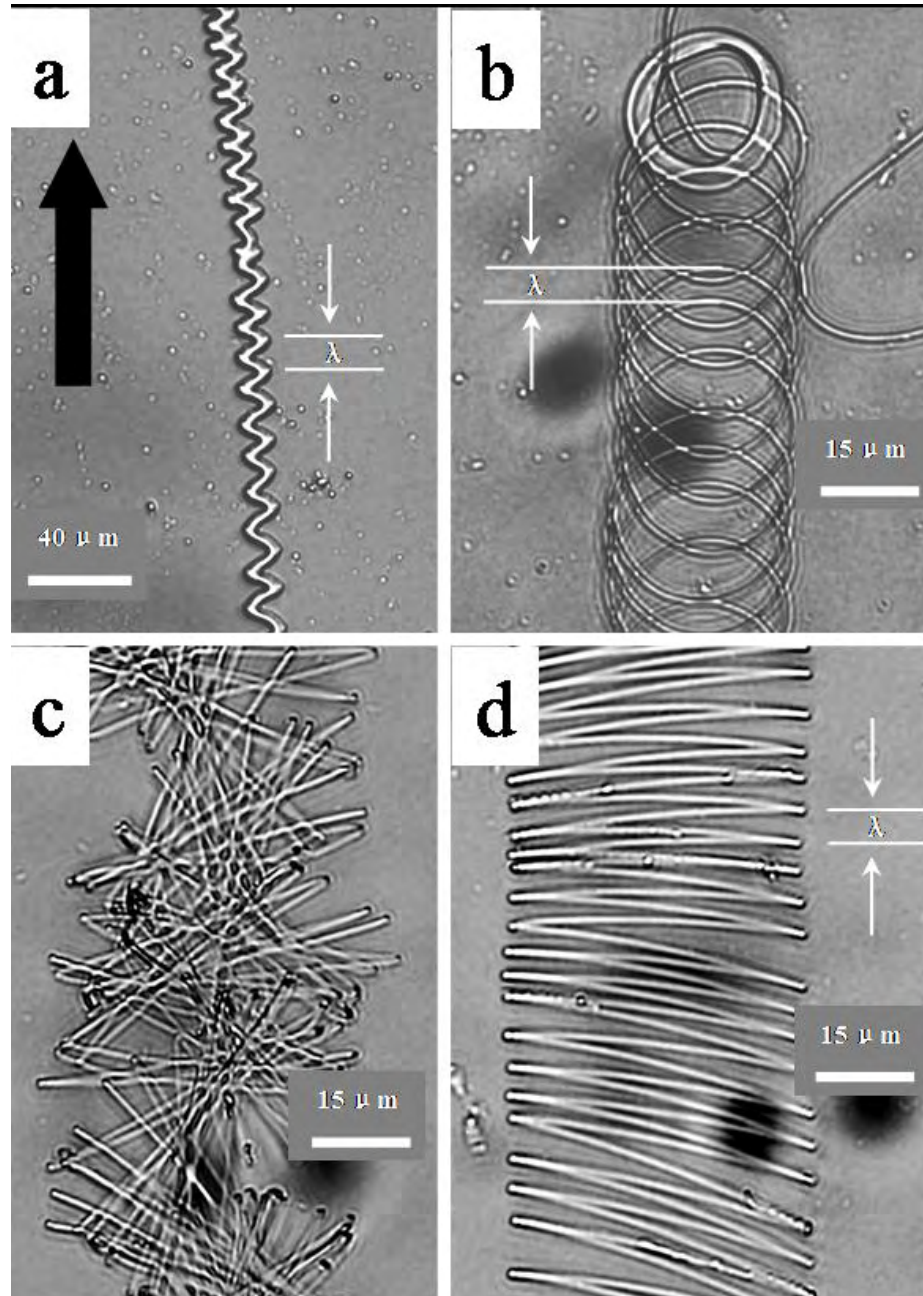


Figure 5.7 Optical images of buckled solidified PLLA patterns. The horizontal collector was moved in direction shown by the black arrow in Figure 5.7-a .The distance  $\lambda$  (the wave length) corresponds to the lateral motion during one period of the formation of the buckling patterns.

### 5.3.5 Buckling of straight electrified jets: Polystyrene jets onto a horizontal moving grounded plate

The polystyrene 25 wt% DMF solution was used. The distance from the tip to the collector was 2 cm. The collector was moved laterally at 2 m/s. The voltage was 3 kV. Under these conditions, the electrical bending instability did not occur and only a straight jet was observed. The axial velocity of the jet was around 2 m/s before it impinged onto the collector surface. The solidified buckled patterns collected on a glass slide were observed using optical microscopy. Figure 5.8 and Figure 5.9 show the patterns observed on buckled polystyrene jets. The diameters of the jets were around 2  $\mu\text{m}$  to 6  $\mu\text{m}$ . Figure-eight (Figure 5.8-a), sinuous folding (Figure 5.8-b), helical coiling (Figure 5.8-c) and overlapping script-like "e" (Figure 5.8-d, Figure 5.9-c, Figure 5.9-d) were observed. Also "paper clip chain" (Figure 5.9-a), and "knee-like" (Figure 5.9-b) patterns were formed under some circumstances. The wave lengths were measured from the micrographs and were found to be around 6 to 30  $\mu\text{m}$ . The corresponding frequencies were around  $0.67 \times 10^5$  Hz to  $3.3 \times 10^5$  Hz.

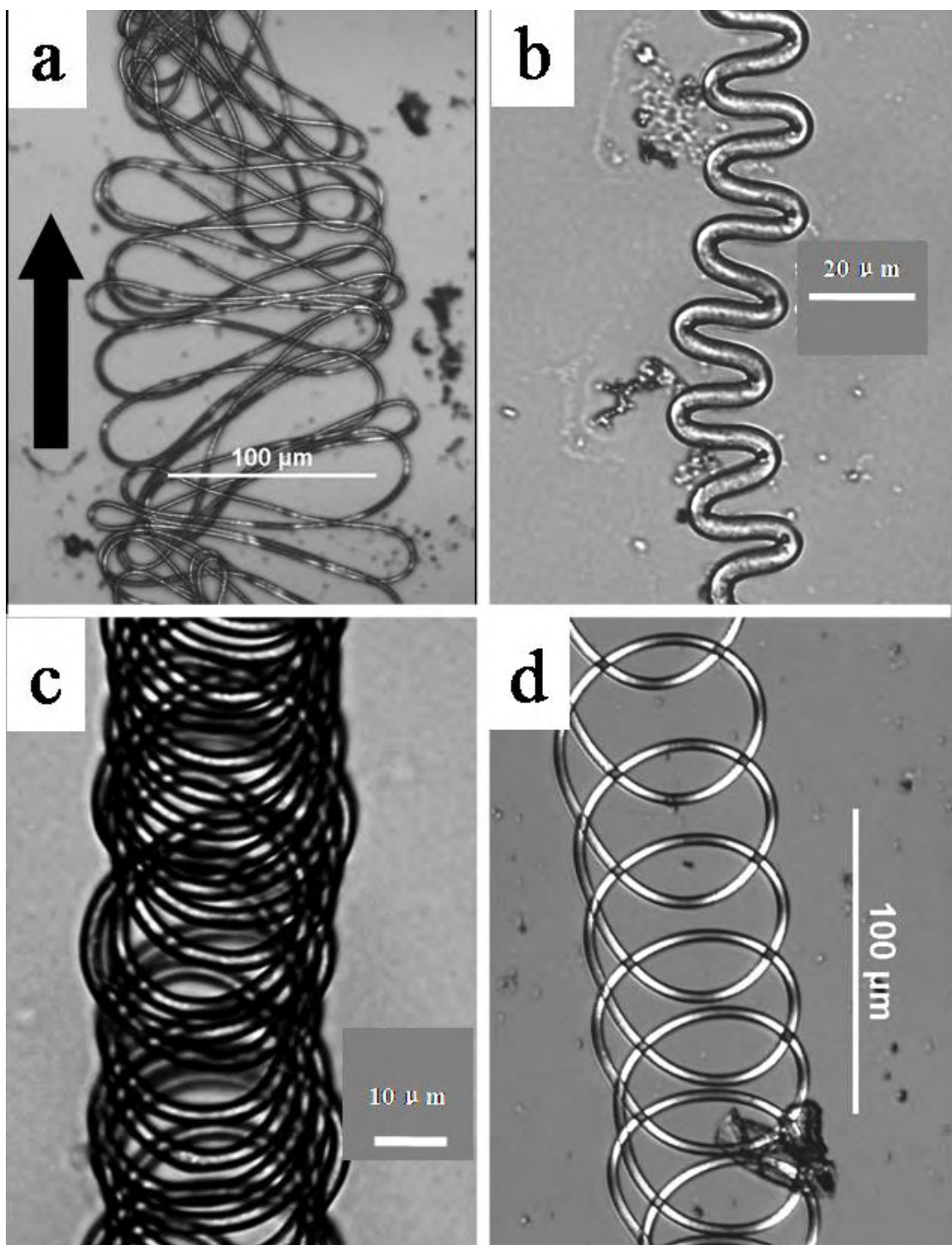


Figure 5.8 Optical micrographs of buckled polystyrene patterns. The horizontal collector was moved in the direction shown by the black arrow in Figure 5.8-a.

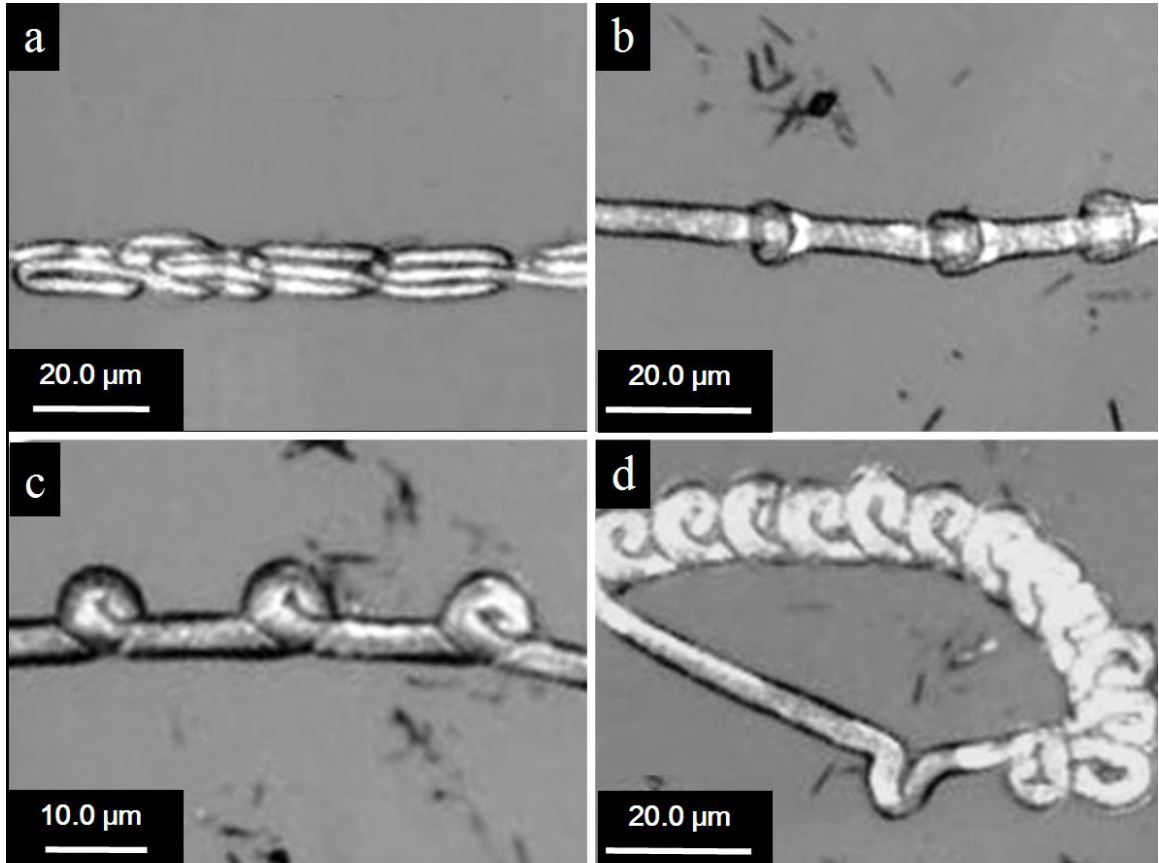


Figure 5.9 Optical micrographs of buckled polystyrene patterns collected on a static water surface.

In some experiments a stationary water surface was used as a collector. The straight jet buckled as it impinged onto the surface and then sank into the water. Three-dimensional buckling morphologies were shaped as a coiling spring (Figure 5.10). The diameter of the three-dimensional coil was around 20  $\mu\text{m}$ .

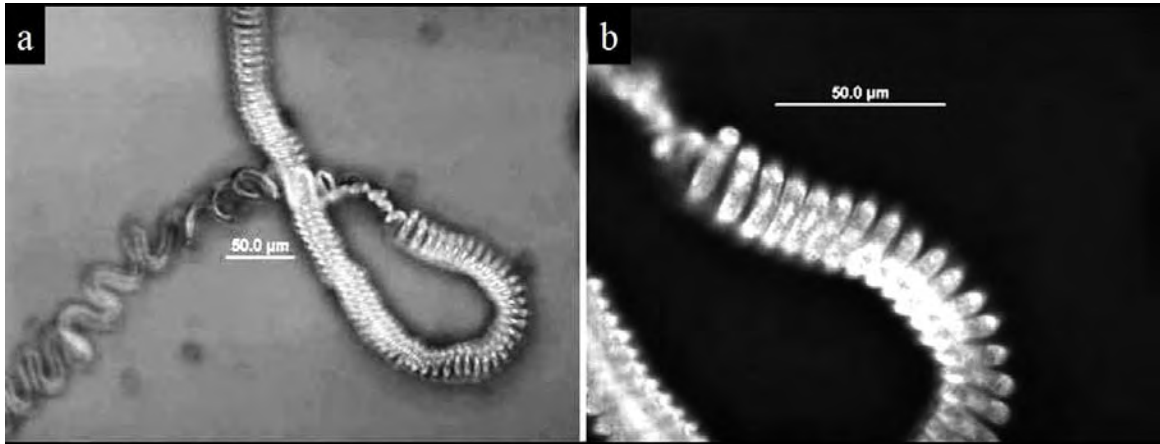


Figure 5.10 Three-dimensional buckled patterns formed after the impingement of a polystyrene jet onto a water surface. The samples were dipped from the water with a glass microscopic slide and observed with the optical microscopy.

### 5.3.6 Buckling of bending electrospun jets: nylon-6 onto an inclined moving collector

A moving collector with an inclination of  $\theta = 18.5^\circ$  was used to collect electrospun jets of nylon-6 (10 wt% in an 8/2 mixture of HFIP and FA). The simultaneous evolution of the electrical bending and buckling was observed (Figure 5.11). The direction of the collector motion is shown by the bold black arrow in Figure 5.11-c. Since the inter-electrode distance increased from about 0.1 cm to about 7.5 cm with time due to the motion of the inclined collectors, different patterns were observed along the collector surface (Figure 5.11). Figure 5.11-c is an overall view of the deposited fiber along the wedge slope. Four sections of the overall view are enlarged in Figures 5.11-a, b, d, e as is shown by white arrows in Figure 5.11. The nearly straight segment of the jet formed a complex, sinuous network of smaller loops, as shown at higher magnification in Figure

5.11-a. At a larger inter-electrode distance, the bending instability produced loops 200  $\mu\text{m}$  in diameter with superimposed, much smaller, buckling patterns that were 15  $\mu\text{m}$  in diameter, as is seen in Figure 5.11-b and Figure 5.11-d. Near the right edge of Figure 5.11-c, parts of larger coils formed by the electrical bending were observed. The enlarged image shown in Figure 5.11-e shows coils and sinuous patterns caused by buckling. Figure 5.11-c shows that the buckling instability occurred both before and after the electrical bending instability developed, and produced coils or sinuous patterns with diameters a little less than 15  $\mu\text{m}$ , in the region shown in Figure 5.11-a and a little more than 15  $\mu\text{m}$  in the region shown in Figure 5.11-e.

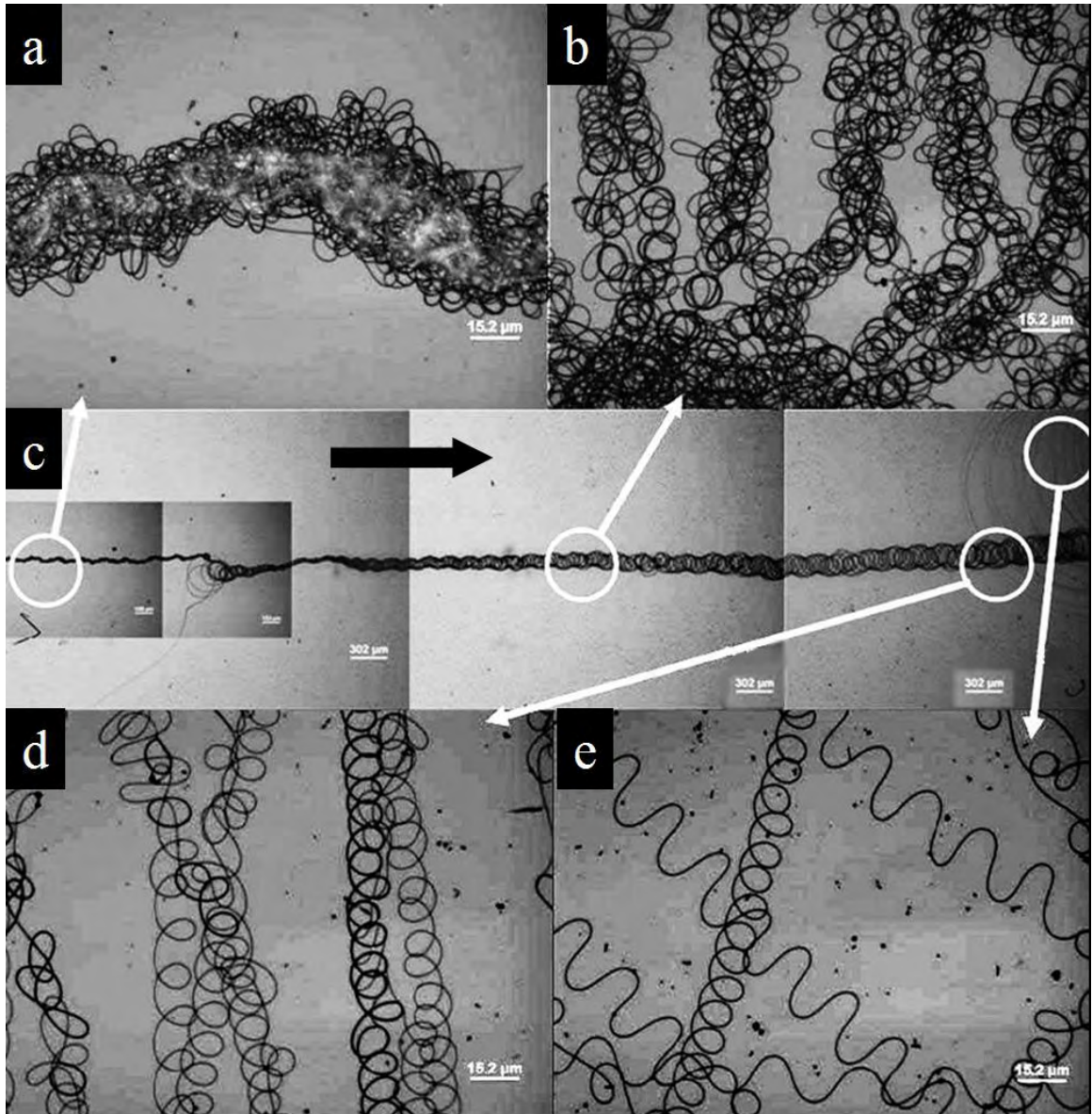


Figure 5.11 Buckled and bent electrospun nylon-6 deposits. The lengths of the horizontal edges of the images a, b, d, e are 0.18 mm; the length of the horizontal edge of the image c is 9.0 mm. The total change in the inter-electrode distance was about 0.3 cm from the left edge to the right edge in Figure 5.11-c.

### 5.3.7 Comparisons between the buckling instabilities of uncharged fluid jets and electrified fluid jets

The experimental data presented previously show that the deposited buckling patterns of the electrified jets have reproducible characteristics that are similar to those found previously in uncharged jets collected by impingement on a moving hard flat surface<sup>146,147</sup> irrespective of whether the electrically-driven jet was straight or bent prior to interaction with the collector. Similarities between charged and uncharged buckling jets are clearly apparent (Figure 5.12 and Figure 5.13 for polyethylene oxide and nylon-6, respectively). For the uncharged jets it was shown that the characteristic buckling frequency is not significantly dependent on the velocity of lateral motion of an obstacle, being in fact the same as for a motionless collector<sup>147</sup>. Therefore, the predicted buckling frequencies for the impingement of the uncharged jet onto a motionless plate<sup>144</sup> can be directly compared with those measured for a charged jet impinging on a moving collector in the present work. The theoretical results for the buckling frequency were by Yarin<sup>144</sup> (shown in cf.144 Figure 13-b). They may be fitted by the following formula

$$\log\left(\omega \frac{d}{V}\right) = -0.0194 \log\left(\frac{\mu Q}{\rho g d^4}\right) + 0.2582 \quad (5.1)$$

where  $\omega$  is the buckling frequency in Hz

$d$  is the jet diameter

$V$  is the jet velocity normal to the collector

$Q$  is volumetric flow rate in the jet

$\rho$  is the density of the liquid

$\mu$  is the viscosity of the liquid

$g$  is the density of external force per unit mass (the electric force per unit mass)

Buckling is a low-speed and low-strain-rate phenomenon. Therefore, in this limit viscoelastic behavior reduces to Newtonian behavior with  $\mu$  being equivalent to the zero-shear viscosity.

In the comparison below,  $d$  and  $V$  in Eq. (5.1) were evaluated for the segment of the jet near the collector, and used to find  $\bar{\omega}_{calculated}$  using the other parameters corresponding to specific experiments. In addition, the values of  $\bar{\omega}_{measured}$  were independently measured using the deposited patterns, as described in Section 3. Comparisons of  $\bar{\omega}_{calculated}$  and  $\bar{\omega}_{measured}$  are presented in Table 5.1 with data from Figure 5.4 to Figure 5.14 for polyethylene oxide, PLLA, polystyrene and nylon-6. Equation (1) was used to calculate the values of  $\bar{\omega}_{calculated}$  in all the cases. It is emphasized that the values  $\log\left(\omega \frac{d}{V}\right)$  and  $\log\left(\frac{\mu Q}{\rho g d^4}\right)$  for the electrified jets in the present work extrapolate outside the range covered by the theoretical data<sup>144</sup> fitted by Eq. (5.1). Nevertheless, the comparisons in Table 5.1 show reasonable agreement between the predictions based on Eq. (5.1) and the current experimental data.

Figure 5.12 and Figure 5.13 show that most of the buckling morphologies found in the present work, for the electrified jets, have their counterparts in those for much larger uncharged, gravity-driven jets by Chiu-Webster et al.<sup>146, 147</sup>. However, there are several other morphologies (Figure 5.14), which were not observed before.

Several morphological structures reported by Kessick et al.<sup>148</sup> and Shin et al.<sup>149</sup> can be attributed to buckling of bending electrospinning jets. However, in these works the real origin of the observed deposits was not uncovered. Kessick et al.<sup>148</sup> claimed that such deposit morphologies could not be obtained with non-conducting polymer nanofibers landing on non-metal substrates, and thus attributed them to the competition of charge relaxation and viscoelasticity. The claim was found to contradict to the data by Shin et al.<sup>149</sup>, as well as it does not agree with the results of the present work where one of the non-conducting polymers, PEO, was the same as in Kessick's work<sup>148</sup>. On the other hand, Shin et al.<sup>149</sup> attributed the micro scale coiled deposits to the ordinary bending instability, while considering macroscopic segments as straight. However, in reality the macroscopic segments are coiled (due to the bending instability) with a much larger radius of curvature. The distinction between the microscopic and macroscopic coils is clearly demonstrated in the present work, and their different physical natures are attributed to two physically different phenomena-mechanical buckling and the electrical bending, respectively.

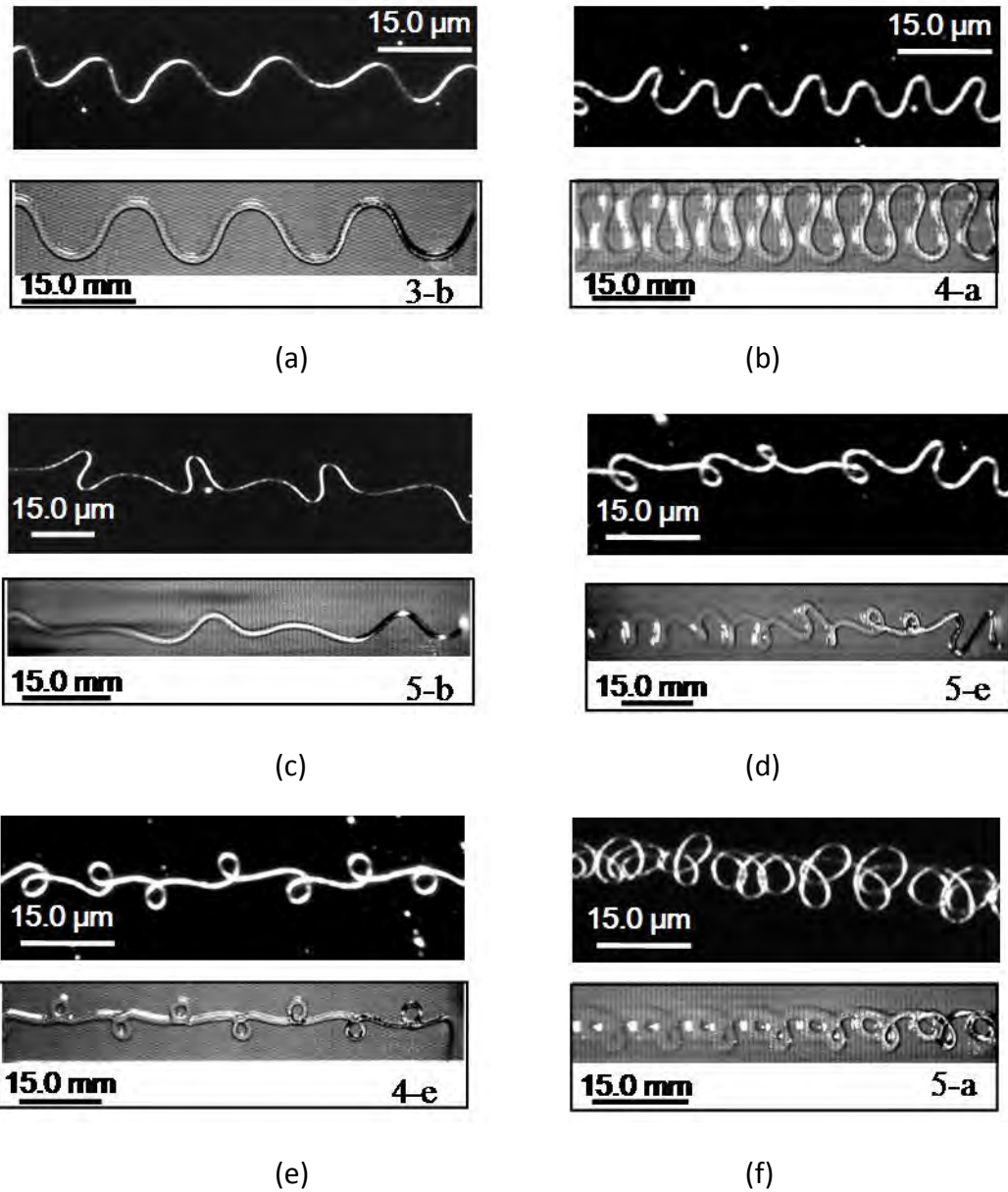


Figure 5.12 Comparison of the buckled patterns created by electrified jets of polyethylene oxide in water, collected on glass slides, to patterns<sup>146</sup> produced by the buckling of uncharged gravity-driven syrup jets. Note that the gravity-driven syrup jets and their buckling patterns are about 1000 times larger than those of the electrified jets of polyethylene oxide in water. The upper panel in each pair depicts the results for the electrified PEO jets in the present work. The lower panels show the similar patterns by the syrup jets by Chiu-Webster<sup>146</sup>. The symbols in the lower right corner of each panel are the figure number found in Chiu-Webster's work<sup>146</sup>.

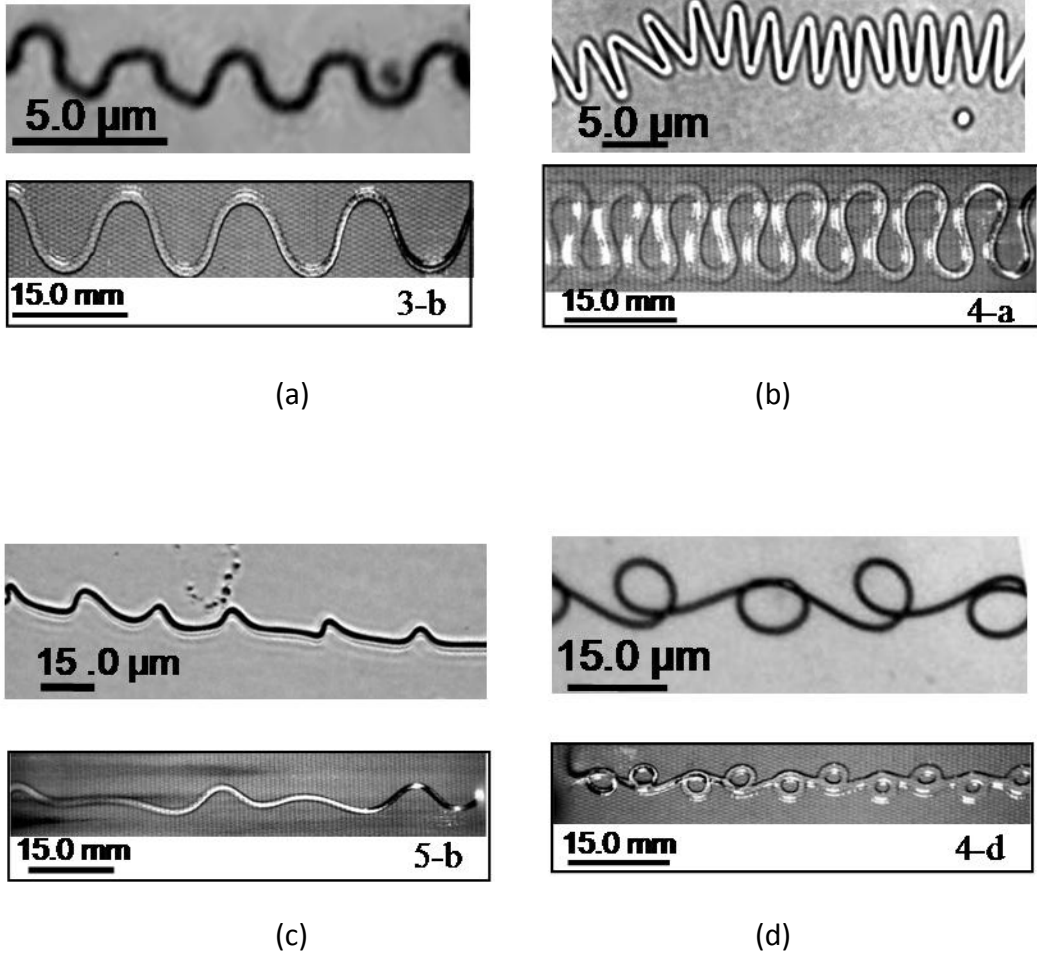
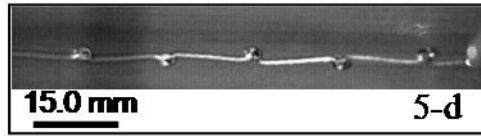
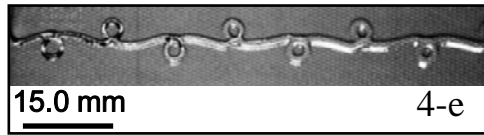
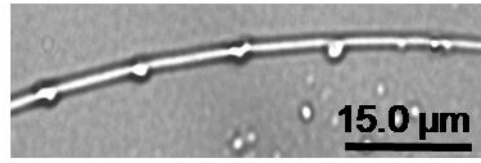
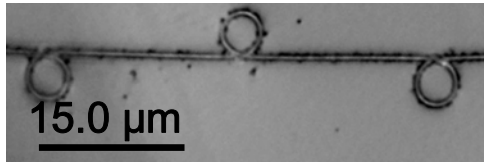
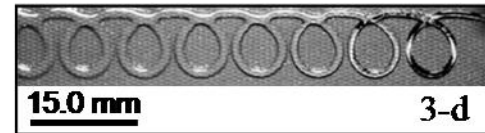
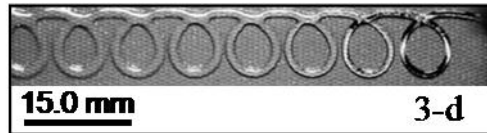
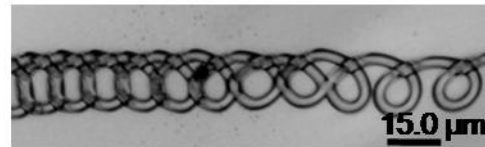
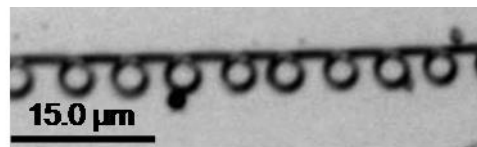


Figure 5.13 Comparison of the buckled patterns created by electrified nylon-6 jets collected on water to the buckling patterns<sup>146</sup> resulting from uncharged gravity-driven syrup jets.



(e)

(f)



(g)

(h)

Figure 5.13 Comparison of the buckled patterns created by electrified nylon-6 jets collected on water to the buckling patterns<sup>146</sup> resulting from uncharged gravity-driven syrup jets. (continued)

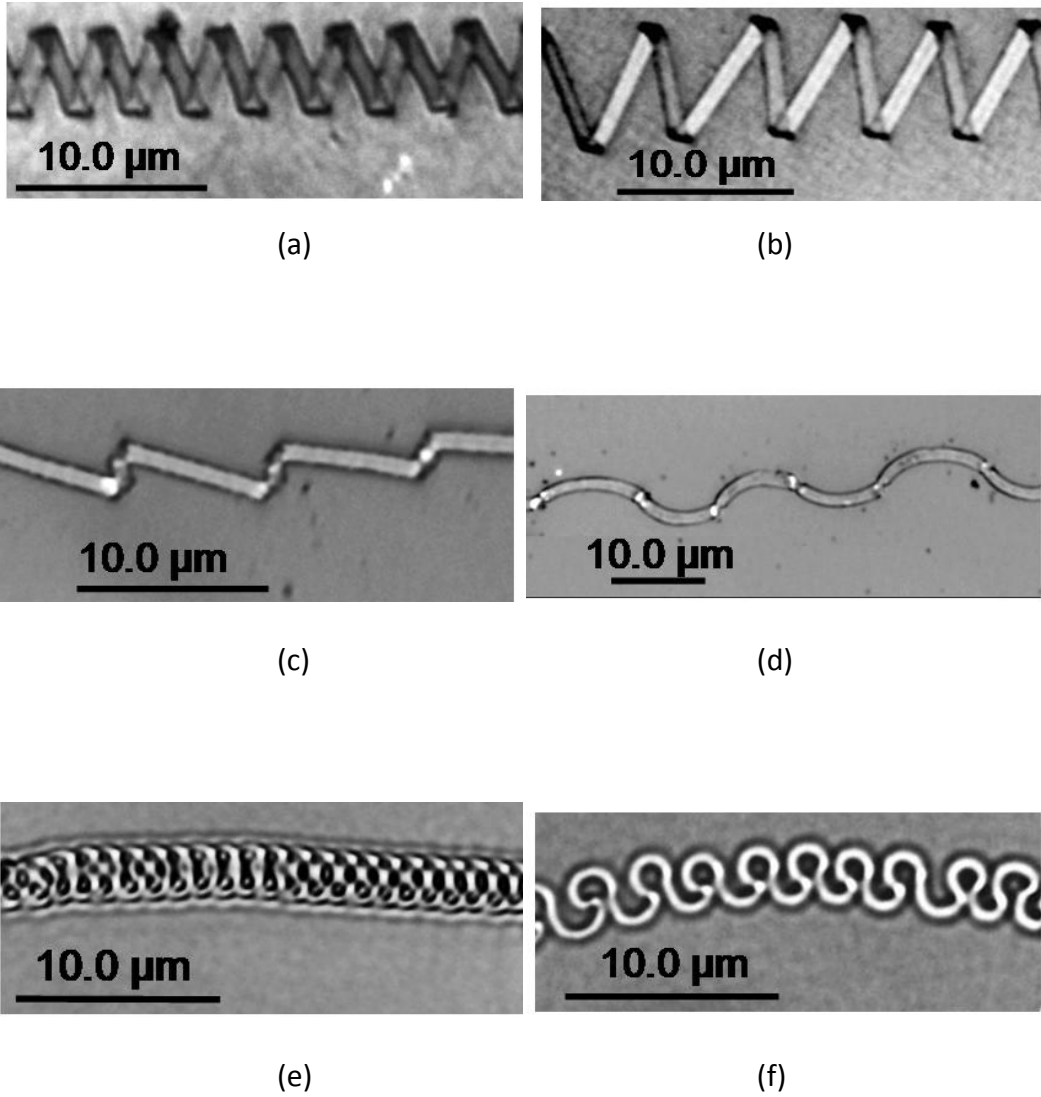


Figure 5.14 Buckled patterns created by electrified nylon-6 jets collected on a water surface. These do not have analogies among those reported by Chiu-Webster et al.<sup>146,147</sup>.

Table 5.1 Comparison of the measured and calculated buckling frequencies of electrospinning jets.

Figure	$d$	$\lambda$ ( $\mu\text{m}$ )	Cycles/mm	$\omega_{meas}$ ( $10^5$ )	$\omega_{cal}$ ( $10^5$ )	FLPC <sup>5</sup> ( $\mu\text{m}$ )	$V_r$ (m/s)
5.4	0.2	5	200	3.4	7.0	23	0.785
5.5-a	0.3	5	200	2.0	4.7		
5.5-b	0.3	5	200	2.0	4.7		
5.5-c	0.2	15	67	2.7	28.0	25	4.00 <sup>1</sup>
5.5-d	0.2	15	67	2.7	7.0	25	4.00 <sup>1</sup>
5.6-c	0.3	5	200	2.0	4.7		
5.6-d	0.2	15	67	2.7	7.0	18	4.00 <sup>1</sup>
5.7-a	3.8	14	71	0.7	0.4	25	1.00
5.7-b	1.0	7	143	1.4	1.4	82	1.00
5.7-c	1.0	1.5	667	6.7	1.4	60	1.00
5.7-d	1.1	4.8	208	2.1	1.3	60	1.00
5.8-a	2.4	17	59	1.2	1.2	334	2.00 <sup>2</sup>
5.8-b	3.9	12.3	81	1.6	0.7	41	2.00 <sup>2</sup>
5.8-c	2.4	3.2	312.5	6.2	1.2	52	2.00 <sup>2</sup>
5.8-d	2.4	30	33	0.7	1.2	100	2.00 <sup>2</sup>
5.9-a	2.7	12	83	1.7	1.0	79	2.00 <sup>2</sup>
5.9-b	4.4	23	43	0.9	0.6	31	2.00 <sup>2</sup>
5.9-c	3.9	18.5	54	1.1	0.7	44	2.00 <sup>2</sup>
5.9-d	4.4	9	111	0.2	0.6	36	2.00 <sup>2</sup>
5.10-a	6.4	8	125	2.5	0.4	73	2.00 <sup>2</sup>
5.10-b	6.4	8	125	2.5	0.4	73	2.00 <sup>2</sup>
5.11-b	0.45	2.6	385	3.8	6.2	31	1.00 <sup>3</sup>
5.11-d	0.4	8.5	118	5.9	7.0	35	5.00 <sup>3</sup>
5.11-e	0.35	20.2	50	5.0	8.0	45	10.00 <sup>3</sup>
5.12-a	0.2	13	77	1.5	3.5	19	2.00 <sup>4</sup>
5.12-b	0.2	8.4	119	2.4	3.5	17	2.00 <sup>4</sup>
5.12-c	0.2	30.6	33	6.5	3.5	46	2.00 <sup>4</sup>
5.12-d	0.2	12	83	1.7	3.5	19	2.00 <sup>4</sup>
5.12-e	0.2	10	100	2.0	3.5	19	2.00 <sup>4</sup>
5.12-f	0.2	4.2	238	4.8	3.5	21	2.00 <sup>4</sup>
5.13-a	0.3	3.4	294	5.9	9.3	5.3	2.00 <sup>4</sup>
5.13-b	0.8	2.4	417	8.3	3.5	11	2.00 <sup>4</sup>
5.13-c	1.2	23	43	0.9	2.3	26	2.00 <sup>4</sup>
5.13-d	0.7	21	48	1.0	4.0	49	2.00 <sup>4</sup>
5.13-e	0.5	20	50	1.0	5.6	33	2.00 <sup>4</sup>
5.13-f	1.2	12	83	1.7	2.3	14	2.00 <sup>4</sup>
5.13-g	0.9	5	200	4.0	3.1	10	2.00 <sup>4</sup>
5.13-h	2.6	11	91	1.8	1.1	44	2.00 <sup>4</sup>
5.14-a	1.2	3.2	312	6.2	2.3	10	2.00 <sup>4</sup>

Table 5.1 Comparison of the measured and calculated buckling frequencies of electrospinning jets. (continued)

Figure	$d$ ( $\mu\text{m}$ )	$\lambda$ ( $\mu\text{m}$ )	Cycles/mm	$\omega_{meas}$ ( $10^5$ Hz)	$\omega_{cal}$ ( $10^5$ Hz)	FLPC <sup>5</sup> ( $\mu\text{m}$ )	$V_r$ (m/s)
5.14-b	1.2	5.4	185	3.7	2.3	15	$2.00^4$
5.14-c	1.0	8.3	120	2.4	2.8	10	$2.00^4$
5.14-d	1.3	10	100	2.0	2.2	11	$2.00^4$
5.14-e	0.45	1.2	833	16.7	6.2	6	$2.00^4$
5.14-f	0.45	2.5	400	8.0	6.2	8	$2.00^4$

- 1,3,4.  $V_r$ : The radial velocity of a typical segment of an electrical bending coils relative to the collector. The value was determined from the high frame rate video.
2.  $V_c$ : The velocity of the collector relative to the straight electrified jet.
5. FLPC (Fiber length per cycle) is defined as the distance along the path of the jets between adjacent identical segments of the repeating patterns.

#### 5.4 SUMMARY

Two-dimensional and three-dimensional buckling phenomena were studied in electrically charged jets that impinged onto collectors that were moving laterally. At short inter-electrode distances the electrified jet was straight, whereas at large distances the jet developed electrical bending coils. Both straight and electrically-bent jets buckled near the collector. In the case of bending electrospinning jets, short wave-length buckling patterns were superimposed on long-wave length electrical bending loops. The frequency corresponding to the buckling was in the range of  $10^5$  to  $10^6$  Hz, and the frequency for the bending loops was about  $10^3$  Hz. Most of the morphologies (but not all) of the deposited buckling patterns resembled the patterns produced by uncharged, highly viscous, gravity-driven jets impinging onto a moving, hard, flat surface published recently<sup>146</sup>. Frequencies derived from observations of the buckling patterns were

compared to those predicted for uncharged jets impinging on a motionless, hard, flat surface. Reasonable agreement of theoretical and experimental results was found. To conclude, the morphologies of the electrospun fibers were manipulated by control of the buckling instability of jets. Various two-dimensional and three-dimensional micron-size patterns were produced by the buckled electrospun fibers.

## CHAPTER VI

### PENDULUM-LIKE MOTION OF STRAIGHT ELECTRIFIED JETS

#### 6.1 INTRODUCTION

Straight electrified jets of low viscosity Newtonian liquids were investigated experimentally and theoretically since the end of the 19<sup>th</sup> century, mostly on the effect of the electric field on the capillary instability<sup>55,150,151,152,153,154,155</sup>. Later on, when electrically-driven jets of highly viscous Newtonian liquids or of viscoelastic polymer solutions came into focus, a number of experimental and theoretical papers aimed at prediction of the tapering shape of such straight jets<sup>5,75,85,87,88,95,156</sup>. In addition it was discovered that straight electrified jets can become unstable to the electrically-driven bending perturbations and make large, rapidly evolving loops which elongate rapidly the thin liquid jet in the industrially important process called electrospinning of polymer nanofibers<sup>5,6,82,83,131,157,158,159,160</sup>. Secondary electrically-driven instabilities leading to jet branching were also theoretically predicted and observed in the experiments<sup>5,81,161</sup>. Buckling of electrified straight and bending jets was also studied<sup>4</sup>. A new phenomenon characteristic of electrified jets is described here. It is shown that for short enough jets, when bending instability is absent, usually straight segment arched in a radial direction and rotated as a pendulum.

## 6.2 EXPERIMENTAL

Nylon-6, 25 wt% solution in formic acid (FA, 88 %). All chemicals were purchased from Sigma-Aldrich Co.

The experimental setup (Figure 6.1) for electrospinning was similar to those used previously. The collector might be either motionless or move horizontally at

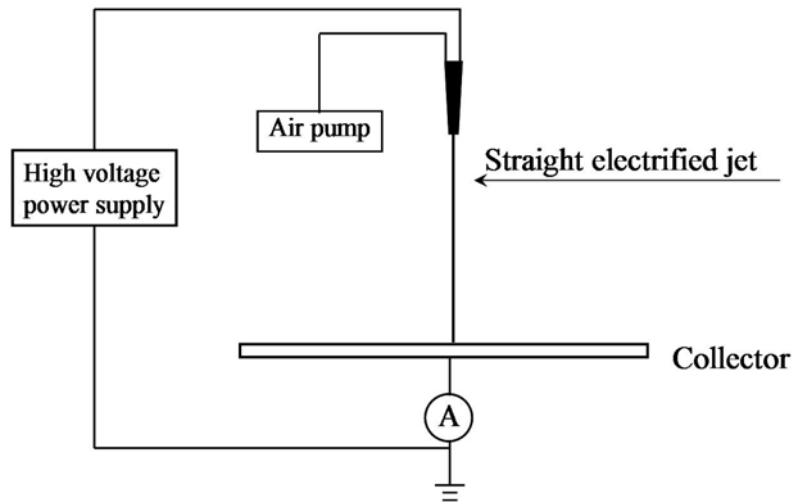


Figure 6.1 Schematic drawing of the experimental setup.

a constant speed of  $V_c = 0$  m/s to 0.01 m/s. In some experiments a grounded liquid surface was used as collector. The experiments were conducted under ambient conditions at room temperature and relative humidity of about 25 %. Polymer solutions were held in a glass pipette which had the inner diameter of 800  $\mu\text{m}$ . A copper wire was immersed in the solution and connected to a high voltage power supply which could generate DC voltage up to 13 kV. No syringe pump was used. The flow was controlled by the outward electrical Maxwell stresses and the air pressure or partial vacuum applied to the surface of the liquid in the pipette. The distance between the pipette tip and the

collector along the straight vertical line could be adjusted from 0.1 cm to 3 cm. An ammeter was connected between the collector and electrical ground to measure the current carried by the jet.

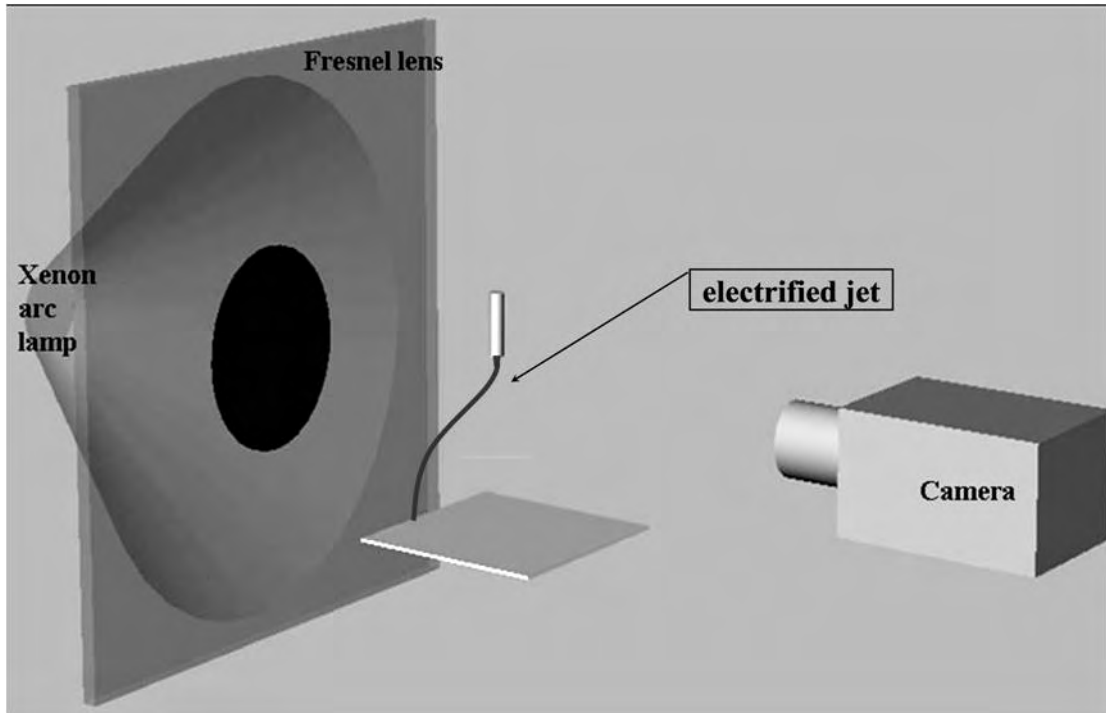


Figure 6.2 Setup for the observation of the jet.

High frame-rate camera hooked to an optical microscopy ( $4.8\times$ ) was used to record the morphology of the jet (Figure 6.2). The Fresnel lens produced a converging cone of illumination at the location of the electrified jet. The opaque disk on Fresnel lens prevented light from the arc lamp from entering the camera. Enough light scattered by the jet and entered the camera and allowed observations of the jet path.

Collected solidified electrospun fibers were observed with optical microscopy (Olympus 51BX) and Scanning Electron Microscopy (JEOL 5310).

### 6.3 RESULTS AND DISCUSSIONS

The Nylon-6 fibers were collected on the collector which was motionless or moving laterally with a speed of 0.001 m/s or 0.01 m/s. The inter-electrode distances were quite small. Therefore, the jets stayed straight or almost straight and did not develop any large scale looping of the bending instability in electrospinning<sup>5</sup>. However, the jets began swinging and rotating as a pendulum following an almost periodic closed trajectory on the grounded electrode.

#### 6.3.1 Experimental results

A view of the pendulum-like jet is shown in Figure 6.3. The closed trajectories of the jet end over the grounded electrode were almost circular. When the electrode moved laterally, a family of such circles intersecting each other was deposited (Figure 6.4). Sharpness of the edges of the deposited lines depended on the inter-electrode distance and the applied voltage (Figure 6.4 and Figure 6.5). When the inter-electrode distance was increased from 0.8 cm to 3 cm at a fixed voltage of 4 kV (Figure 6.5 to Figure 6.8), the jet segments impacting the grounded electrode became thin enough for buckling to occur<sup>3,4</sup>. Then, the deposited circular lines on the grounded electrode acquired a small-scale zigzag-like structure, which was more pronounced the larger inter-electrode distance was (Figure 6.6 to Figure 6.8).

Figure 6.9 to Figure 6.13 contain overall information on the electrified jets moving as a pendulum under different conditions. Figure 6.9 depicts the electrical current transferred by the jets to the grounded electrode versus the inter-electrode distance  $H$  for several values of the applied voltage in the range of 3 kV to 6 kV. A similar dependence for the whole angle at the vertex of the cone enveloping the pendulum jet configurations is shown in Figure 6.10.

The frequency of the pendulum-like motions of the electrified jets at different inter-electrode distances and voltages are combined in Figure 6.11. Diameters  $D$  of the collected patterns and landing velocities of the jet end  $V_{jet\ end}$  versus the inter-electrode distance  $H$  for different values of the applied voltage are presented in Figure 6.12 and Figure 6.13, respectively.

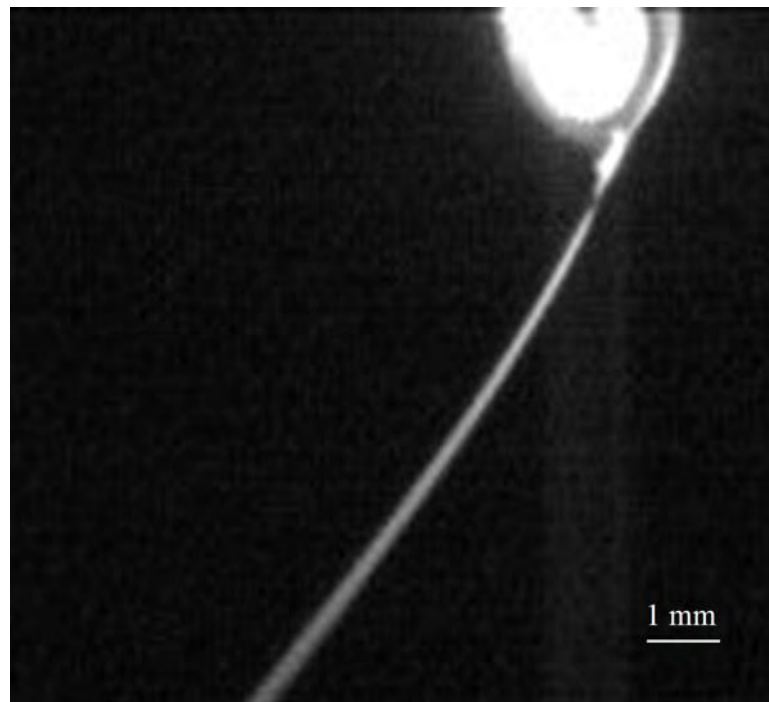


Figure 6.3 High frame rate video image of an electrified pendulum-like jet above the collecting surface. The voltage was 3 kV, the inter-electrode distance was 2.6 cm.

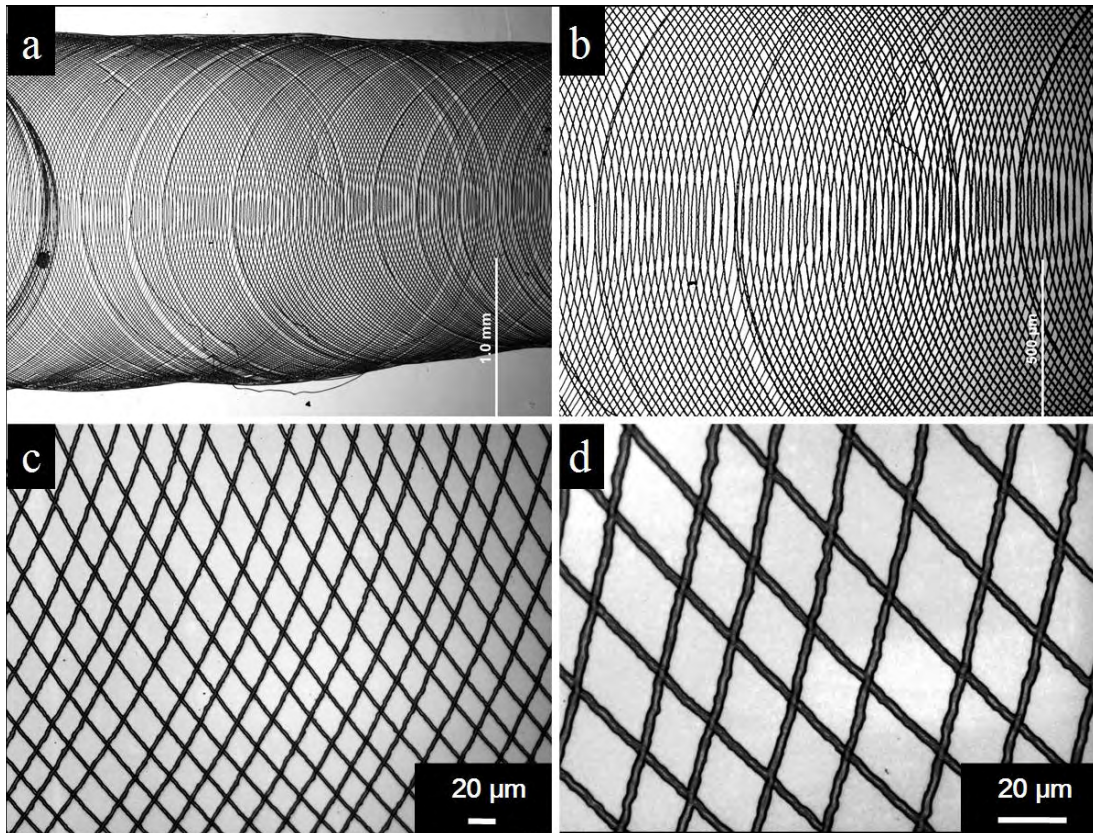


Figure 6.4 Optical microscopic images of patterns deposited by electrified jet moving as a pendulum. The voltage was 3 kV, the inter-electrode distance was 0.5 cm; the grounded electrode was moved horizontally at 0.001 m/s.

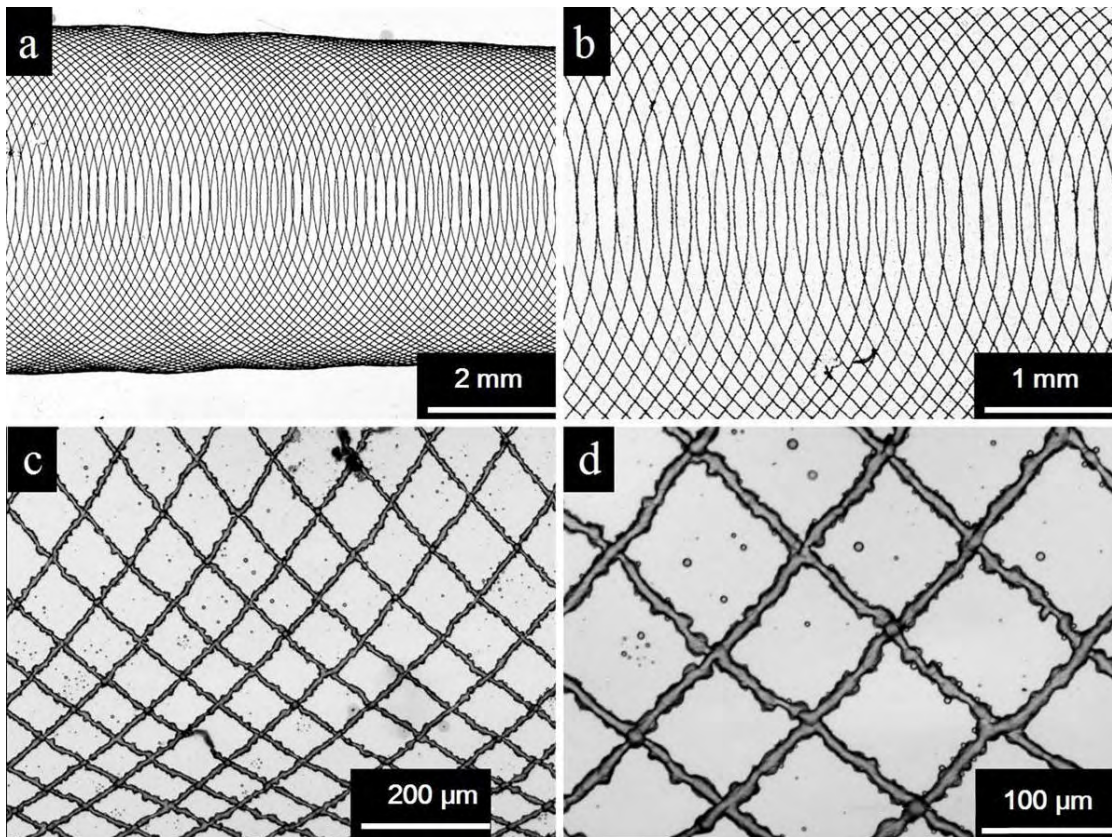


Figure 6.5 Optical microscopic images of patterns produced from electrified jet moving as a pendulum. The voltage was 4 kV, the inter-electrode distance was 0.8 cm; the grounded electrode was moved horizontally at 0.01 m/s.

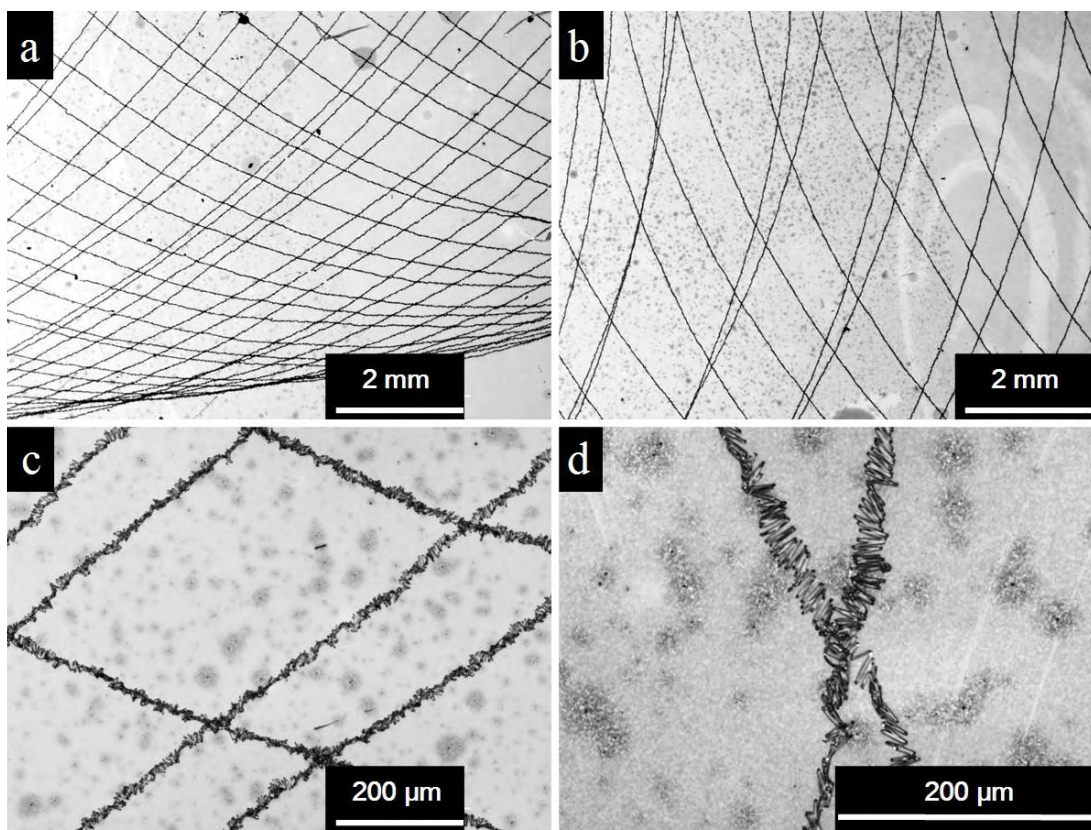


Figure 6.6 Optical microscopic images of patterns produced from electrified jet moving as a pendulum. The voltage was 4 kV, the inter-electrode distance was 1.8 cm; the grounded electrode was moved horizontally at 0.01 m/s.

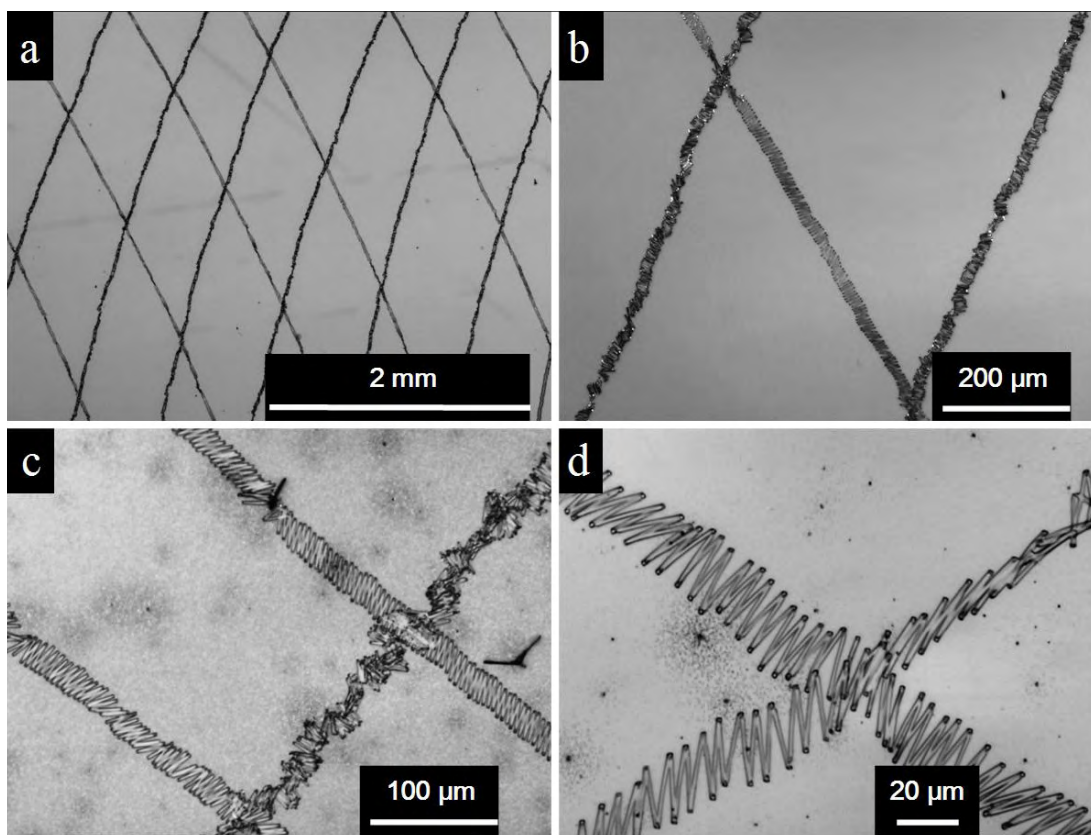


Figure 6.7 Optical microscopic images of patterns produced from electrified jet moving as a pendulum. The voltage was 4 kV, the inter-electrode distance was 2.0 cm; the grounded electrode was moved horizontally at 0.01 m/s.

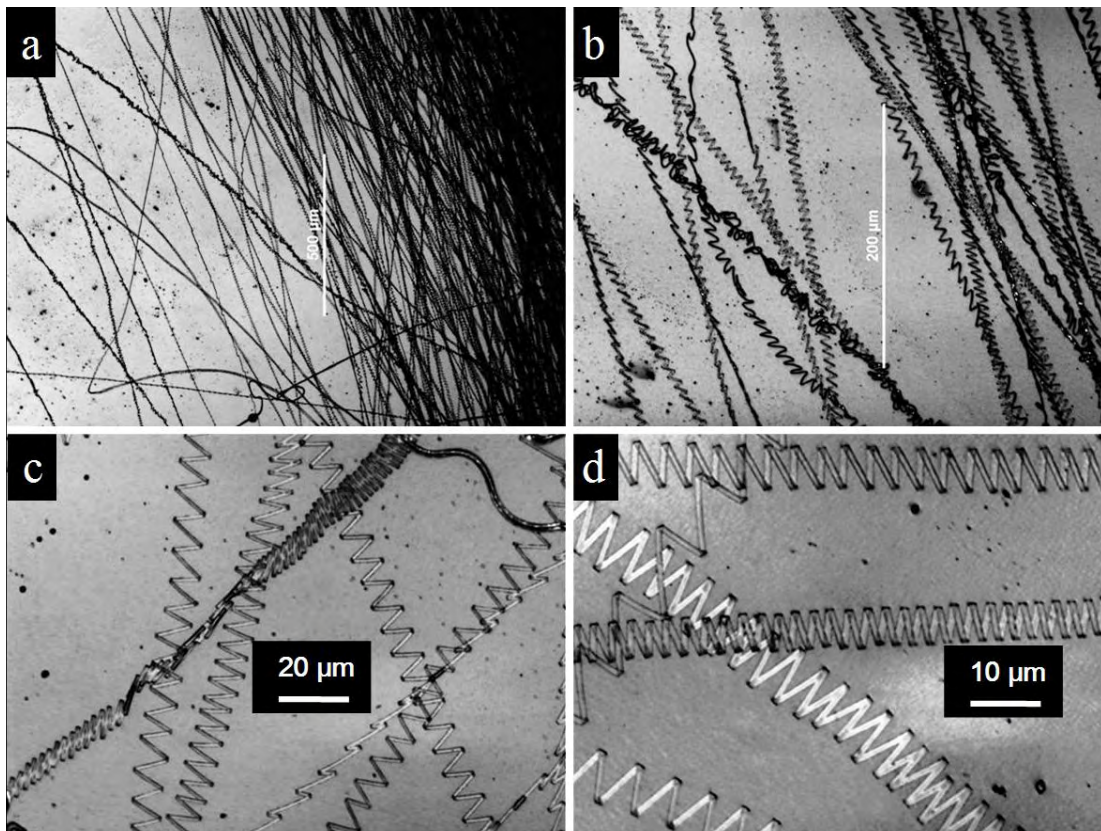


Figure 6.8 Optical microscopic images of patterns produced from electrified jet moving as a pendulum. The Nylon-6 fibers were collected on the static water surface which served as a grounded electrode. The voltage was 4 kV; the inter-electrode distance was 3.0 cm.

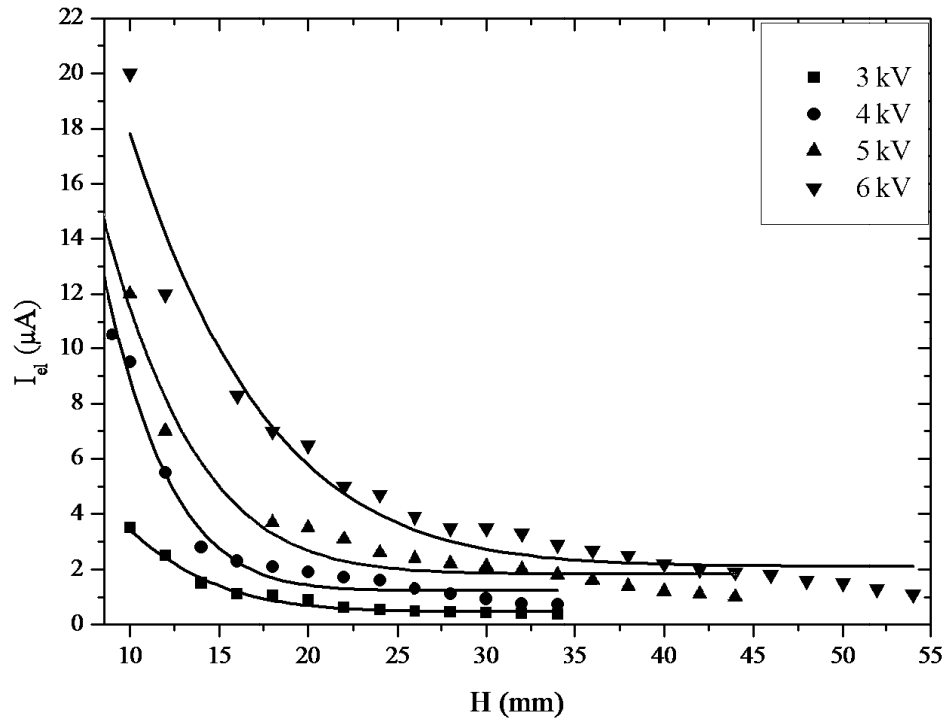


Figure 6.9 The electrical current carried by the electrified straight jets as a function of the inter-electrode distance for different applied electrical voltages. A horizontal motionless aluminum sheet was used as a grounded collector (electrode).

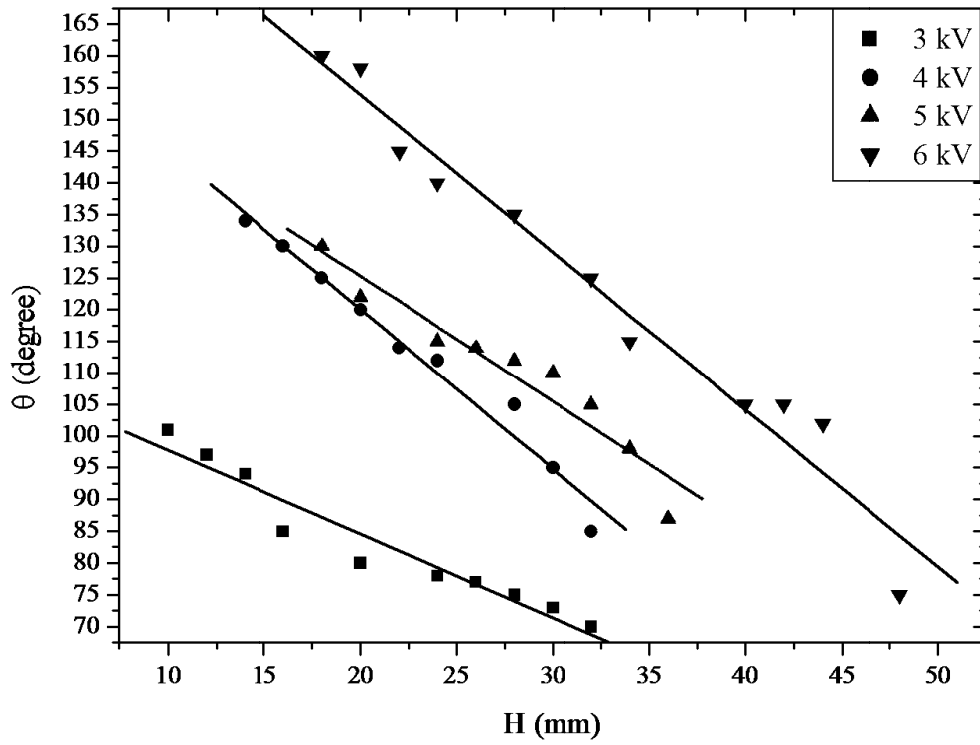


Figure 6.10 Envelop angle about the electrified pendulum jet configurations as a function of the inter-electrode distance for different applied electrical voltages. A horizontal motionless aluminum sheet was used as a grounded collector (electrode).

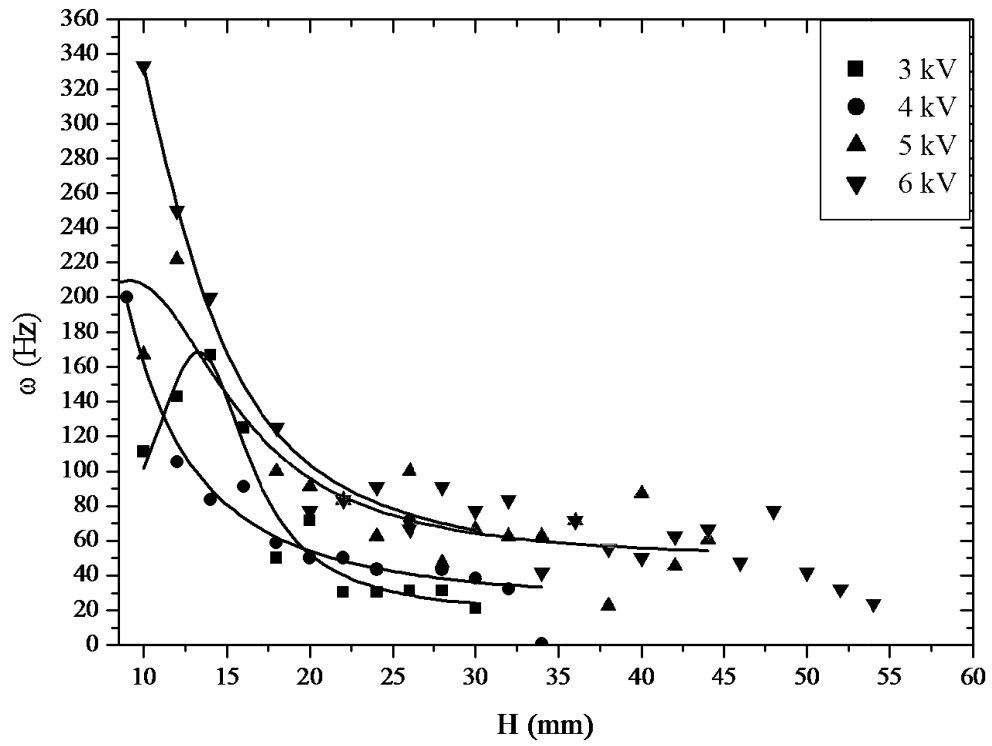


Figure 6.11 Rotation frequency  $\omega$  of the pendulum-like motion of the electrified jets as a function of the inter-electrode distance for different applied electrical voltages. A horizontal motionless aluminum sheet was used as a grounded collector (electrode).

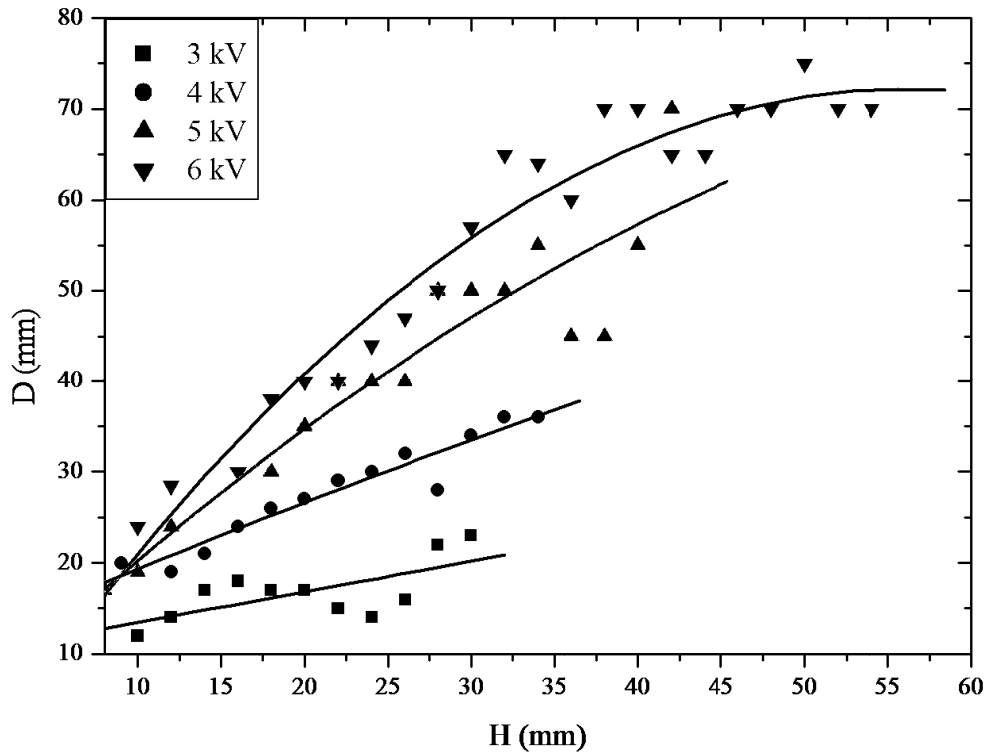


Figure 6.12 Diameter of the collected circular deposits of the electrified jets as a function of the inter-electrode distance for different applied electrical voltages. A horizontal motionless aluminum sheet was used as a grounded collector (electrode).

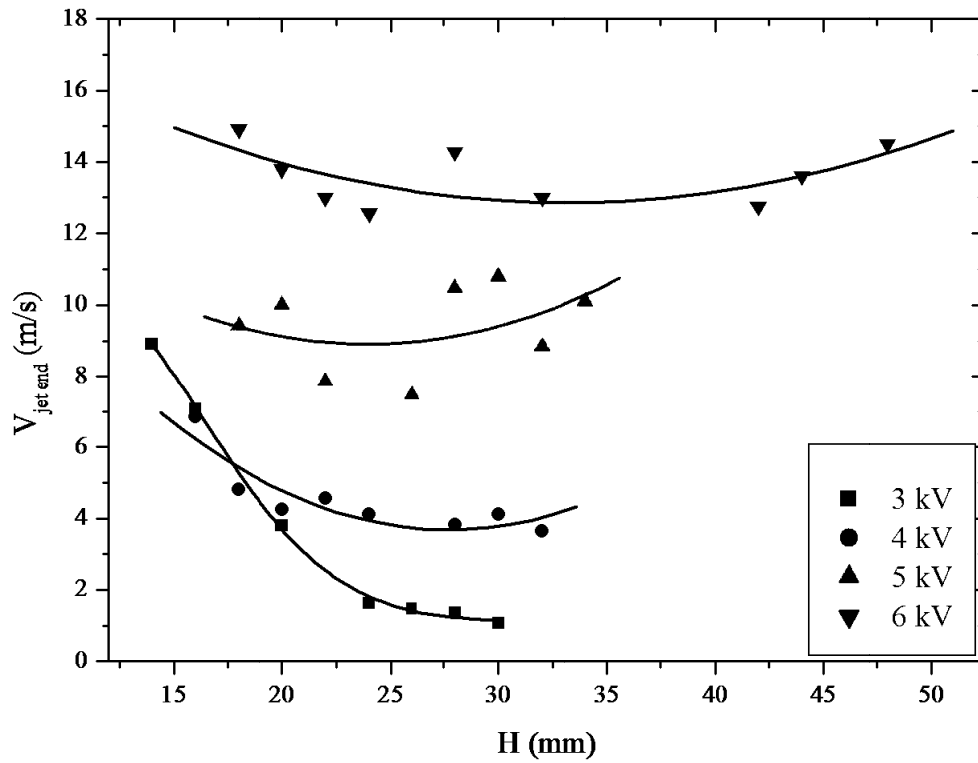


Figure 6.13 The end velocity of the electrified jets as a function of the inter-electrode distance for different values of the applied electrical voltages. A horizontal static aluminum sheet was used as a grounded collector (electrode).

### 6.3.2 Theoretical model

The electrical charge delivered by an electrified jet to the grounded electrode can escape from the landing site on a time scale of the order of  $\tau = \frac{\varepsilon}{4\pi\sigma}$ , where  $\varepsilon$  and  $\sigma$  are the effective electrical permittivity and conductivity, respectively of the collected fibers on the ground. After charge relaxation takes place, the charge can be considered to be transferred to the grounded collector electrode. The previously collected charged fibers are assumed to form disc of radius  $a$ . All the charge on the collected fibers will ultimately make its way to the electrode. However, disappearance of the charge is not immediate and some charge could remain for long times if the collected fibers, which have low electrical conductivity. The linear charge density over the disc perimeter is denoted  $q$ . In the following consideration the charge on the far away segments of the oncoming jet will be neglected compared to the charge at the most recently landed segment, where the electric charge is denoted as  $e$ . A schematic drawing of the pendulum-like motion of the electrified jet is shown in Figure 6.14.

Using the Cartesian coordinates  $xyz$  centered at the disc center as well as the polar angle  $\theta$  corresponding to points on the disc edge, the Columbic repulsive force  $\vec{F}$  acting at the jet segment in contact with the disc is given as:

$$\vec{F} = qea \int_0^{2\pi} \frac{\vec{i}(x-acos\theta)+\vec{j}(y-asin\theta)}{[(x-acos\theta)^2+(y-asin\theta)^2]^{3/2}} d\theta \quad (6.1)$$

where it is assumed that the disc is located at  $z = 0$  with  $z$  being the coordinate axis normal to the disc plane;  $\vec{i}$  and  $\vec{j}$  are the unit vectors of  $x$  and  $y$  axes in the disc plane, respectively.

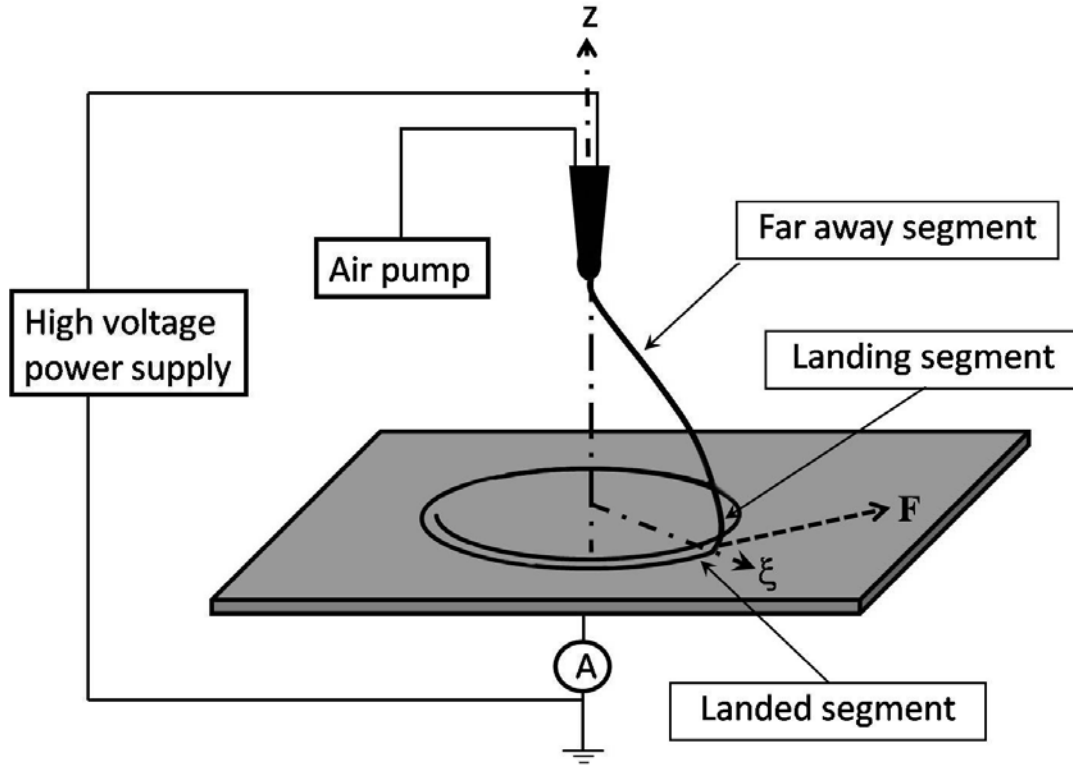


Figure 6.14 Schematic drawing of the pendulum-like motion of the electrified jet.

The integral in Eq. (6.1) can be expressed through the complete elliptic integrals.

Then the components of the repulsive electric force acting on a landed jet segment from the equilibrium electric charge present at the disc edge are given by the following dimensionless expressions:

$$F_x = x \frac{4E(m)}{D^{3/2}(1-m)} - \frac{x}{(x^2+y^2)^{1/2}} P$$

$$F_y = y \frac{4E(m)}{D^{3/2}(1-m)} - \frac{y}{(x^2+y^2)^{1/2}} P \quad (6.2)$$

where the force components are rendered dimensionless by  $qe/a$ , the coordinates  $x$  and  $y$  by  $a$ , and

$$\begin{aligned}
 D_1 &= x^2 + y^2 + 1 \\
 D &= [(x^2 + y^2)^{\frac{1}{2}} + 1]^2 \\
 m &= \frac{(x^2 + y^2)^{\frac{1}{2}}}{D} \\
 P &= \frac{2D_1 E(m)}{D^{3/2}(x^2 + y^2)^{\frac{1}{2}}(1-m)} - \frac{2K(m)}{D^{1/2}(x^2 + y^2)^{\frac{1}{2}}} \quad (6.3)
 \end{aligned}$$

In Eq. (6.2) and Eq. (6.3)  $E(m)$  and  $K(m)$  denote the complete elliptic integrals<sup>162</sup>.

The electrical repulsive force pushes the landing segment in the disc plane. Its motion would be transferred to the whole jet via the elastic stresses sustained by polymer solutions. As a result, the whole jet would move under the action of the electric force driving its landing segment. (Note: The landing segment must be large compared to the buckling phenomena observed, since the successful theory does not include any buckling phenomena.) The equations of motion of the landing segment under the action of the electrical repulsive force from the disc edge have the following dimensionless form:

$$V_x = \frac{dx}{dt}, V_y = \frac{dy}{dt}, F_x = \frac{dV_x}{dt}, F_y = \frac{dV_y}{dt} \quad (6.4)$$

with the components of force determined in Eq. (6.2) and Eq. (6.3). In Eq. (6.4) time is rendered dimensionless by  $T = (\frac{ma^2}{qe})^{1/2}$ , where  $m$  is the mass of the whole jet; the velocity components  $V_x$  and  $V_y$  are rendered dimensionless by  $a/T$ .

Eq. (6.4) is solved numerically. The solution determines the coordinates of the landed jet segment on the disc,  $x$  and  $y$ , or alternatively, its polar coordinates

$$r_0 = (x^2 + y^2)^{1/2} \text{ and } \theta.$$

A plausible assumption is that the mass of the whole jet  $m$  is sufficiently small, and the rate of propagation of the elastic waves in it is sufficiently large. Then, the whole jet can re-orient itself almost instantaneously to the direction of the applied force given by the angle  $\theta = \alpha = \cos^{-1}[\frac{F_x}{(F_x^2 + F_y^2)^{1/2}}]$ . In the plane  $\theta = \alpha$  the jet configuration is given by the Euler-Bernoulli beam theory<sup>163</sup>, with the jet assumed to be clamped at the nozzle and bent under the action of force  $\vec{F}$  applied to its landing segment. Then, the jet configuration in space  $x = X, y = Y, z = Z$  is given by the following dimensionless expressions:

$$\begin{aligned} Z &= H - \frac{2^{\frac{1}{2}}}{(Qf)^{\frac{1}{2}}} [\sqrt{\cos\gamma_0} - \sqrt{\cos\gamma_0 - \cos\gamma}] \\ \xi &= \frac{1}{(2Qf)^{\frac{1}{2}}} \int_{\gamma}^{\pi/2} \frac{\cos\gamma}{\sqrt{\cos\gamma_0 - \cos\gamma}} d\gamma \\ X &= \xi \cos\alpha, Y = \xi \sin\alpha \end{aligned} \tag{6.5}$$

Here  $\gamma$  can be considered as a dummy variable,

$H$  is the distance between the disc and the nozzle rendered dimensionless by  $a$ , which is calculated as:

$$H = \left[ \frac{2\cos\gamma_0}{fQ} \right]^{1/2} \quad (6.6)$$

$$f = (F_x^2 + F_y^2)^{1/2}, \quad Q = \frac{qea}{EI} \quad (6.7)$$

$E$  is the average Young's modulus of polymer solution over the jet.

$I$  is the average moment of inertia of the jet cross-section.

( $I = \frac{\pi b^4}{4}$ , with  $b$  is the average cross-sectional radius over the jet)

$Q$  is the dimensionless parameter characterizing the ratio of the electrical and elastic forces involved.

The value of  $\gamma_0$  in Eq. (6.5) and Eq. (6.6) is determined by the following equation:

$$\xi_0 = \frac{1}{(2Qf)^{1/2}} \int_{\gamma_0}^{\pi/2} \frac{\cos\gamma}{\sqrt{\cos\gamma_0 - \cos\gamma}} d\gamma \quad (6.8)$$

where  $\xi_0$  is the current  $\xi$  coordinate of the landed jet segment on the disc rendered dimensionless by the disc radius  $a$ .

Its approximate solution with a sufficient accuracy is given by:

$$\gamma_0 = \frac{\pi}{2} - \left[ \frac{3}{4} \xi_0 \sqrt{2Qf} \right]^{2/3} \quad (6.9)$$

The dimensional jet length  $L$  is calculated as:

$$\xi_0 = \frac{a}{(2Qf)^{\frac{1}{2}}} \int_{\gamma_0}^{\pi/2} \frac{d\gamma}{\sqrt{\cos\gamma_0 - \cos\gamma}} \quad (6.10)$$

The jet mass is  $m = \rho\pi b^2 L$ ,  $\rho$  is the polymer solution density.

The dimensionless parameter  $Q$  was taken as  $Q = 1$ . In the first case considered, the initial conditions for Eq. (6.4) were chosen as  $t = 0: x = 0.3, y = 0.3, V_x = -0.5, V_y = 0.5$ . The predicted overall jet configuration at different time moments is shown in Figure 6.15a. In this case the jet length  $L \approx a$  and  $H \approx 0.9$  (the corresponding dimensional value is  $0.9a$ ). The landing point of the jet moves over an almost circular path in the disc plane (Figure 6.15b). The corresponding  $x$  and  $y$  coordinates are shown in Figure 6.15c as functions of time. The corresponding period is approximately equal to 3.2. The latter means that the predicted dimensional frequency of such pendulum-like motion is equal to  $\varpi = \frac{2\pi}{3.2} \left[ \frac{qe}{ma^2} \right]^{1/2}$ . This value could be compared to the experimental data.

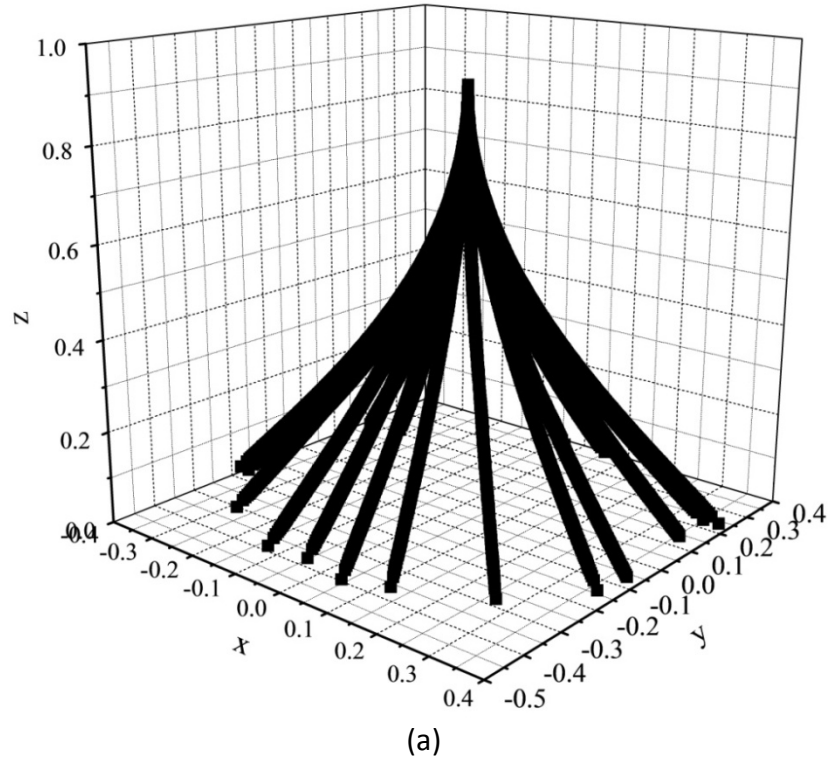


Figure 6.15 Theoretically predicted pendulum-like motion of an electrified jet for the initial conditions  $t = 0: x = 0.3, y = 0.3, V_x = -0.5, V_y = 0.5$ .

(a) Three-dimensional configurations of the jet at several times moments (here and hereinafter the  $xyz$  coordinates are rendered dimensionless by  $a$ ).

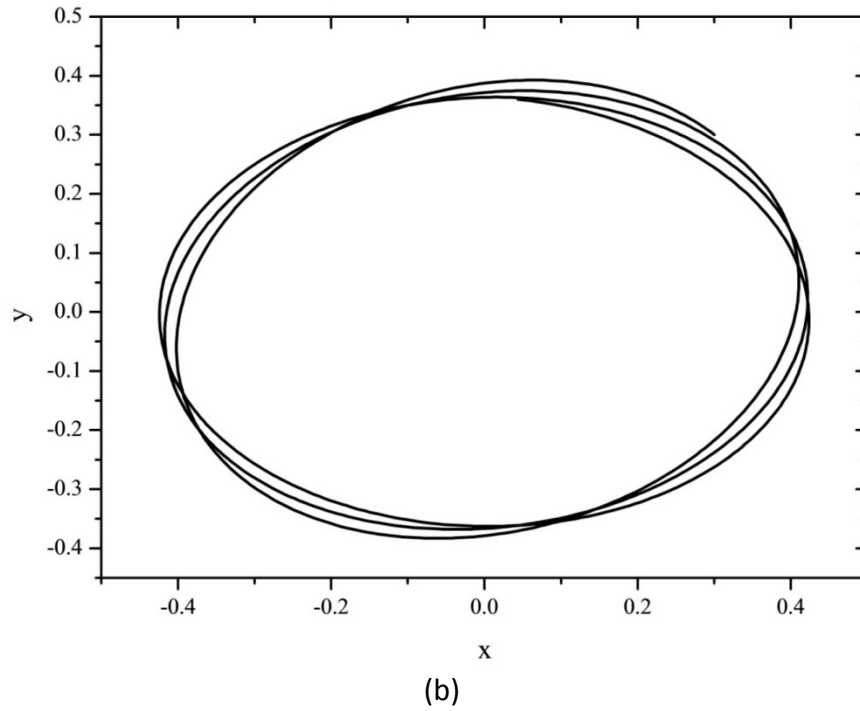
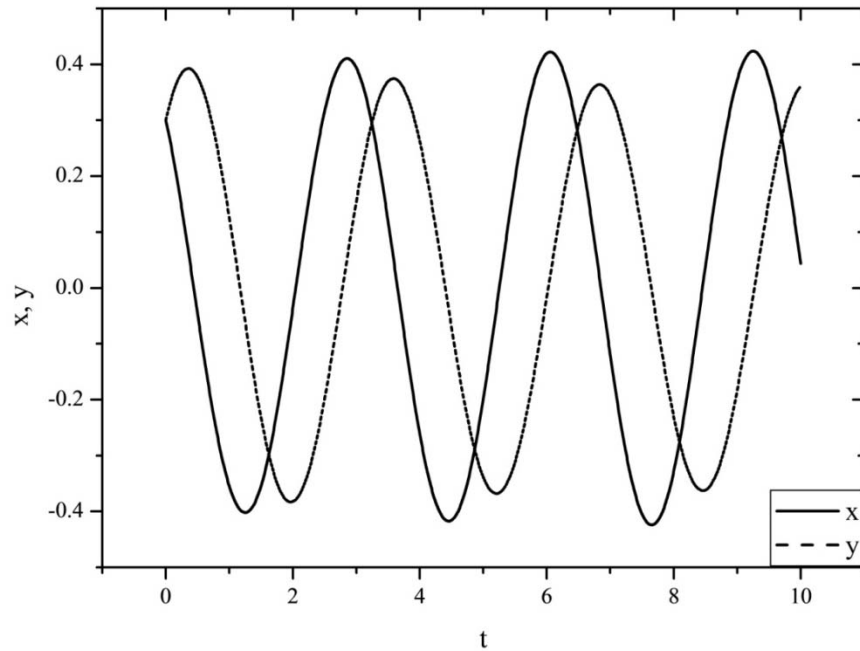


Figure 6.15 Theoretically predicted pendulum-like motion of an electrified jet for the initial conditions  $t = 0: x = 0.3, y = 0.3, V_x = -0.5, V_y = 0.5$ . (continued)

(b) The trajectory of the jet end on the horizontal motionless grounded electrode.



(c)

Figure 6.15 Theoretically predicted pendulum-like motion of an electrified jet for the initial conditions  $t = 0: x = 0.3, y = 0.3, V_x = -0.5, V_y = 0.5$ . (continued)

(c) The horizontal coordinates of the jet end on the grounded electrode as functions of time; time is rendered dimensionless by  $T$ .

Another almost closed loop-like jet path over the disc is shown in Figure 6.16. It corresponds to the following initial conditions:

$$t = 0: x = 0.3, y = 0.1, V_x = -0.5, V_y = 0.5$$

Jet behavior corresponding to Figure 6.15 and Figure 6.16 could be characterized as a circular pendulum.

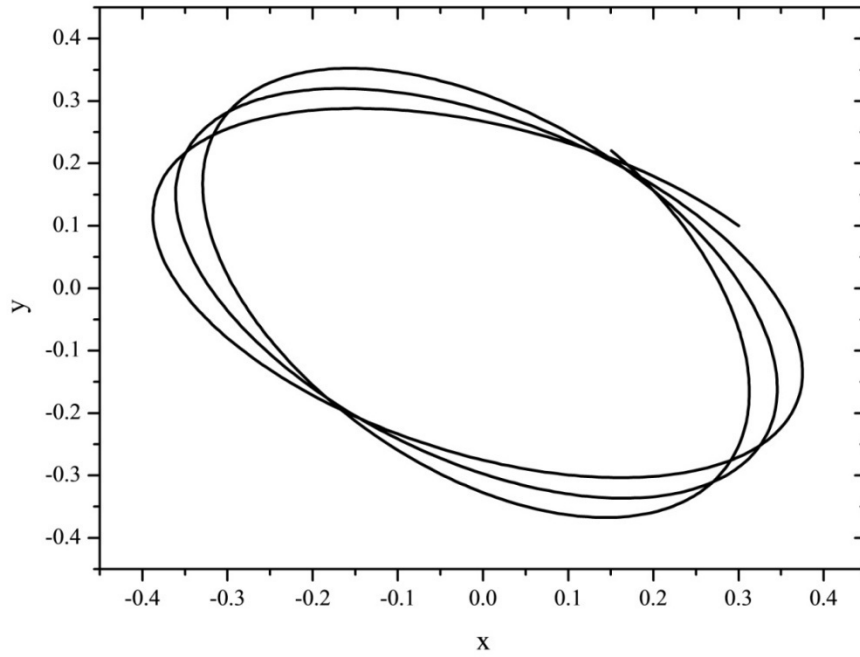


Figure 6.16 Theoretically predicted pendulum-like motion of an electrified jet for the initial conditions:  $t = 0: x = 0.3, y = 0.1, V_x = -0.5, V_y = 0.5$ . The trajectory of the landing point of the jet on the horizontal motionless grounded electrode is shown.

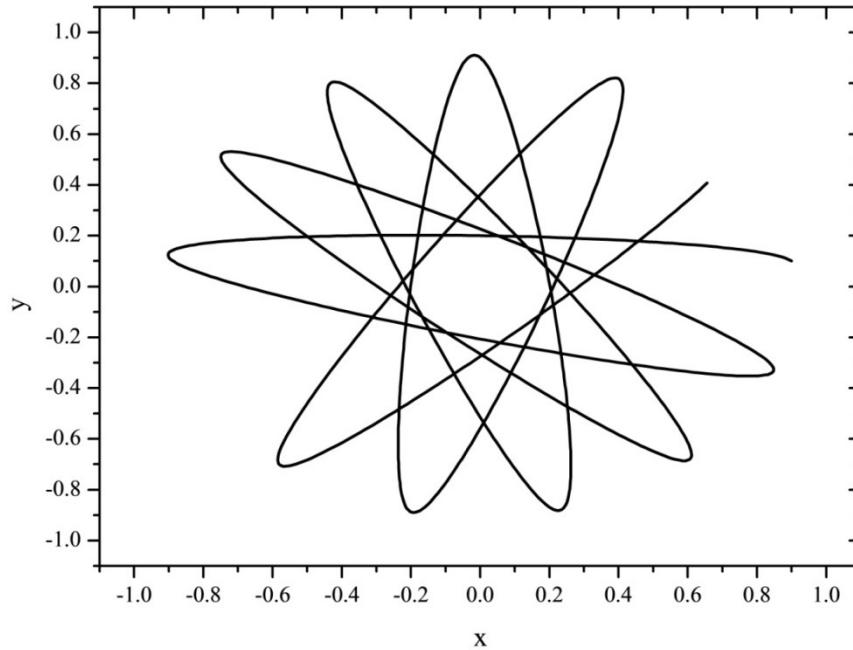


Figure 6.17 Theoretically predicted pendulum-like motion of an electrified jet for the initial conditions:  $t = 0: x = 0.9, y = 0.1, V_x = -0.5, V_y = 0.5$ . The star-like trajectory of the jet end on the horizontal motionless grounded electrode is shown.

A totally different behavior corresponds to the initial conditions,  $t = 0: x = 0.9, y = 0.1, V_x = -0.5, V_y = 0.5$ , which is depicted in Figure 6.17. In this case, in distinction from the previous ones, the jet will produce a star-like deposit on the disc, which is similar to the experimental observation by Sun et al.<sup>123</sup>

In the following, the theoretical predictions will be compared with the experimental data. In particular, the predicted and measured pendulum frequencies will be compared. As discussed before, the dimensionless group  $Q$  (the ratio of the electric to the elastic forces) determines the jet shape in the pendulum-like motion. For the

value of  $Q = 1$ , we found  $L \approx a$  and the dimensional  $H \approx a$ . For the estimates, it is reasonable to take  $a \sim 1$  cm which agrees with the size of the grounded electrode in the experiments. Then, with  $Q = 1$  the jet length  $L$  and the inter-electrode distance  $H$  are both of the order of 1 cm. This is true for the jet image in Figure 6.3. Therefore, the value of  $Q = 1$  is reasonably accurate. Then, from Eq. (6.7) the product  $qe = \frac{EI}{a}$ . Taking elongation viscosity  $\mu \sim 10^4$  g/(cm·s), and the viscoelastic relaxation time  $\theta \sim 10^{-2}$  s, we can estimate the Young modulus  $E$  as  $E \sim \frac{\mu}{\theta} \sim 10^6$  g/(cm·s<sup>2</sup>). Figure 6.3 allows us to estimate the cross-sectional radius  $b$  of the jet as  $b \sim 10^{-2}$  cm, and thus  $I = \frac{\pi b^4}{4} \sim 10^{-8}$  cm<sup>4</sup>. With the values of the parameters listed,  $qe = \frac{EI}{a} \sim 10^{-2}$  g·cm<sup>2</sup>/s<sup>2</sup>. The total mass of the jet can be estimated as  $m = \rho \pi b^2 L$ , where  $\rho$  is the polymer density. Taking for the estimate  $\rho \sim 1$  g/cm<sup>3</sup>, and using the above-mentioned values of  $b$  and  $L$ , we find  $m \sim 10^{-4}$  g. Then, the predicted frequency of the pendulum-like motion  $\varpi = \frac{2\pi}{3.2} \left[ \frac{qe}{ma^2} \right]^{1/2} \approx 20$  Hz. This value is of the order of the lower bound of the experimental data for the measured frequency  $\varpi$  in Figure 6.11.

It is of interest to estimate the values of  $q$  and  $e$  separately in addition to their product  $qe \sim 10^{-2}$  g·cm<sup>2</sup>/s<sup>2</sup> estimated above. For an estimate of the electrical (convective) current  $I_{el}$  we take from Figure 6.9 the value  $I_{el} \sim 10 \mu\text{A} \sim 10^4$  g<sup>1/2</sup>cm<sup>3/2</sup>/s<sup>2</sup>. Let us assume that charge  $e$  corresponds to a jet section of the length  $l \sim 10^{-1}$  cm above the grounded electrode, i.e. to the volume  $\pi b^2 l \sim 10^{-5}$  cm<sup>3</sup>. Denote the volumetric charge density in the jet as  $C$ , and the jet velocity as  $V$ . Then,  $C = \frac{I_{el}}{V \pi b^2 l} = \frac{I_{el}}{V \pi b^2}$ .

Therefore,  $e = c\pi b^2 l = \frac{l e l}{V}$ . Take for the estimate  $V=10^3$  cm/s as in Figure 6.13. Then,  $e \sim 1 \text{ g}^{1/2} \text{ cm}^{3/2} / \text{s}$ . For comparison, the value of  $e$  in the computations of electrospinning used in Reneker<sup>5</sup> was  $e = 8.48 \text{ g}^{1/2} \text{ cm}^{3/2} / \text{s}$ . Then,  $q \sim 10^{-2} / e \sim 10^{-2} \text{ g}^{1/2} \text{ cm}^{1/2} / \text{s}$ . On the other hand, with no charge dissipation we would have  $q_0 \sim \frac{e}{2\pi a} \sim 10^{-1} \text{ g}^{1/2} \text{ cm}^{1/2} / \text{s}$ .

Conduction of charge to the collector should be responsible for the reduction of  $q_0$  by an order of magnitude compared to the value of  $q$ .

#### 6.4 SUMMARY

Pendulum-like rotation of a short, almost straight, electrified jet was discovered. Its characteristics, in particular frequency of jet rotation about the vertical axis, were measured. The theoretical model proposed attributed pendulum-like jet motion to the repulsion of the electric charges brought to the grounded electrode by the jet, but not immediately "relaxed", which is transferred to the electrode. Comparison of the predicted and measured jet frequency was in reasonable agreement. Fishnet-like hierarchical structures were produced. Morphologies of these structures were manipulated by control of the pendulum-like rotation and buckling instability of the electrified jet.

## CHAPTER VII

### SUMMARY AND CONCLUSIONS

The electrospinning jet is a continuous fluid flow ejected from the surface of a fluid when the applied electrical force overcomes surface tension<sup>1</sup>. The jet moves straight away from the tip for some distance and then becomes unstable and bends into coiled loops. When the distance between the spinneret and grounded collector is reduced to less than the length of the straight segment, the electrical bending instability does not occur; instead, only a straight jet is produced.

Determination of the behavior of the jet path near the onset of the first electrical bending instability is important for orderly collection of the electrospun fibers. Direct observations of the onset and development of the electrical bending instability were presented. Morphologies of electrospun fibers produced at different stages of the jet were discussed. Electrical bending instabilities of an electrospinning jet collected on a solid surface were observed, at various distances from the orifice. Frequency of the electrical bending instability was in the range of  $10^3$  Hz. Increased voltage delayed the onset of the electrical bending instability and produced a longer straight segment in the jets. Under certain conditions, high applied voltage delayed onset of the bending instability and a straight segment was deposited on the collector. Fibers were produced by collecting a straight, electrified jet on a laterally moving collector. A minimum

collector velocity was needed to produce straight fibers. When velocity of the collector was below this minimum, buckled fibers were produced. This resulted in two-dimensional periodical arrays that might be used in microelectronics and biomedical devices.

A novel method of characterization of longitudinal stresses in electrospinning jets was introduced. Measured initial longitudinal stresses in jets of a 6 wt% aqueous solution of polyethylene oxide ( $M_w=400$  kDa) were of the order of 100 kPa. This is two orders of magnitude larger than the value in other charge free, viscoelastic jets. This is attributed to rapid stretching ( $100 \text{ sec}^{-1}$  to  $1000 \text{ sec}^{-1}$ ) of polymeric liquids in the transition zone between the Taylor cone and the beginning of the jet. The velocity of the fluid along the straight segment was determined from jet diameter and data from the laser Doppler velocimetry. Tensile stress was measured by creating lateral displacement near the beginning of the jet, and observing its propagation along the jet. Combination of velocity and stress data was used to determine modulus and relaxation time.

A buckling instability of the electrospinning jet was discovered and discussed. Two-dimensional and three-dimensional buckling were studied in electrically charged jets that impinged onto collectors that were moving laterally at constant velocity. Both straight and electrically-bent jets buckled near the collector. For bending, electrospinning jets, short wave-length buckling was superimposed on long wave-length electrical bending loops. The frequency corresponding to the buckling was in the range of  $10^5$  to  $10^6$  Hz, and the frequency for the bending loops was about  $10^3$  Hz. Most buckling patterns resembled those produced by uncharged, highly viscous, gravity-

driven jets impinging onto a moving, hard, flat surface. Frequencies derived from observations of the buckling patterns were compared to those predicted for uncharged jets impinging on a motionless hard flat surface. A reasonable agreement of the theoretical and experimental results was found. Morphologies of the electrospun fibers were manipulated by control of the buckling instability. Various two-dimensional and three-dimensional micron-sized patterns were.

A new phenomenon, pendulum-like rotation of an electrified jet, was observed and hierarchical structures made from buckled fibers were described. The theoretical model attributed pendulum-like jet motion to the repulsion of the electrical charges brought to the grounded electrode by the jet, but not immediately conducted to metal collector. Comparison of the predicted and measured jet frequency was in a reasonable agreement.

## REFERENCES

1. Doshi J.; Reneker D. H., *J. Electrostatics*, **35**, 151-160, (1995)
2. Yarin A. L.; Koombhongse S.; Reneker D. H., *J. Appl. Phys.*, **90**, 4836-4846, (2001)
3. Reneker D.H.; Han T., *Mater. Res. Soc. Symp. Proc.*, **948**, 0948-B07-01, (2007)
4. Han T.; Reneker D.H.; Yarin A.L., *Polymer*, **48**, 6064-6076, (2007)
5. Reneker D. H.; Yarin A. L.; Fong H.; Koombhongse S., *J. Appl. Phys.*, **87**, 4531-4547, (2000)
6. Yarin A. L.; Koombhongse S.; Reneker D. H., *J. Appl. Phys.*, **89**, 3018-3026, (2001)
7. [www.donaldson.com](http://www.donaldson.com)
8. Schreuder-Gibson H. L.; Gibson P.; Senecal K.; Sennett K.; Walker K.; Yeomans W.; Ziegler D.; Tsai P. P., *J. Adv. Mater.*, **34**, 44-55, ( 2002)
9. Ramaseshan R.; Sundarrajan S.; Liu Y.; Barhate R. S.; Lala N. L.; Ramakrishna S., *Nanotechnology* , **17**, 2947-2953, (2006)
10. Gibson P.; Schreuder-Gibson H.; Rivin D., *Colloids Surf. A*, **187–188**, 469-481, (2001)
11. Annis D.; Bornat A.; Edwards R.O.; Higham A.; Loveday B.; Wilson J., *Transaction of the American Society for Artificial Internal Organs*, **24**, 209, (1978)
12. Lannutti J.; Reneker D.H.; Ma T.; Tomasko D.; Farson D., *Mater. Sci. and Eng. C*, **27**, 504-509, (2007)
13. Kameoka J.; Orth R.; Ilic B.; Czaplewski D.; Wachs T.; Craighead H. G., *Anal. Chem.* **74**, 5897-5901, (2002)
14. Kameoka J.; Craighead H. G., *Appl. Phys. Lett.* **83**, 371–373, (2003)

15. Kameoka J.; Orth R.; Yang Y.; Czaplewski D.; Mathers R.; Coates G. W.; Craighead H. G. *Nanotechnology*, **14**, 1124-1129, (2003)
16. Kameoka J.; Verbridge S. S.; Liu H. Q.; Czaplewski D. A.; Craighead H. G., *Nano Lett.*, **4**, 2105-2108, (2004)
17. Liu H. Q.; Kameoka J.; Czaplewski D. A.; Craighead H. G., *Nano Lett.*, **4**, 671-675, (2004)
18. Hou H.; Jun Z.; Reuning A.; Schaper A.; Wendorff J. H.; Greiner A., *Macromolecules*, **35**, 2429-2431, (2002)
19. Bognitzki M.; Hou H.; Ishaque M.; Frese T.; Hellwig M.; Schwarte C.; Schaper A.; Wendorff J.H.; Greiner A., *Adv. Mater.*, **12**, 637-640, (2000)
20. Caruso R.; Schattka J.H.; Greiner A., *Adv. Mater.*, **13**, 1577-1579, (2001)
21. Sun Z.; Zeng J.; Hou H.; Wickel H.; Wendorff J.H.; Greiner A., *Prog. Colloid Polym. Sci.*, **130**, 15-19, (2005)
22. Moller K.; Quinn J.F.; Johnston A.P.R.; Becker M.; Greiner A.; Caruso F., *Chem. Mater.*, **18**, 2397-2403, ( 2006)
23. Sun Z.; Zussman E.; Yarin A.L.; Wendorff J.H.; Greiner A., *Adv. Mater.*, **15**, 1929-1932, ( 2003)
24. Loscertales G.; Barrero A.; Guerrero I.; Cortijo R.; Marquez M.; GaQRn-Calvo A.M., *Science*, **295**, 1695-1698, (2002)
25. Larsen G.; Velarde-Ortiz R.; Minchow K.; Barrero A.; Loscertales I.G., *J. Am. Chem. Soc.*, **125**, 1154-1155, (2003)
26. Li D.; Xia Y., *Nano Lett.*, **4**, 933-938, (2004)
27. Yu J.H.; Fridrikh S. V.; Rutledge G. C., *Adv. Mater.*, **16**, 1562- 1566, (2004)
28. Zhang Y.; Huang Z. M; Xu X.; Lim C. T.; Ramakrishna S., *Chem. Mater.*, **16**, 3406-3409, (2004)
29. Li D.; McCann J. T.; Xia Y., *Small*, **1**, 83-86, (2005)

30. Jiang H.; Hu Y.; Li Y.; Zhao P.; Zhu K.; Chen W., *J. Controlled Release*, **108**, 237-243, (2005)
31. Reznik S. N.; Yarin A. L.; Zussman E.; Bercovici L., *Phys. Fluids*, **18**, 062101-062113, (2006)
32. Wang M.; Yu J. H., Kaplan D. L., Rutledge G. C., *Macromolecules*, **39**, 1102-1107, (2006)
33. Han X.; Huang Z.; He C.; Liu L.; Han X.; Wu Q., *Polym. Compos.*, **27**, 381-387, (2006)
34. Zhang Y.; Wang X.; Feng Y.; Li J.; Lim C. T.; Ramakrishna S., *Biomacromolecules*, **7**, 1049-1057, (2006)
35. Dror Y.; Salalha W.; Avrahami R.; Zussman E.; Yarin A. L.; Dersch R.; Greiner A.; J. H. Wendorff J. H., *Small*, **3**, 1064-1073, (2007)
36. Gilbert W. *de Magnet*, Book 2, Chap. 2, (1600) (Trans. By P. F. Mottelay.)
37. Bose G. M., *Recheres sur la cause et sur la veritable theorie del'electricite: Wittenberg*, (1745)
38. Lord R., *Proc. Roy. Soc.*, **28**, 406–409, ( 1879)
39. Lord R., *Proc. Roy. Soc.*, **29**, 71–79, ( 1879)
40. Lord R., *Phil. Mag.*, **14**, 184–186, (1882)
41. Cooley J. F., US, 692,631, (1902)
42. Morton W. J., US, 705,691, (1902)
43. Cooley J. F., US, 745,276, (1903)
44. Zeleny J., *J. Phys. Rev.*, **3**, 69-91, (1914)
45. Zeleny J., *J. Proc. Camb. Phil. Soc.*, **18**, 71-83, (1915)
46. Zeleny J., *J. Phys. Rev.*, **10**, 1-6, (1917)
47. Zeleny J., *J. Franklin. Inst.*, **219**, 659-676, (1935)

48. Hagiwaba K.; Oji-Machi O.; Ku K., Jpn, 1,699,615, (1929)
49. Formhals A., US, 1,975,504, (1934)
50. Formhals A., US, 2,123,992, (1934)
51. Vonnegut B.; Neubauer R. L., *J. Colloid Sci.*, **7**, 616, (1952)
52. Taylor G. I., *Proc. Roy. Soc. Lond.*, **280**, 383-397, (1964A)
53. Michelson D., *Electrostatic Atomization: Bristol*, UK, (1990)
54. Taylor G. I., *Proc. Roy. Soc. Lond.*, **291**, 145-158, (1964A)
55. Taylor G. I., *Proc. Roy. Soc. Lond.*, **313**, 453-475, (1969A)
56. Lord R., *Philos. Mag.*, **34**, 145-155, (1892)
57. Simons H. L., US, 3,280,229, (1966)
58. Baumgarten P. K., *J. Colloid Interface Sci.*, **36**, 71-79, (1971)
59. Martin G. H.; Derek I., US, 4,043,331, (1977)
60. Martin G. H.; Derek I., US, 4,044,404, (1977)
61. Simm W. L.; Claus, G. O.; Bonart R. B.; Bela V. F. G., US, 4,069,026, (1978)
62. Horning D. W.; Hendricks C. D., *J. Appl. Phys.*, **50**, 2614-2617, (1979)
63. Fine J.; Passaic N. J.; Sigismondo A. T., US, 4,223,101, (1980)
64. Guignard C., US, 4,230,650, (1980)
65. Guignard C., US, 4,287,139, (1981)
66. Larrondo L.; Manley R. S. J., *J. Polym. Sci.: Polym. Phys.*, **19**, 909-919, (1981)
67. Larrondo L.; Manley R. S. J., *J. Polym. Sci.: Polym. Phys.*, **19**, 921-932, (1981)
68. Larrondo L.; Manley R. S. J., *J. Polym. Sci.: Polym. Phys.*, **19**, 933-940, (1981)

69. Bornat A., US, 4,323,525, (1982)
70. Bornat A., US, 4,689,186, (1987)
71. Srinivasan G.; Reneker D. H., *Polym. Int.*, **36**, 195-201, (1995)
72. Reneker D. H.; Chun I., *Nanotechnology*, **7**, 216-223, (1996)
73. Fang X.; Reneker D.H., *J. Macromolecular Sci. Phys.*, **36**, 169–173, (1997)
74. Saville D. A., *Annu. Rev. Fluid Mech.*, **29**, 27-64, (1997)
75. Spivak A. F.; Dzenis Y. A., *Appl. Phys. Lett.*, **73**, 3067-3069, (1998)
76. Fong H.; Chun I.; Reneker D. H., *Polymer*, **40**, 4585–4592, (1999)
77. Scardino F. L.; Balonis R. J., US, 6,106,913, (2000)
78. Zarkoob S.; Reneker D. H.; Ertley D.; Eby R. K.; Hudson S. D., US, 6,110, 590, (2000)
79. Spivak A. F.; Dzenis Y. A.; Reneker D. H., *Mech. Res. Comm.*, **27**, 37-42, (2000)
80. Koombhongse S.; Liu W.; Reneker D. H., *J. Polym. Sci. B: Polym. Phys.*, **39**, 2598-2606, (2001)
81. Yarin A. L.; Kataphinan W.; Reneker D. H., *J. Appl. Phys.*, **98**, 064501–12, (2005)
82. Hohman M. M.; Shin Y. M.; Rutledge G. C.; Brenner M. P., *Phys. Fluids*, **13**, 2201-2220, (2001)
83. Hohman M. M.; Shin Y. M.; Rutledge G. C.; Brenner M. P., *Phys. Fluids*, **13**, 2221-2236, (2001)
84. Shin Y. M.; Hohman M. M.; Brenner M. P.; Rutledge G. C., *Polymer*, **42**, 9955-9967, (2001)
85. Shin Y. M.; Hohman M. M.; Brenner M. P.; Rutledge G. C., *Appl. Phys. Lett.*, **78**, 1149-1151, (2001)
86. Reneker D. H.; Kataphinan W.; Theron A.; Zussman E.; A.L. Yarin A. L., *Polymer*, **43**, 6785-6794, (2002)

87. Feng J. J., *Phys. Fluids*, **14**, 3912-3926, (2002)
88. Feng J. J., *J. Non-Newtonian Fluid Mech.*, **116**, 55-70, (2003)
89. Lee K.H.; Kim H.Y.; Bang H.J.; Jung Y.H.; Lee S.G., *Polymer*, **44**, 4029-4034, (2003)
90. McKee M. G.; Wilkes G. L.; Colby R. H.; Long T. E., *Macromolecules*, **37**, 1760-1767, (2004)
91. Shenoy S. L.; Bates W. D.; Frisch H. L.; Wnek G., *Polymer*, **46**, 3372-3384, (2005)
92. Gupta P.; Elkins C.; Long T. E.; Wilkes G. L., *Polymer*, **46**, 4799-4810, (2005)
93. Shenoy S. L.; Bates W. D.; Wnek G., *Polymer*, **46**, 8990-9004, (2005)
94. Yu J. H.; Fridrikh S. V.; Rutledge G. C., *Polymer*, **47**, 4789-4797, (2006)
95. Carroll C.P.; Joo Y. L., *Phys. Fluids*, **18**, 053102-053114, (2006)
96. Higuera F. J., *J. Fluid Mech.*, **558**, 143-152, (2006)
97. Koombhongse S.; Zhong Z.; Reneker D. H., *Polymer*, **48**, 5742-5746, (2007)
98. Sanders E. H.; Kloefkorn R.; Bowlin G. L.; Simpson D. G.; Wnek G. E., *Macromolecules*, **36**, 3803-3805, (2003)
99. Loscertales I. G.; Barrero A.; Márquez M.; Spretz R.; Velarde-Ortiz R.; Larsen G., *J. Am. Chem. Soc.*, **126**, 5376-5377, (2004)
100. Díaz J. E.; Barrero A.; Márquez M.; Loscertales I. G., *Adv. Funct. Mater.*, **16**, 2110-2116, (2006)
101. Srivastava Y.; Loscertales I. G.; Marquez M.; Thorsen T., *Microfluid Nanofluid*, Springer-Verlag, (2007)
102. Xu X.; Yang L.; Xu X.; Wang X.; Chen X.; Liang Q.; Zeng J.; Jing X., *J. Controlled Release*, **108**, 33-42, (2005)
103. Hou H.; Reneker D. H., *Adv. Mater.*, **16**, 69-73, (2004)

104. Tomer V.; Teye-Mensah R.; Tokash J.C.; Stojilovic N.; Kataphinan W.; Evans E.A.; Chase G.G.; Ramsier R.D.; Smith D. J.; Reneker D.H., *Sol. Energy Mater. Sol. Cells*, **85**, 477–488, (2005)
105. Zhang G.; Kataphinan W.; Teye-Mensah R.; Katta P.; Khatri L., Evans E.A.; Chase G.G.; Ramsier R.D.; Reneker D.H., *Mater. Sci. Eng. B*, **116**, 353–358, (2005)
106. Doiphode S. V.; Reneker D. H.; Chase G.C., *Polymer*, **47**, 4328-4332, (2006)
107. Kessick R.; Fenn J.; Tepper G., *Polymer*, **45**, 2981-2984, (2004)
108. Sarkar S.; Levit N.; Tepper G., *Sens. Actuat. B*, **114**, 756-761, (2006)
109. Sarkar S.; Deevi S.; Tepper G., *Macromol. Rapid Commun.*, **28**, 1034-1039, (2007)
110. Dersch R.; Liu T.; Schaper A.; Greiner A.; Wendorff J. H., *J. Polym. Sci. Part A.*, **41**, 545-553, (2001)
111. Theron A.; Zussman E.; Yarin A. L., *Nanotechnology*, **12**, 384-390, (2001)
112. Theron A.; Zussman E.; Yarin A. L., *Appl. Phys. Lett.*, **82**, 973-975, (2003)
113. Sundaray B.; Subramanian V.; Natarajan T. S., *Appl. Phys. Lett.*, **84**, 1222-1224, (2004)
114. Li D.; Wang Y.; Xia Y., *Nano Lett.*, **3**, 1167-1171, (2003)
115. Li D.; Wang Y.; Xia Y., *Adv. Mater.*, **16**, 361-366, (2004)
116. Li D.; M. Ouyang M.; McCann J.; Xia Y., *Nano Lett.*, **5**, 913-916, (2005)
117. Katta P.; Alessandro M.; Ramsier R. D.; Chase G. G., *Nano Lett.*, **4**, 2215-2218, (2004)
118. Smit E.; Buttner U.; Sanderson R. D., *Polymer*, **46**, 2419-2423, (2005)
119. Kameoka J.; Orth R.; Yang Y.; Czaplewski D.; Mathers R.; Coates G. W.; Craighead H. G., *Nanotechnology*, **14**, 1124-1129, (2003)
120. Liu H. Q.; Reccius C. H.; Craighead H. G., *Appl. Phys. Lett.*, **87**, 253106-3, (2005)

121. Bellan L. M.; Cross J. D.; Strychalski E. A.; Moran-Mirabal J.; Craighead H. G., *Nano Lett.*, **6**, 2526–2530, (2006)
122. Moran-Mirabal J. M.; Slinker J. D.; DeFranco J. A.; Verbridge S. S.; Ilic R.; Flores-Torres S.; Abrun H.; Malliaras G. G.; Craighead H. G., *Nano Lett.*, **7**, 458–463, (2007)
123. Sun D.; Chang C.; Li S.; Lin L., *Nano Lett.*, **6**, 839-842, (2006)
124. Xue H., *Formation and characterization of polymer jets in electrospinning*, Doctorial Dissertation, The University of Akron, August, (2003)
125. Doshi J. N., *The electrospinning process and application of electrospun fibers*, Doctorial Dissertation, The University of Akron, August, (1994)
126. Koombhongse S., *The formation of nanofibers from electrospinning process*, Doctorial Dissertation, The University of Akron, May, (2001)
127. Ziabicki A. *Fundamentals of Fiber Formation*, Wiley, London, (1976)
128. Eds. Ciferri A.; Ward I. M., *Ultra-High Modulus Polymers*, *Appl. Sci. Publ.*, London, (1979)
129. Eds. Ziabicki A.; Kawai H., *High-Speed Fiber Spinning*, Wiley, New York, (1985)
130. Yarin A. L., *Free Liquid Jets and Films: Hydrodynamics and Rheology*. Longman Scientific & Technical, Wiley & Sons, Harlow, New York, (1993)
131. Reneker D. H.; Yarin A. L.; Zussman E.; Xu H., *Adv. Appl. Mech.*, **41**, 43-195, (2007)
132. Gill S. J.; Gavis J., *J. Polym. Sci.*, **20**, 287-298, (1956)
133. Gill S. J.; Gavis J., *J. Polym. Sci.*, **21**, 353-362, (1956)
134. Goren S. L.; Gavis J., *Phys. Fluids*, **4**, 575-579, (1961)
135. Bazilevskii A. V.; Entov V. M.; Rozhkov A. N., *Fluid Dynamics*, **20**, 169-175, (1985)
136. Middleman S.; Gavis J., *Phys. Fluids*, **8**, 222-229, (1965)
137. Kowalewski T. A.; Blonski S.; Barral S., *Bull. Pol. Ac.: Tech.*, **53**, 385-394, (2005)

138. Entov V. M.; Yarin A. L., *J. Fluid Mech.* , **140**, 91-111, (1984)
139. Yarin A. L.; *J. Non-Newtonian Fluid Mech.*, **37**, 113–138, (1990)
140. Taylor G. I., *Proc. 12th Intl. Congr. Appl. Mech.*, Stanford, 382-388, (1968)
141. Timoshenko S. P.; Gere J. M., *Theory of Elastic Stability*, McGraw-Hill, New York, (1961)
142. Cruickshank J. O.; Munson B. R., *J. Fluid Mech.* , **113**, 221-239, (1981)
143. Cruickshank J. O., *J. Fluid Mech.*, **193**, 111-127, (1988)
144. Tchavdarov B.; Yarin A. L.; Radev S., *J. Fluid Mech.*, **253**, 593-615, (1993)
145. Yarin A. L.; Tchavdarov B., *J. Fluid Mech.*, **307**, 85-99, (1996)
146. Chiu-Webster S.; Lister J. R., *J. Fluid Mech.*, **569**, 89-111, (2006)
147. Ribe N. M.; Lister J. R.; Chiu-Webster S., *Phys. Fluids*, **18**, 124105-124108, (2006)
148. Kessick R.; Tepper G., *Appl. Phys. Lett.*, **84**, 4807-4809, (2004)
149. Shin M. K.; Kim S. I.; Kim S. J., *Appl. Phys. Lett.*, **88**, 223109-3, (2006)
150. Lord R., *The Theory of Sound.*, Dover Publ., New York, (1945)
151. Chandrasekhar S., *Hydrodynamic and Hydromagnetic Stability.*, Clarendon Press, Oxford, (1961)
152. Garmendia L., *AIChE Journal*, **23**, 935-938, (1977)
153. Garmendia L.; Smith I. K., *Can. J. Chem. Eng.*, **53**, 606-610, (1975)
154. Huebner A. L.; Chu H. N., *J. Fluid Mech.*, **49**, 361-372, ( 1971)
155. Tomita Y.; Sudou K.; Ishibashi Y., *Bull. J.S.M.E.*, **22**, 1390-1398, (1979)
156. Kirichenko V. N.; Petryanov-Sokolov I. V.; Suprun N. N.; Shutov A. A., *Sov. Phys. Dokl.*, **31**, 79-81, (1986)
157. Frenot A.; Chronakis I. S., *Curr. Opin. Colloid Interface Sci.*, **8**, 64-75, (2003)

158. Huang Z. M.; Zhang Y. Z.; Kotaki M.; Ramakrishna S., *Compos. Sci. Tech.*, **63**, 2223-2253, (2003)
159. Dzenis Y., *Science*, **304**, 1917-1919, (2004)
160. Ramakrishna S.; Fujihara K.; Teo W. E.; Lim T. C.; Ma Z., *An Introduction to Electrospinning of Nanofibers*, World Scientific, Singapore, (2005)
161. Saville D. A., *Phys. Fluids*, **14**, 1095-1099, (1971)
162. Abramowitz M.; Stegun I. A., *Handbook of Mathematical Functions*, Dover Publ., New York, (1972)
163. Landau L. D.; Lifshits E. M., *Theory of Elasticity*, Pergamon Press, New York, (1975)